Journal of Energy Challenges and Mechanics

ISSN 2056-9386

http://www.nscj.co.uk/JECM/

Volume 2, Issue 4
December 2015

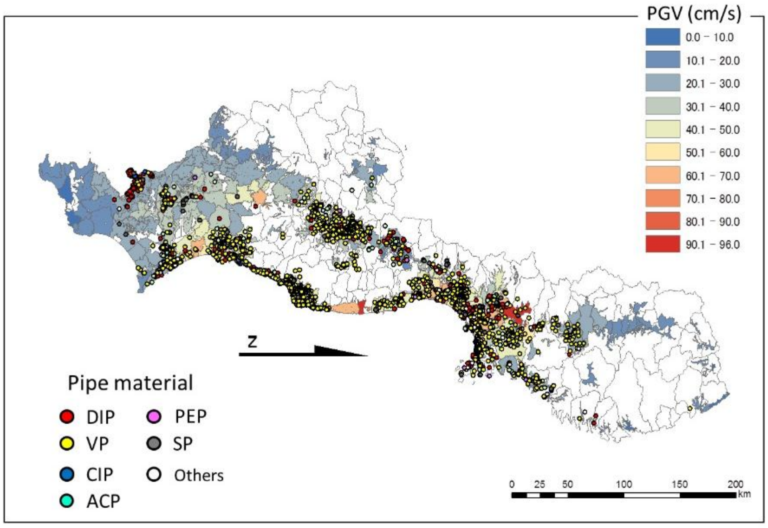

Featured article:

Damage Assessment of Water Distribution Pipelines after the 2011 off the Pacific Coast of Tohoku Earthquake

Yoshihisa Maruyama[1], Shigeru Nagata[2], Kazue Wakamatsu[3]*

[1]Department of Urban Environment Systems, Chiba University, 263-8522, Japan

[2]Kajima Technical Research Institute, Kajima Corporation Co., Ltd., 182-0036, Japan

[3]Department of Civil Engineering, Kanto Gakuin University, 236-8501, Japan

North Sea

North Sea Conference & Journal LTD
2 Charlestown Walk, Cove Bay, AB12 3EZ, Aberdeen, Scotland, United Kingdom
http://www.nscj.co.uk/JECM/ | jecm@nscj.co.uk | +44(0)1224 875635

Journal of Energy Challenges and Mechanics
http://www.nscj.co.uk/JECM/
ISSN 2056-9386
Volume 2 (2015) issue 4

TABLE OF CONTENTS pages

Journal of Energy Challenges and Mechanics
http://www.nscj.co.uk/JECM/
ISSN 2056-9386
Volume 2 (2015) issue 4, article 1

Integrative technology assessment of carbon capture and utilization: a German perspective

碳捕获和利用的综合技术评估：一个德国视角

Wilhelm Kuckshinrichs[1*], Juergen-Friedrich Hake[1*], Peter Markewitz[1]

[1]*Institute for Energy and Climate Research – Systems Analysis and Technology Evaluation (IEK-STE), Forschungszentrum Juelich, 52425 Juelich, Germany*

w.kuckshinrichs@fz-juelich.de

Accepted for publication on 4th November 2015

Abstract - **Fossil-based energy conversion and energy-intensive industries are sources of a large part of global CO_2 emissions. Carbon capture and storage (CCS) technologies are regarded as important technical options to reduce worldwide CO_2 emissions. However, the discussion on the potential of CCS is highly controversial and focuses on issues such as *technology development, economic competitiveness, environmental and safety impacts*, and *social acceptance*. The paper focuses on these aspects and analyses the potential and the possible role of CCS technologies. When regional considerations are important for evaluation, e.g. in the case of social acceptance, the focus is on the German perspective.**

While there is no lack of technical options for CCS and storage capacities are available, the question arises as to whether and under what conditions CCS could become a key element within the framework of implementing climate protection strategies. To answer this question, an Integrated Technology Assessment is required covering technical, economic, environmental, and social considerations. In order to play a decisive role in climate protection strategies, 5 key criteria are identified: (1) 'demonstration of an industrial scale and commercial availability', (2) 'environmental and safety requirements', (3) 'cost efficiency and economic viability', (4) 'coordination of energy and climate policy', and (5) 'public acceptance'. Given the different analyzes of the 5 key criteria essentials are formulated assessing the potential of CCS technologies as elements of climate protection strategies. Finally, the OECD approach for constructing composite indicators for assessing technologies is used.

Keywords – **CCS, CO_2 utilization, technology assessment.**

I. Introduction

In order to limit the anthropogenic increase in the average global temperature by 2100 to 2 °C, the concentration of CO_2 in the atmosphere must be restricted to 450 ppmv according to the Intergovernmental Panel on Climate Change (IPCC). To achieve this target, global CO_2 emissions must be cut by 50 % by 2050 compared to levels in 1990. However, global energy consumption is growing year by year and the use of fossil energy carriers is not only continuing, but coal in particular is becoming even more important as an energy carrier globally.

In their analyses on stabilizing global CO_2 emissions, Pacala and Socolow identified strategies ('wedges') to help reduce future CO_2 emissions [1]. A 'wedge' is a strategy or measure to reduce CO_2 emissions, which are forecast to increase in fifty years to 3.67 billion tonnes of CO_2 ($GtCO_2$) per year (= 1 GtC/a). Over 50 years, this represents a cumulative total of approx. 92 $GtCO_2$ (25 GtC). These wedges include energy efficiency, a fuel shift, nuclear energy, wind energy, solar energy, bioenergy, and natural CO_2 sinks, as well as carbon capture and storage (CCS).

Numerous analyses of and projections for the global energy system also emphasize the importance of CCS in strategies for reducing greenhouse gases, e.g. the Stern Report, Energy Technology Perspectives, and the World Energy Outlook [2-7]. The IEA projects an increase in CO_2 emissions in a business-as-usual scenario from 29 $GtCO_2$ per year today to some 62 $GtCO_2$ per year by 2050 [8]. This would be accompanied by an increase in the concentration of CO_2 in the atmosphere to approx. 550 ppm, and by a mean temperature rise of 3 °C to 4 °C. The IEA proposes two scenarios for reducing these emissions, both of which cover the period up to 2050. In the ACT Map scenario, a clear reduction in CO_2 is achieved, saving some 35 $GtCO_2$ per year by 2050 compared to the business-as-usual scenario. This would mean maintaining today's levels of CO_2 emissions in 2050, which would be equivalent to a CO_2 concentration of around 485 ppm. The BLUE Map scenario goes even further, cutting CO_2 emissions in 2050 by 48 $GtCO_2$ per year, representing a reduction of 77 % compared to the business-as-usual scenario.

This would be equivalent to a CO_2 concentration of around 445 ppm in 2050.

In both cases, power generation would make the highest contribution of any sector and CCS would lead to the biggest reductions of any individual measure. CCS would reduce CO_2 emissions in the power sector by approx. 21 % in the ACT Map scenario and by approx. 26 % in the BLUE Map scenario. The results highlight the importance of CCS technology in the global context and show how attractive CCS is if stringent greenhouse gas reduction targets are to be achieved.

Worldwide, industrial processes are responsible for almost 30 % of CO_2 emissions [9], whereby some of these emissions are process-induced. CCS can therefore also help to reduce CO_2 emissions in industrial sectors [10]. The most pertinent sectors are the cement industry, the iron and steel industry, and the production of other metals, as well as industries that process crude oil.

In contrast, the current usage of CO_2 as an industrial gas amounts to approx. 20 Mt/a and as a chemical raw material around 110 Mt/a [11]. The options for utilizing CO_2 in the future would mean that these two areas could contribute to a welcome, albeit limited, direct reduction in carbon dioxide emissions. The interest in utilizing carbon dioxide (CCU) stems primarily from the fact that CO_2 is a potentially recyclable material with an interesting application profile and great potential for the chemical industry. Carbon utilization would also positively affect the evaluation of strategies aiming to reduce CO_2 emissions if product-related CO_2 balances show a reduction in the emission of CO_2. In this way, the greenhouse gas carbon dioxide can be transformed on a limited scale into a raw material for the material value chain [12] (see schematic in Fig. 1).

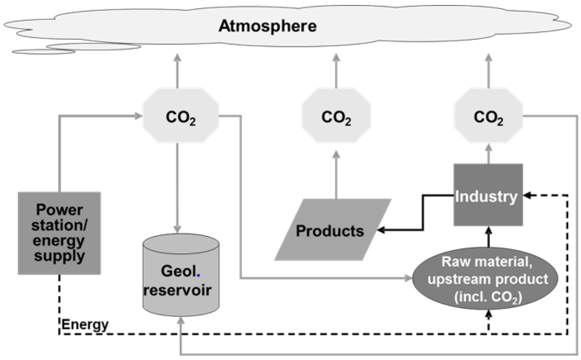

Figure 1: Schematic of carbon capture and storage as well as utilization of CO_2 as a raw material for manufacturing

In this context, capturing carbon dioxide is an important mitigation measure for CO_2 point sources in the energy conversion sector and in industry, and it is the focus of numerous research and development projects throughout the world.

At present, three technology lines are favoured for carbon capture: post-combustion, oxyfuel, and pre-combustion. Although the post-combustion and oxyfuel processes are being tested in smaller test facilities, practical demonstration is still required before first-generation technologies can be implemented on an economic and industrial scale. In the long term, interesting options could replace the currently favoured physical and chemical scrubbing using membranes, as well as carbonate looping, which count as second-generation technologies. For the oxyfuel process, the cryogenic air separation process could be improved (three-column process) and a transition to other oxygen production processes (membranes, chemical looping) is also possible.

For the storage of CO_2, a range of options are being discussed both at the national and European level. These include unused deep underground rock formations containing highly saline fluids (on-shore and under the seabed), depleted natural gas and crude oil fields (enhanced gas and oil recovery, EGR/EOR), and coal seams (enhanced coal-bed methane, ECBM). In national and international research projects, potential storage capacities are being analysed and concepts developed for the long-term and safe trapping of CO_2. With respect to the acceptance of CO_2 storage, strong reservations abound in Germany, as illustrated by the formerly planned on-shore storage facility in Schleswig-Holstein and by the discussion in Lower Saxony. At the moment, neither the general public nor politicians in the north and north-west of Germany appear to be willing to accept potential CO_2 storage sites.

While there is no lack of technical options for CCS and storage capacities are available, the question arises as to whether and under what conditions CCS could become a key element within the framework of implementing climate protection strategies. To answer this question, an Integrated Technology Assessment is required that goes beyond a purely technical evaluation. This paper therefore looks at possible implications that the technology evaluation of carbon capture and utilization could have for energy, climate, and industrial policy. First, we identify 5 key criteria and present assessment results, respectively. In a second step, an overall assessment is made resulting in key conclusions. Finally, the OECD approach for constructing composite indicators for assessing technologies is used.

II. Integrated Technology Assessment

2.1. Objective

The objective of a technology assessment is to determine the importance of a technology in relation to a set of criteria. The set of criteria selected here is rooted in the regulatory framework governing the concept of sustainable development, which has led to the need for the transformation of the energy sector in favour of sustainable technologies and systems. The principle involves investigating the development of energy technologies (and energy systems) in terms of their technical, economic, ecological, and social impacts, and thus evaluating what contribution technologies can make to the transformation of energy systems.

2.2. Methodological Approach

The range of methods for technology evaluations is very broad. They include technologically oriented methods (e.g.

risk assessments), economically oriented methods (e.g. cost analyses), politically oriented methods (e.g. voting procedures), systematic considerations (e.g. cost-benefit analyses), and methods based on systems theory (e.g. scenario techniques) [13]. IEK-STE pursues a systems analysis approach here, which focuses on the interdependencies between technologies and their associated fields in the economy, environment, and in society, and is mainly based on quantitative modelling (Fig. 2).

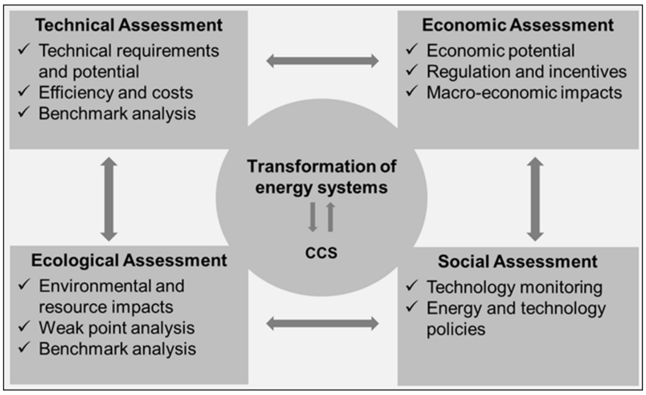

Figure 2: Methodological approach of an Integrated Technology Assessment of CCS

Our approach consists of 5 steps:

1. Criteria selection and indicator identification: Before CCS can play a decisive role in the process of implementing strategies to mitigate climate change, there are a number of key criteria that must be fulfilled. However, simply fulfilling these requirements may not necessarily be enough to guarantee the success of CCS because of the possible development of competing technologies aiming to reduce CO_2 emissions (e.g. renewables, energy efficiency).
2. Indicator level information gathering: Information on the level of indicators may result from own studies. Nevertheless, a literature review necessarily completes the basis.
3. Indicator level quantification and normalization of results: We prefer quantification of indicators as far as possible. Even if this is possible, indicators may have different units, such as ton CO_2, %, or EURO. Using normalization approaches, indicators can be translated to dimensionless ones, therefore facilitating comparison.
4. Indicator weighting: Indicators may have equal or different weights. E.g., environmental indicators may be regarded more important than others, resulting in relatively stronger weights. In other cases, this holds e.g. for economic or societal indicators.
5. Indexing: Combining individual indicators to form a composite indicator for technology assessment methodologically supports decision-making, although this may not be regarded to substitute careful interpretation of any individual indicator result.

III. Criteria, Indicators, And Information Gathering

3.1. Criteria Selection/Indicator Identification

The challenges affect all areas of an integrated technology evaluation from the technical, economic, and environmental aspects right up to the social aspects. They comprise:

- demonstration on an industrial scale and commercial availability
- environmental and safety requirements
- cost efficiency and economic viability
- coordination of energy and climate policy
- public acceptance

3.2. Indicator Level Information Gathering

In our case main information is from several chapters of [14] which is based on own studies and extensive literature review.

Demonstration on an industrial scale

According to *Markewitz and Bongartz* [15], all three technology lines have great potential to improve efficiency depending on the processes involved, although the energy penalties remain considerable. In all cases, the thermodynamic integration of the carbon capture process is particularly challenging. Interesting options exist in the long term for replacing the currently favoured physical or chemical scrubbing. Alternatives here include the use of membranes as well as carbonate looping. For the oxyfuel process, the cryogenic air separation process could be improved (three-column process), and the transition to other oxygen production processes (use of membranes, chemical looping) is also possible.

Increasing the flexibility of coal-fired power plants with and without carbon capture is one of the main challenges from a technical perspective, because an increasingly volatile feed-in of electricity into the grid will place much greater demands on the flexibility and mode of operation of power plants (e.g. higher load ramps, greater load ranges, more start-up and shut-down cycles). How well CCS power plants will be able to meet these demands is a question that cannot be answered at the moment. From a technical point of view, a basic power plant process with the highest possible efficiency is generally considered essential. The necessary significant increase in efficiencies in the basic power plant process, however, can only be achieved using ambitious live steam parameters (temperature and pressure), which in turn has negative impacts on flexibility.

It is generally assumed that CCS technology will be commercially available from 2020 at the earliest. Against the background of planned fossil-fired power plants worldwide, retrofitting with carbon capture technologies will play a particularly important role. At the moment, post-combustion appears to be the most promising technology line for retrofitting. A big advantage compared to other technology lines is that the modification of the power plant process would not involve too much effort. With respect to timely commercial availability, the current delays in investing in demonstration power plants are counter-productive.

Industrial processes (e.g. iron and steel, as well as cement production and refineries) often involve large CO_2 point sources. There is a range of options for the use of carbon capture for these processes. In the long term, considerable technical potential in Germany is seen specifically for blast furnaces, ammonia synthesis, and clinker production [16].

At present, the global contribution of the industrial utilization of CO_2 to combating climate change is quite low at 130 million tCO_2, but there is potential for improvement. Moreover, the use of CO_2 in the past for organo-chemical and inorganic applications was mainly based on industrial sources, where CO_2 is created as a joint product or an emission. Putting CO_2 to use is becoming more important from an industrial policy point of view, because CO_2 can be used as a cheap raw material, and when large amounts are needed, it can also be obtained from CCS sources. There are many possible ways of using CO_2, which should be analysed in detail with respect to their climatic relevance and their value-added potential. As global carbon emissions are increasing and will continue to do so in future, it can be assumed that the utilization of CO_2 will not replace carbon storage but will supplement it.

The relevance of utilizing CO_2 motivated by industrial policy for climate change mitigation not only depends on the amount itself, but also on the duration of CO_2 fixation [17]. The fixation potential varies widely depending on the use of CO_2 and is calculated based on the combination of small to large quantities and short to long durations of fixation. At the same time, attention should be paid to whether the activation or utilization of CO_2 requires the use of other resources or energy that would interfere with the balance of CO_2. In addition, there is a need to clarify whether the use of CO_2 from CCS sources substitutes another source that would not require geological storage. The best method for analysing the entire energy and CO_2 balance is the life cycle assessment – an established approach for evaluating the environmental impacts of processes and products. However, in practice, conclusions can only be drawn separately for each use of CO_2.

ENVIRONMENTAL AND SAFETY REQUIREMENTS

Carbon capture technologies often lead to amplification of other environmental effects [18]. The rise in other environmental effects is usually triggered by the decline in net efficiency, and the related additional requirements for fuels and chemicals (e.g. scrubbing substances), as well as increased volumes of waste. A detailed analysis of the reasons shows that optimizing the reduction of power plant emissions is in itself not enough to prevent this increase. In particular, the provision of fuel often involves a high proportion of different environmental impacts. If scrubbing substances are additionally used, the human toxicity and ecotoxicity potential rises mainly because of emissions during production. Heavy metal emissions during the dumping of hazardous waste and ash also contribute to increased toxicity. A comparison of the studies shows that the processes of the upstream and downstream chains are often not represented in the same detail as the electricity generation and subsequent carbon capture processes. These processes should therefore be investigated in more detail.

A consideration of the entire life cycle also shows that there may be local or regional environmental effects upstream. While acidification and eutrophication are reduced at power plant sites, they increase in regions where the fuel is extracted and along transportation paths.

Furthermore, a comparison with the overall effects of a region helps to relate different impacts to each other. The desired effect of reducing greenhouse gas emissions is obvious. However, more detailed consideration must be given to emissions promoting acidification and human toxicity, especially for post-combustion plants. The most important method of reducing the majority of environmental impacts is reducing efficiency losses. New technological developments, such as membranes, are promising. Nevertheless, further analyses with a detailed description of the system boundaries and the parameters are required in order to provide robust information on the respective environmental impacts of the different technologies.

Essential safety requirements concern transportation and storage activities. Pipelines are particularly interesting for transporting large amounts of CO_2 over long distances. At present, CO_2 pipelines throughout the world have a total length of more than 4000 km. The transportation of carbon dioxide is state of the art.

The release of large amounts of CO_2 can pose local risks to humans and the environment. As CO_2 is heavier than air under ambient conditions, it can collect in sinks for example, and at very high concentrations (7–10 vol.%) it can pose a life-threatening danger. Comparisons of natural gas and CO_2 pipelines show that the frequency of failures is similar. The purity of the CO_2 stream is particularly relevant for protection against corrosion. Experience with the standards in the USA can only be transferred to the European situation to a limited extent. With respect to impurities, the captured CO_2 stream in power plants is very different to the volumes of CO_2 currently transported in the USA.

Bongartz et al. [19] summarized risk assessments using probabilistic approaches. Frequencies of occurrence were assumed for the different scenarios and used as a basis for determining the ranges of critical CO_2 concentrations. The available studies were used to qualitatively evaluate the categorized transportation risks (e.g. valve leakage, leak, rupture) in terms of frequency and range of critical CO_2 concentrations with the aid of a risk matrix (frequency classes, hazard classes). The findings show that the majority of risks associated with transportation are either insignificant or very small.

Reservoir rocks with the potential for geological storage are mainly sandstones, as they are characterized by sufficient porosities and permeabilities, allowing CO_2 to be injected efficiently into these formations. Overall, four retention mechanisms in the layers of the storage formation facilitate permanent and safe storage: (i) structural retention below an impermeable caprock, (ii) immobilization via capillary binding in pore space, (iii) dissolution of CO_2 in the formation water, and (iv) mineral binding via carbonization.

Near the town of Ketzin on the Havel in Brandenburg, the first continental European field laboratory for CO_2 storage was set up and put into operation as a pilot site in 2004. The pilot site in Ketzin is thus the first and to date the only active CO_2 storage project in Germany. The injection of CO_2 is accompanied by one of the most extensive scientific research and development programmes in the world. The findings on a research scale [20] show that: (i) the geological storage of CO_2 at the pilot site in Ketzin is safe and reliable, and poses no danger to humans or the environment, (ii) a well-thought-out combination of different geochemical and geophysical monitoring methods can detect minute amounts of CO_2 and image its spatial distribution, (iii) the interactions between fluid and rock induced by CO_2 injection at the pilot site in Ketzin have no significant impacts and do not influence the integrity of the reservoir rock or the caprock, and (iv) numerical simulations can depict the temporal and spatial behaviour of injected CO_2.

COST EFFICIENCY AND ECONOMIC VIABILITY

Martinsen et al. [21] use an energy system model to estimate the monetary value of CCS technologies in Germany within the framework of greenhouse gas reduction scenarios (‘system value’ in the following). This value is determined here by the additional avoidance costs that would be incurred if climate change mitigation targets were to be achieved without CCS technologies. It is therefore an implicit measure of the level of willingness of society to pay for refraining from the use of CCS technologies.

The actual present value of the costs avoided by deploying CCS technologies for the period 2005–2050 is approx. $€_{2010}$ 100 billion. The value is calculated by balancing across all sectors (end-use, conversion, primary energy incl. imports). In the end-use sectors (industry, households, traffic and transport, commerce, trade and services), relatively expensive savings measures can be avoided if CCS is implemented in the conversion sector. In the same way, the primary energy sector including imports also plays a role, where most of the additional costs associated with the import of biomass products (e.g. bioethanol) are avoided when CCS is implemented, but additional costs are incurred for fossil fuels, which predominate until 2035. Despite the costs caused by CCS technologies, the conversion sector also contributes to the system value because an additional increase in renewable energy capacity is avoided. Overall, this applies to all sectors but the extent is very different.

The construction of CCS facilities represents an investment with long-term and high capital tie-up. In addition, the projections of the plant costs for CCS power plants still involve uncertainties, despite the continuing development of demonstration facilities. Increased knowledge and ongoing technological development lead to the investment costs of the first commercial CCS plants being predicted as 70–90 % higher than those of conventional plants. The costs for the transportation and storage of CO_2 depend on the quantities to be transported, the transport distance, and the type and location of the geological storage facility, and they vary considerably. In all cases, the costs of capturing CO_2 dominate.

Even high plant utilization gives rise to much higher electricity generation costs, particularly for coal-based CCS plants (lignite: +80 %) [22]. The CO_2 avoidance costs are € 34–38/tCO_2 (lignite), € 41–48/tCO_2 (hard coal), and approx. € 67/tCO_2 for natural gas plants. Only if the price of allowances rises to the same level will the use of CCS power plants during normal operation be cost-effective.

A very low number of full-load hours tends to cause the CO_2 avoidance costs to double. As a result, a relatively high CO_2 price would be necessary to justify operation with a low number of full-load hours.

CCS power plants must be refinanced through the electricity market. Furthermore, the use of CCS power plants can have an effect on the price of electricity on the wholesale market under certain conditions. The price on the electricity market is determined by the costs of the last power plant used, whereby the power plants are used in order of their marginal costs (merit order) and the costs for electricity imports must be considered.

In general, the question arises as to the degree to which potentially higher revenues due to merit order effects cover the additional investment costs for CCS power plants. Owing to the high uncertainties with respect to the additional investment costs, it can be assumed that CCS plants will only become interesting to investors when the allowance price is at least € 40/tCO_2. Development in the area of renewable energy must also be considered. The increased use of renewables will lead to a decrease in the average annual price on the electricity market as long as sufficient ‘cheap’ back-up capacities are available, i.e. power plants with low operating costs. In addition, merit-order effects arise where the use of CCS also dampens the price of electricity. Merit-order effects also tend to boost the level of domestic production. It should be noted that this could cause reciprocal effects. Price effects caused by the increased use of renewable energy will make it more difficult to refinance CCS power plants, and the electricity price effects of CCS power plants will reduce the revenues for renewable energy (which in turn impacts on the level of Renewable Energy Act (EEG) surcharges).

If renewable energy is further integrated into the electricity system, with the current market design (‘energy only’) there is a danger that the power plant capacities of an existing fleet will be potentially underused. In addition to the generation cost effect caused by a low number of full-load hours, the drop in residual demand would lead to a merit order effect. As a result, there would be a short-term cost recovery problem for fossil plants in the installed power plant fleet. Regardless of the possible concrete design of capacity markets, the comparatively high refinancing needs compared to conventional power plants will prevail if capacity revenues are incorporated.

The use of CCS as a CO_2 mitigation measure for industrial plants is technically feasible in principle, but neither demonstration nor commercial CCS plants are currently in operation on the industrial scale. As a result, estimates for plant costs continue to be associated with great uncertainties.

A cost analysis of a cement plant with a capacity of 1 million tonnes of cement per year shows an increase of 32 % in production costs when oxyfuel technology is used [23]. In the case of carbon capture with post-combustion technology, production costs increase by about 100 %. Retrofitting an oil refinery with a capacity of 10 million tonnes of crude oil per year with oxyfuel technology leads to an increase of roughly 15 % in processing costs. This results in CO_2 avoidance costs of about € 55/tCO_2 for the oxyfuel cement plant, and about € 62/tCO_2 for the oxyfuel refinery. Avoidance costs are much higher for the cement plant with post-combustion capture (€ 143/tCO_2).

COORDINATION OF ENERGY AND CLIMATE POLICY

The policy-making process anchoring CCS as a climate change mitigation option in the EU was executed at a remarkable speed [24]. Faced with two options – the mandatory introduction of CCS or the development of a framework for the industrial implementation of CCS – the EU institutions decided in favour of the second option. Between 2005 and 2009, European institutions successfully established CCS as a cornerstone of the EU's integrated energy and climate policy, developed a legal framework for geological storage, incorporated CCS into the European emissions trading system, and elaborated funding instruments for CCS. This dynamic momentum makes the EU one of the pioneers internationally. Despite this, feedback with respect to the implementation of CCS policy is less positive. The implementation of the CCS Directive reveals the lack of consensus on whether CCS should be used as an option for combating climate change. Today, some European countries, such as Austria, are completely against carbon storage.

The emissions trading system (EU ETS) and the demonstration programme (EEPR, NER300) are instruments that support CCS. However, the majority of companies are hesitant to invest in demonstration projects at the moment. The role of NER300 financing as one of the main instruments supporting CCS demonstration projects in Europe is being increasingly questioned in this context. The instrument attracted criticism from the very beginning because of the uncertainty regarding the price level of allowances. Pessimistic expectations were confirmed by initial experiences trading the allowances. The low price for emissions allowances also ignited discussions on the competitiveness of CCS technology after the demonstration phase. Long-term incentives are decisive for a stable development of low-carbon technologies. Within the scope of these instruments, an EU ETS cap, a carbon tax, and a bonus-malus system are being discussed as part of a carbon standard.

Attitudes towards CCS as a climate change mitigation option have undergone rapid development over the last ten years from initial euphoria to cautious restraint [26]. The development of international cooperation reflects these changes. The recognition of CCS as a potential method for combating climate change with the publication of the IPCC Special Report was accompanied by the establishment of several international organizations and new priorities in existing collaborations. The G8, IEA, and Carbon Sequestration Forum (CSLF) aim to facilitate the timely commercialization and demonstration of CCS.

However, the period between 2008 and 2010 is characterized by the discontinuation of several internationally important CCS projects. This means that the G8's aspiration of initiating 20 integrated demonstration projects worldwide by 2010 was not met. Despite approaches, such as the recognition of CCS demonstration projects by the CSLF or the creation of the Global Carbon Capture and Storage Institute (GCCSI) in Australia, no international cooperation has succeeded in furthering the demonstration of CCS. A decisive prerequisite has yet to be implemented – the introduction of a sufficiently high CO_2 price in the main emitter countries.

Germany's CCS Act, for example, shows that there is neither consensus on a national prohibition nor on the demonstration of the commercial application of CCS. The answer to the question of whether CCS is an option for Germany for reducing CO_2 emissions has been pushed into an uncertain future by the Act [27].

Compared to the first bill in 2009, the adopted CCS Act has shrunk to a research law with a theoretical potential for smaller demonstration projects which will probably not be exploited in Germany. If the potential of CCS should be demonstrated for large power plants or for industrial plants, the Act would have to be amended with respect to the storage amounts. In 2017, the CCS Act will be evaluated, and the discussion on CCS could become heated once again.

A minority of explicit political advocates of CCS hope that suitable energy economy and European framework conditions will emerge in future. The advocates include the state governments of Brandenburg, Saxony, and Saxony-Anhalt. In North Rhine-Westphalia, where in 2010 around 54 % of German lignite was mined, the last word has yet to be spoken on lignite policy and thus indirectly on the implementation of CCS.

A clearer picture will emerge over the next few years as to whether the targets for expanding the capacity of renewables will be achieved and how smooth the transformation of the energy system will be [28], what role coal in general and lignite-fired base-load power plants could play, and how emissions trading and its CO_2 prices (EU ETS) will develop. Should it emerge that the EU and its member states are not in a position to implement their extremely ambitious action plan for CO_2 mitigation politically or economically, e.g. because international climate change mitigation goes along with the less demanding willingness of states to act to mitigate CO_2 (bottom-up), the perspectives for CCS could become more clouded. The EU's CCS policy could also have an impact, e.g. possible additional CCS regulations, making CCS mandatory for new as well as for old power plants. CCS plays a key role in the EU plan for a low-carbon economy in 2050 [29] and the more specific 2050 Energy Roadmap [30], even though commercial application is not expected until after 2030 and

CCS projects are not progressing well in the EU member states.

Another obstacle for CCS is the lack of acceptance for the solution of the 'back-end' CCS problem, namely storage. The northern federal states in Germany will pull out all the stops to block even potential storage projects. This problem might be less virulent if CO_2 were to be stored below the seabed (off-shore), particularly within the context of enhanced oil/gas recovery. Research work is being conducted on storage in deep ocean sediments, the safety of such sites, and on the consequences of leaks for the marine environment, which also includes regions off the German coast. It remains to be seen whether a 'loophole' [31] will emerge for federal storage projects below the seabed. That CCS opponents take this option seriously is reflected in the coalition agreement of the new state government in Schleswig-Holstein: it wants to 'preclude' CCS 'for the whole of Germany – particularly in the exclusive economic zone.' [32]. For this reason, should a European CO_2 transportation infrastructure be created, CO_2 could be exported to onshore storage sites in other countries or injected into their deep ocean sediments. The statements issued in response to the legislative compromise indicate an interest in this option in sections of the political and industrial arenas. Assuming that there is interest in carbon capture in Germany and that the respective transportation infrastructure existed, then the acceptance of CO_2 pipelines through the federal states would also have to be ensured – considering the massive opposition to the planned Hürth pipeline in 2008, this represents a huge challenge for politics and society. It may be mastered if CCS were to be considered independently of lignite and if it were to become an integral part of a comprehensive strategy for a low-carbon society that would bring advantages with it for citizens, the economy, and the environment. Within the framework of the Rotterdam Climate Initiative, [1] an attempt is being made to implement this strategy. Germany can learn from this social experiment.

PUBLIC ACCEPTANCE

The acceptance of technologies cannot yet be reliably measured because the population still knows too little about CCS technologies [33]. CCS acceptance research therefore focuses on investigating awareness and knowledge of CCS as well as spontaneous attitudes towards it among the general public. Such studies also concentrate on identifying factors that have an impact on spontaneous attitudes towards the technologies as well as on analysing the impact of information and methods of communication on changes in and the stability of spontaneous attitudes.

With respect to how well known CCS is among the general public, the findings of international and national studies confirm that at least awareness of the concept of 'carbon capture and storage' has increased considerably over the course of time. The increasing awareness of the concept of 'carbon capture and storage', however, is not accompanied by an increase in knowledge of the technologies. As the findings of international and national studies show, misconceptions about CCS (still) abound among the general public. This can be explained by the fact that lay people often find it difficult to distinguish between environmental problems, such as ozone depletion, global warming, acid rain or smog.

In addition, information on CCS and the communication of CCS should consider the fact that citizens have spontaneous attitudes towards the technologies even though they know little or nothing about CCS. In Germany, these spontaneous attitudes towards CCS are on average (still) mainly neutral, although women are more sceptical of the technologies than men.

The regional differences in spontaneous attitudes before and after the receipt of information demonstrate that citizens of Schleswig-Holstein do not only have more negative attitudes towards CCS than citizens of the region along the Rhine or of the 'rest' of Germany, but that the debate surrounding carbon storage in Schleswig-Holstein has already led to the emergence of negative attitudes towards CCS in this region which are not necessarily spontaneous attitudes any more but rather stable opinions. As the present findings also suggest, these negative attitudes in Schleswig-Holstein are mainly related to the fact that citizens here consider the personal risks associated with carbon storage to be much greater than citizens of the other regions.

However, the results also illustrate that spontaneous attitudes towards CCS in all regions are most heavily influenced by the perception of the social benefits of the technologies and that this influence is positive: the greater the social benefits of CCS, the more positive the spontaneous attitudes towards the technologies.

How stable these perceptions of the benefits of CCS are or how easily they can be changed by new information cannot be conclusively analysed using the present findings as a basis. The influence of information on the perception of the benefits of CCS, as well as the influence of the perception of benefits on the stability of attitudes towards CCS, must therefore be systematically investigated in future studies in order to assess the importance of the perception of benefits as an indicator for evaluating the future public acceptance of CCS in Germany.

At the moment, the lack of acceptance for the solution to the 'back-end' problem associated with CCS, namely storage, in the northern federal states is blocking all potential storage projects. Policies and legislation on CCS in Germany clearly reflect this negative stance, even if CCS is emphasized as a (necessary) option for energy-intensive and carbon-intensive industries.

3.3. Key Conclusions

The preceding deliberations explain the challenges considered to be most important for technology evaluation. What big picture emerges? What is the success factor like as a whole? And how sensitive is the result with respect to the separate challenges?

The greatest success factor applies to the safety requirements for the transportation and storage of CO_2. The assessment of the environmental requirements from a life

[1] http://www.rotterdamclimateinitiative.nl.

cycle perspective, however, is cause for concern in that the envisaged reduction in the global warming potential may lead to other environmental impacts, such as eutrophication, and thus induce regional shifts in environmental impacts. With a view to public acceptance, no conclusions can be drawn at this point because the public does not yet know enough about CCS technologies. Irrespective of this, the public still forms opinions on CCS technologies, which are characterized by the negative attitudes, e.g. in the northern federal states where potential storage sites are located. This negative attitude is also reflected in the national CCS Act, which does not permit commercial storage of large quantities of CO_2. Implementation on an economic and industrial scale has not yet been demonstrated in Europe despite EU financial incentive systems. As a result, commercial availability is not likely in the near future. Compared to the CO_2 avoidance costs of other large technical options, those of CCS technologies are average, but the electricity generation costs increase rapidly and incentives to invest in the technologies are not enough. The price of CO_2 is currently low and the number of full-load hours is dropping due to the increasing integration of renewable technologies, which means that refinancing the high investment costs is too uncertain in today's market design. With respect to political factors, the outcome of the overall evaluation is negative. The EU appears to be an institutional driving force for CCS technologies, promoting them in its energy, climate, and technology policy. However, this is not as successful as it may appear. Internationally, the euphoria surrounding CCS has dissipated, and CCS advocates in Germany (such as those in individual state governments) can only hope for improvements in future. Should climate change mitigation in Germany prove to be insufficient using the options currently preferred within the framework of the transformation of the energy sector, there may be re-evaluation of CCS in Germany. Even though none of this can yet provide a decisive answer to the question of whether CCS has a future in Germany or not, the economic climate combined with the political and social balance of power imply that CCS is doomed to failure.

IV. Composite Indicator

Methodologically, an approach used by the OECD for a composite indicator and applied in its technology evaluations is taken here [34]; it combines individual indices to form an overall index.

$$I = \sum_{i=1}^{n} w_i * x_i \quad (1)$$

$$\sum w_i = 1; \;\; 0 \leq w_i \leq 1 \quad (2)$$

with I: overall index, x_i: individual index, w_i: weighting factor for index I, and n: number of indices.

4.1. Normalization and weighting

First, each criterion (= individual index) is assigned a success factor *x* on a scale of 1 to 5. The lower the scale value, the worse the technology assessment with respect to the criterion is. Conversely, the higher the scale value, the better the assessment (TABLE 1).

Based on expert interviews at IEK-STE criterion (2) 'environmental and safety requirements' is most successfully fulfilled (rating of 3.00), although 3.00 does not even come close to achieving the maximum, and criterion (5) 'public acceptance' (rating of 1.32) least successfully. Criterion (1) 'demonstration, commercial availability' was also evaluated relatively positively (rating of 2.84), while (3) 'cost efficiency and economic viability' fared poorly with a rating of 1.86.

TABLE 1, Expert Rating and weighting of the indicators

Criterion	Expert rating	Priorities and Weighting			
		Equal	Environment	Economy	Society
1. Demonstration, commercial availability	2.84	0.2	0.125	0.125	0.125
2. Environmental and safety requirements	3.00	0.2	0.5	0.125	0.125
3. Cost efficiency and economic viability	1.86	0.2	0.125	0.5	0.125
4. Coordination of energy and climate policy	2.21	0.2	0.125	0.125	0.125
5. Public acceptance	1.32	0.2	0.125	0.125	0.5

Furthermore, weightings w are introduced to account for the fact that the criteria could affect the overall assessment in different ways. The sum of the weighting factors is always 1. The case where the criteria are weighted equally is analysed as the base case. It implicitly exists whenever – supposedly – weighting is not used. The chosen methodology means that the overall index can have values between 1 and 5. Additionally, cases are introduced, focusing either on environmental, economic, or societal foci by giving them more weight (0.5). In order to fulfil formula 2, in these cases the corresponding criteria have lower weights because of formula 2.

Fig. 3 shows the contribution of individual indices to the results based on different weightings. Observed from different perspectives (equal weighting or weighting foci) the results differ and are not easily comparable. However, the results support the interpretation that the attractiveness of CCS technologies is mainly influenced by criterion 2, 3, or 5, depending on the weighting focus. In case the weighting focus is on environment, then criterion 2 (environmental and safety requirements) is of main importance. In our case, the result is due to the relative optimistic expert rating of criterion (2) 'environmental and safety requirements' (rating of 3.00 of 5.00 maximum).

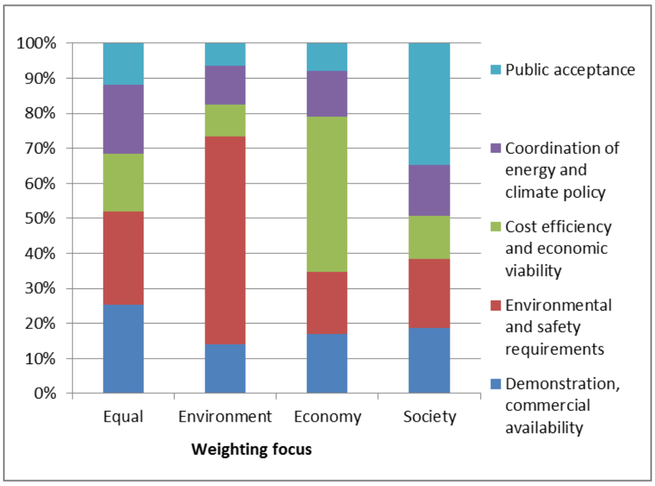

Fig. 3, Relative importance of individual indices based on different weighting foci.

4.2. Overall Index

In order to fully support the OECD approach of technology assessment a composite indicator was calculated based on formula (1). The calculations result to indices for the four weighting cases (Fig. 4). The CCS technologies indeed are most attractive if the weighting focus is on environmental perspective, followed by the equal weighting concept. The technologies are less attractive if societal concerns are in the foreground. Fig. 4 also shows that the index even in the best case is far less than the possible maximum 5.

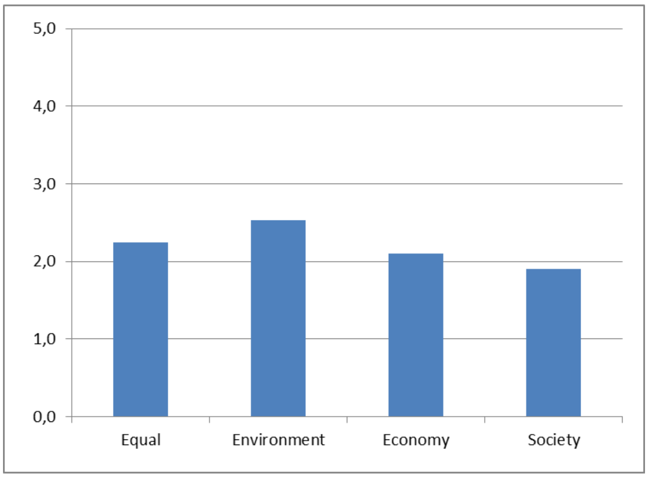

Fig. 4, Composite indicator based on different weightings.

V. CONCLUSIONS

The aim of the paper was to analyze the potential and the possible role of CCS technologies as an option for reducing emission of energy-related CO_2. Methodically, the paper is based on Integrated Technology Assessment, for which the OECD approach of a composite index for assessing technologies is used. The chosen approach needs 5 steps: (1) criteria selection and indicator identification, (2) indicator level information gathering, (3) indicator level quantification and normalization of results, (4) indicator weighting, and (5) aggregation to a composite index.

For this approach, 5 criteria are identified: (1) demonstration on and industrial scale and commercial availability, (2) environmental and safety requirements, (3) cost efficiency and economic viability, (4) coordination of energy and climate policy, and (5) public acceptance. For weighting, 4 cases are tested: (1) equal weighting, (2) environmental focus, (3) economic focus, and (4) societal focus.

The results support the interpretation that CCS technologies may be regarded an attractive option if the focus is on environment. In our case, the result is due to the relative optimistic expert rating of criterion (2) ‘environmental and safety requirements’ (rating of 3.00 of 5.00 maximum). The composite index indeed shows that CCS is most attractive from an environmental perspective, followed by the equal weighting concept. CCS technologies are less attractive if societal concerns are in the foreground. In the case of Germany, it is mainly the level of public acceptance that fails to support CCS.

References

[1] S. Pacala and R. Socolow, "Stabilization wedges: Solving the climate problem for the next 50 years with current technologies," *Science*, vol. 305, pp. 968-972, 2004.

[2] IEA, *World energy outlook 2009*: International Energy Agency IEA/OECD, Paris, 2009.

[3] IEA, "Energy technology perspectives - scenarios & strategies to 2050," OECD/IEA, Paris2010.

[4] IEA, *World energy outlook 2011*: International Energy Agency OECD/IEA, Paris, 2011.

[5] IEA, "World energy outlook 2012," IEA, ParisNov 16, 2012 2012.

[6] N. Stern, "Stern review: The economics of climate change," London, http://webarchive.nationalarchives.gov.uk/+/http://www.hm-treasury.gov.uk/stern_review_report.htm, 21.06.20122006.

[7] IEA, "Energy technology perspectives 2012," IEA, Paris2012.

[8] IEA, "Energy technology perspectives - scenarios & strategies to 2050," International Energy Agency IEA/OECD, Paris2008.

[9] IEA, "Energy technology transitions for industry," International Energy Egency IEA/OECD, Paris2009.

[10] J. Gale, "Challenges and opportunities of CO_2 capture and storage for the iron and steel industry," IEA GHG, London2012.

[11] M. Peters, B. Köhler, W. Kuckshinrichs, W. Leitner, P. Markewitz, and T. E. Müller, "Chemical technologies for exploiting and recycling carbon dioxide into the value chain," *ChemSusChem, Special Issue: Carbon Dioxide Recycling*, vol. 4, pp. 1216-1240, 2011.

[12] F. Ausfelder and A. Bazzanella, "Verwertung und Speicherung von CO_2," DECHEMA, Frankfurt2008.

[13] O. Renn. (2010, Methoden und Verfahren der Technikfolgenabschätzung und der

Technologiebewertung. Available: www.elib.uni-stuttgart.de/opus/volltexte/2010/5286/pdf/ren2.pdf

[14] W. Kuckshinrichs and J.-F. Hake, (Eds.), *Carbon capture, storage and use. Technical, economic, environmental and societal perspective*. Dordrecht: Springer, 347 pages, 2015.

[15] P. Markewitz and R. Bongartz, "Carbon capture technologies," in *Carbon capture, storage and use*, W. Kuckshinrichs and J.-F. Hake, Eds., ed Dordrecht: Springer, 2015, pp. 13-45.

[16] McKinsey, "Kosten und Potenziale der Vermeidung von Treibhausgasemissionen in Deutschland - Sektorperspektive Industrie," Mc Kinsey&Company, Inc.2007.

[17] T. E. Müller, W. Leitner, P. Markewitz, and W. Kuckshinrichs, "Opportunities for utilizing and recycling CO_2," in *Carbon capture, storage and use*, W. Kuckshinrichs and J.-F. Hake, Eds., ed Dordrecht: Springer, 2015, pp. 67-100.

[18] A. Schreiber, P. Zapp, and J. Marx, "Environmental aspects of CCS," in *Carbon capture, storage and use*, pp. 147-171.

[23] J. Fleer and W. Kuckshinrichs, "Cost analysis for CCS in selected carbon-intensive industries " in *Carbon capture, storage and use*, W. Kuckshinrichs and J.-F. Hake, Eds., ed Dordrecht: Springer, 2015, pp. 173-182.

[24] O. Schenk and J.-F. Hake, "CCS policy in the EU: Will it pay off or do we have to go back to square one?," in *Carbon capture, storage and use*, W. Kuckshinrichs and J.-F. Hake, Eds., ed Dordrecht: Springer, 2015, pp. 287-309.

[25] ZEP. (2011, Juni 29). *CCS state of play, Dr. Graeme Sweeney, Chairman, ZEP & EVP, CO_2, Royal Dutch Shell*. Available: http://www.zeroemissionsplatform.eu/events/details/136-zepga2011.html

[26] J.-F. Hake and O. Schenk, "International cooperation in support of CCS," in *Carbon capture, storage and use*, W. Kuckshinrichs and J.-F. Hake, Eds., ed Dordrecht: Springer, 2015, pp. 311-327.

[27] W. Fischer, "No CCS in Germany despite the CCS Act?," in *Cabon capture, storage and use*, W. Kuckshinrichs and J.-F. Hake, Eds., ed Dordrecht: Springer, 2015, pp. 255-286.

[28] K. Mikulcak, "German government backtracks on the Energy Transition," *European Energy Review, 12 July 2012,* W. Kuckshinrichs and J.-F. Hake, Eds., ed Dordrecht: Springer, 2015, pp. 101-126.

[19] R. Bongartz, J. Linssen, and P. Markewitz, "CO_2 transportation," in *Carbon capture, storage and use*, W. Kuckshinrichs and J.-F. Hake, Eds., ed Dordrecht: Springer, 2015, pp. 47-65.

[20] M. Kühn, A. Liebscher, S. Martens, F. Möller, T. Kempka, and M. Streibel, "Safe operation of geological CO_2 storage using the example of the pilot site in Ketzin," in *Carbon capture, storag and use*, W. Kuckshinrichs and J.-F. Hake, Eds., ed Dordrecht: Springer, 2015, pp. 127-143.

[21] D. Martinsen, H. Heinrichs, P. Markewitz, and W. Kuckshinrichs, "The system value of CCS technologies in the context of CO_2 mitigation scenarios for Germany," in *Carbon capture, storage and use*, W. Kuckshinrichs and J.-F. Hake, Eds., ed Dordrecht: Springer, 2015, pp. 201-220.

[22] W. Kuckshinrichs and S. Vögele, "Economic analysis of carbon capture in the energy sector," in *Carbon capture, storage and use*, W. Kuckshinrichs and J.-F. Hake, Eds., ed Dordrecht: Springer, 2015 *http://www.europeanenergyreview.eu/site/pagina.php?id=3799#artikel_3799*, 2012.

[29] European Commission, "A roadmap for moving to a competitive low carbon economy in 2050," Brussels, Communication from the Commission, COM/2011/0112 final, http://eur-lex.europa.eu/LexUriServ/LexUriServ.do?uri=CELEX:52011DC0112:EN:NOT2011.

[30] European Commission, "Energy roadmap 2050," European Commission, Brussels, COM(2011) 885 final, http://eur-lex.europa.eu/LexUriServ/LexUriServ.do?uri=COM:2011:0885:FIN:EN:PDF2011.

[31] CO_2 Handel. (2011). *Bund schafft sich Schlupfloch im CO_2-Speichergesetz.*

[32] SPD/Grüne/SSW, "Bündnis für den Norden. Koalitionsvertrag 2012 bis 2017," Kiel, http://www.sh.gruene.de/cms/default/dokbin/411/411582.koalitionsvertrag_spd_buendnis90die_grue.pdf2012.

[33] D. Schumann, "Public acceptance," in *Carbon capture, storage and use*, W. Kuckshinrichs and J.-F. Hake, Eds., ed Dordrecht: Springer, 2015, pp. 221-251.

[34] OECD, *Handbook on constructing composite indicators*. Paris: OECD http://www.oecd.org/std/leadingindicatorsandtendencysurveys/42495745.pdf, 2008.

Journal of Energy Challenges and Mechanics
http://www.nscj.co.uk/JECM/
ISSN 2056-9386
Volume 2 (2015) issue 4, article 2

The role of deformation history of buckle folds on sustainable pore pressure magnitudes

褶皱构造过程对于可持续孔隙压力影响的研究

Andreas Eckert[1*], Xiaolong Liu[1]

[1] *Department of Geosciences and Geological and Petroleum Engineering, Missouri University of Science and Technology, Rolla, MO 65409, USA*

eckertan@mst.edu

Accepted for publication on 22nd October 2015

Abstract - **Subsurface engineering applications such as waste water disposal or CO_2 sequestration require the selection of suitable injection sites which depends critically on the assessment of geomechanical risks such as fracture initiation or fracture reactivation. As an analogue to hydrocarbon production sites, buckle fold structures are a preferred structural trap for fluid storage and become of interest for waste water disposal or CO_2 sequestration. In this contribution, 3-dimensional finite element analysis is used to quantify the influence of different permeability distributions in a multi-layer visco-elastic buckle fold system on the resulting state of stress throughout the deformation history of the fold. Based on the advanced, tensor-based concept of pore pressure – stress coupling, pre-injection analytical estimates of the maximum sustainable pore pressure change, ΔPc, for fluid injection scenarios can be calculated if the state of stress of a geologic structure can be quantified using numerical models. The results of this study show that the minimum ΔPc is varying throughout the deformation history of multilayer buckle folds and different locations within the structure show great variability in ΔPc. Furthermore, the permeability distribution of the various layers in the multilayer fold system has great influence on minimum ΔPc. It is concluded that geomechanical risk assessment for active fold belts needs to consider the complete deformation history of geologic structures such as buckle folds.**

Keywords – **multilayer buckle folds, sustainable pore pressure, deformation history, erosional unloading.**

关键词 – 多岩层弯曲褶皱，可持续孔隙压力，构造变形史，剥蚀反弹。

I. Introduction

The reactivation of critically stressed fractures due to subsurface fluid injection represents a geomechanical risk for applications such as waste water disposal or geologic CO_2 sequestration. As shown by [1], the lower limit of sustainable subsurface pore pressures is determined by the threshold of reactivation of optimally oriented, cohesionless shear fractures. If reactivated these fractures represent fluid flow pathways [2] which may connect the fluid reservoir to the surface or to fresh water aquifers and fluid injection related seismicity is observed [3-7]. Geomechanical risk assessment of fracture reactivation [e.g. 6, 8-13] requires a thorough understanding of the in situ state of stress and the pore pressure distribution and evolution, which often involves extensive numerical modeling studies coupling geomechanics to fluid flow through porous media [10,12,14-17]. As a result from these studies it has been concluded that the fluid flow boundary conditions [10,18,19] and the in situ stress regime [10,11,20] are the key parameters determining the likelihood of fracture reactivation.

As an alternative the tensor based concept of pore pressure – stress coupling [21,22] can be used to calculate analytical pre-injection estimates of the maximum sustainable pore pressure [20]. The pore pressure – stress coupling (PPSC) theory states that the principal stress magnitudes change with a change in pore pressure. [22] showed that PPSC is different for different stress regimes and that (for a homogenous full space) the risk of fault reactivation is highest along the maximum principal stress direction. The homogeneous full space modeling results by [22] imply on the assumption of the prevailing stress regimes being Andersonian (i.e. compressional, strike-slip and extensional). [20] showed that the PPSC principle can be applied to any state of stress and thus be applied to complex geologic structures where stresses are not Andersonian. As long as the principal stress magnitudes and orientations can be determined (e.g. using numerical modeling approaches such as finite element analysis) the maximum sustainable change in pore pressure magnitude, ΔP_c, prior to injection can be calculated for the complete structure. PPSC accounts for the poro-elastic effects and over- or underestimations of ΔP_c can be minimized [11,22].

For safe long term sub-surface storage of fluids natural geologic trap systems such as fold structures become of primary interest. In their study, [20] have applied the PPSC principle to anticline structures subject to different stress regimes and different levels of inter-layer coupling using 3D finite element analysis. However, the anticline structures considered are based on static representations of stress and pore pressure, i.e. the specific strain path of how the geologic system evolved is not considered. [23-25] have shown that the stress and pore pressure distribution in single- and multi-layer buckle folds vary significantly throughout the deformation history and with respect to the permeability distribution of the modeled layers. In addition to the structural development, post-deformation processes such as erosional unloading during exhumation have significant influence on the resulting stress distribution [23,26].

In this contribution, 3D finite element analysis is used to simulate the stress and pore pressure distribution of visco-elastic multi-layer buckle fold systems. The modeled fold systems are characterized by permeability distributions resembling favorable cap rock (i.e. low permeability) and injection layer (i.e. high permeability) sequences. Based on the resulting state of stress and pore pressure evolution of the fold system during the deformational history (including erosional unloading strain paths) the maximum sustainable pore pressure change, ΔP_c, is quantified and the risk of fracture reactivation assessed.

II. Pore Pressure – Stress Coupling

In contrast to the to the previous concept of PPSC described by [27,28], not only the minimum horizontal stress, but all principal stress components are affected by changes in pore pressure [21,22]. As a result the ratio of $\Delta\sigma_{ij} / \Delta P$ is a complex function of space ($\vec{x}$) and time (t) and has tensor character. The simplification of the long term limits (i.e. $t \rightarrow \infty$; which becomes relevant for subsurface fluid injection scenarios requiring an estimate of the sustainable pore pressure change over long time periods) results in the following coupling ratios for the radial (σ_{rad}) and tangential (σ_{tan}) stress components [29] in a principal coordinate system (Figure 1; after [21]) are given:

$$\lim_{t\rightarrow\infty} \frac{\Delta\sigma_{rad}(\vec{x},t)}{\Delta P(\vec{x},t)} = \alpha \frac{1-2\nu}{1-\nu} \quad (1)$$

$$\lim_{t\rightarrow\infty} \frac{\Delta\sigma_{\tan}(\vec{x},t)}{\Delta P(\vec{x},t)} = \frac{1}{2} \alpha \frac{1-2\nu}{1-\nu} \quad (2)$$

where α represents the Biot coefficient and ν the Poisson's ratio. The full tensor solution of the PPSC equations are given in [20,21]. [21] showed that based on the new effective stress tensor after injection the maximum sustainable pore pressure, P_c, for fault reactivation can be derived for each principal stress direction. They also show that the lowest P_c is obtained for the σ_1 direction and is given by:

$$P_c = \frac{b\sigma_3 - \sigma_1 - \left(\alpha \frac{1-2\nu}{1-\nu}\right)\left(\frac{b}{2}-1\right)P}{\alpha \frac{1-2\nu}{1-\nu}\left(1-\frac{b}{2}\right) - (1-b)} \quad (3)$$

where b is given by $b = \frac{1+\sin\phi}{1-\sin\phi}$, with ϕ being the angle of internal friction, and P is the initial pore pressure. The maximum sustainable change in pore pressure magnitude, ΔP_c,is then calculated by:

$$\Delta P_c = P_c - P \quad (4)$$

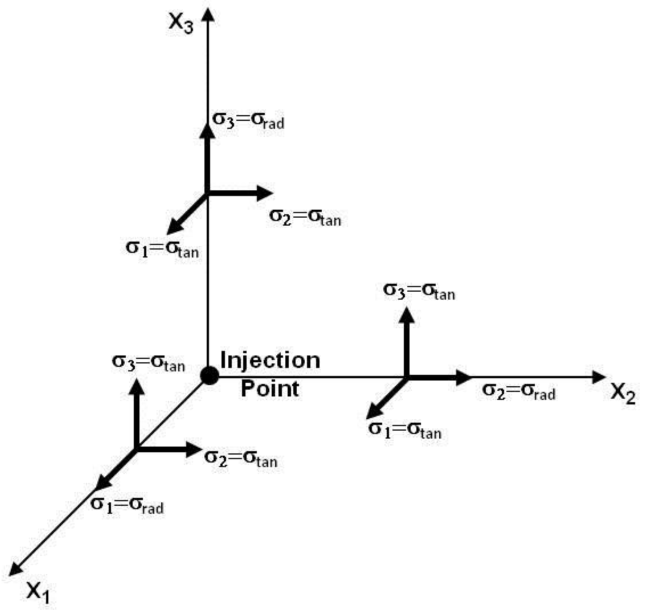

Figure 1: Principal axis coordinate system with different stress components, σ_1, σ_2, and σ_3, which are represented as radial and tangential stresses along different axes with respect to the injection location (after [21]).

III. Numerical Modeling Approach

2.1. Visco-elastic Buckle folding

In this study a classic Maxwell model (allowing instantaneous elastic behavior for high strain rates and time dependent viscous behavior for low strain rates) is adopted to simulate visco-elastic, multi-layer layer, cylindrical buckle fold systems [23-25]. Pore pressure is introduced by utilizing effective stress analysis assuming an incompressible fluid and rock matrix, i.e. utilizing a Biot coefficient of α=1 [30]. The governing equation system is presented in detail by [23] and thus not repeated here. A 3D finite element analysis (FEA; via the commercial software package ABAQUS™) is employed to solve the equations of equilibrium, conservation of mass, constitutive equations, and the equations for pore fluid flow.

The numerical models are setup such that only one wavelength, i.e. the dominant wavelength λ_{dv} ($\frac{\lambda_{dv}}{h} = 2\pi\sqrt[3]{\frac{N\mu_f}{6\mu_m}}$, where N is the number of competent layers, h is the layer thickness; μ_f and μ_m represent the viscosities of the folded layer and the surrounding rock matrix, respectively) is amplified [23]. As presented in [23,24] the parameter R (the ratio between the viscous dominant wavelength, λ_{dv}, and the elastic dominant wavelength, λ_{de}) is utilized to determine whether the competent layer is folded viscously (R<1) or elastically (R>1) [31,32]. Based on the material properties used (i.e. μ_f = 10^{21} Pa s, G ≈12 GPa) R equals 0.134. This indicated predominantly viscous deformation and an appropriate viscous dominant wavelength of 630.96 m is chosen for the geometry of the initial perturbation.

2.1. Model Setup

The 3D model geometry features a multi-layer fold structure comprised of 5 layers, of 30m thickness each, embedded in a rock matrix of varying thickness (Figure 2; Table 1). The horizontal model dimensions are 150 m by 2839 m. The 5 fold layers are characterized by small periodic perturbations of the viscous dominant wavelength with 2.5m amplitude. The 5 fold layers and the matrix surrounding them feature a viscosity and stiffness contrast (Table 1), whereby Layers 1, 3, and 5 represent the more competent layers (i.e. having higher Young's modulus and higher viscosity). In addition to the competence contrast different permeabilities are assigned to the matrix and fold layers to represent a cap rock – injection layer sequence (Table 1). Considering the significant overburden load applied in this study, initial porosity decreases with depth and is assigned after [33]:

$$\varphi(z) = 16.39e^{-0.00039z} \tag{5}$$

where ϕ is the porosity (%), and z is the depth in meters below the top of the overburden. Furthermore, since permeability also changes with depth, the relationship given by [33] is modified and applied to represent high and low horizontal permeabilities in models with overburden less than 1500 meters as:

$$k_H(z) = 7.583\cdot10^{-17} e^{0.283\phi} \tag{6}$$

$$k_H(z) = 7.583\cdot10^{-23} e^{0.283\phi} \tag{7}$$

and in models with overburden more than 1500 meters as:

$$k_H(z) = 7.583\cdot10^{-16} e^{0.283\phi} \tag{8}$$

$$k_H(z) = 7.583\cdot10^{-22} e^{0.283\phi} \tag{9}$$

where ϕ is the porosity (in %), z is the depth in meters and k is the permeability in m^2. The anisotropic permeability ratio (i.e. k_H/k_v) equals to 5.

Since the permeability magnitude has significant influence on the resulting pore pressure distribution [23, 25], 2 model scenarios with either the competent layers being permeable or the incompetent layers being permeable are considered (Tables 1,2). The models are subjected to 2 or 3 different load steps respectively (Table 3). The first load step features the equilibration of the gravitational compaction (termed pre-stressing) of the model [23-25]; in the second load step the model is compressed with a strain rate of 10^{-14} s^{-1} [34] until 50% of bulk shortening is obtained; the third load step applies uni-axial erosional unloading (Figure 2b) with an exhumation rate of 1 mm/a [34]. The overburden thickness for the various models is varied considering the different load steps (Table 3). For models featuring the buckling process only (Models 1 & 2; Table 3) an overburden thickness of 1000 m is chosen. Models also subjected to erosional unloading (Models 3 & 4; Table 3) have an overburden 3000 m thick. For the erosional unloading models different deformation stages (i.e. different amounts of bulk shortening) are considered before the onset of exhumation.

The initial pore pressure distribution during the gravitational compaction is hydrostatic. The fluid flow boundary conditions represent a semi-closed system [18] such that fluid flow is constrained across the lateral model boundaries but pressure dissipation occurs vertically.

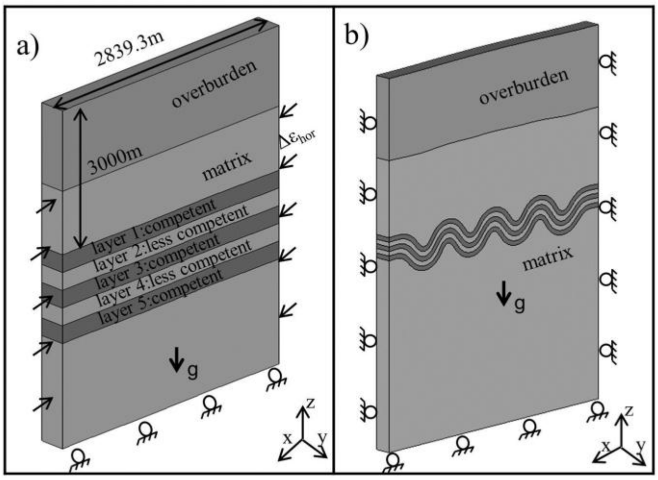

Figure 2: Model geometry and boundary conditions.

Table 1: Material properties for the various models. All model parts feature a Poisson's ratio of ν=0.25.

	E (GPa)		μ (10^{21} Pa·s)	
	Model 1&2	**Model 3&4**	**Model 1&2**	**Model 3&4**
Overburden	2.85(0.5km)	3.03(1.5km)	0.0133	0.0133
Layer 1	29.9	31.93	1	1
Layer 2	2.99	3.193	0.0133	0.0133
Layer 3	29.9	31.93	1	1
Layer 4	2.99	3.193	0.0133	0.0133
Layer 5	29.9	31.93	1	1
Underburden	3.03(1.5km)	3.23(3.5km)	0.133	0.133

Table 2: Horizontal permeabilties for the various models

	Model 1	Model 2	Model 3	Model 4
Overburden	3.44×10^{-15} (0.5km)	3.44×10^{-15} (0.5km)	1×10^{-14} (1.5km)	1×10^{-14} (1.5km)
Layer 1	1.75×10^{-21}	1.75×10^{-15}	3.20×10^{-21}	3.20×10^{-15}
Layer 2	1.75×10^{-15}	1.75×10^{-21}	3.20×10^{-15}	3.20×10^{-21}
Layer 3	1.75×10^{-21}	1.75×10^{-15}	3.20×10^{-21}	3.20×10^{-15}
Layer 4	1.75×10^{-15}	1.75×10^{-21}	3.20×10^{-15}	3.20×10^{-21}
Layer 5	1.75×10^{-21}	1.75×10^{-15}	3.20×10^{-21}	3.20×10^{-15}
Underburden	1×10^{-15} (1.5km)	1×10^{-15} (1.5km)	2.48×10^{-15} (3.5km)	2.48×10^{-15} (3.5km)

Table 3: Various types of loading and overburden thicknesses for the models considered.

Model	Load steps	Overburden thickness
1-2	Pre-stressing Buckling	1000 m
3-4	Pre-stressing Buckling Erosional unloading	3000 m

III. Model Results

In order to assess the critical sustainable pore pressure after Eq. (3) and (4) we assume a value of 30° for the angle of internal friction. The results for ΔP_c are plotted for deformation stages of 10, 20, and 30% of bulk shortening. Larger bulk shortening leads to fold structures with high fold limb dips which are more unlikely to be considered. For the following results analysis the contours of ΔP_c magnitudes at the various deformation stages are presented in combination with the according σ_1 directions. It should be noted that the results description and analysis is focused on the cap rock layers of the respective models considered.

3.1. Model 1

In Model 1 the competent layers (Layers 1, 3, 5) of the multi-layer fold system feature a low permeability and thus represent possible cap rock sequences. While the results for 10% shortening (Fig. 3a) show positive ΔP_c magnitudes of 7.5-9.5 MPa (Layer 4) and 9.5-13 MPa (Layer 2) for the injection layers, the stiffer cap rock layers (Layers 1, 3, 5) show widespread risk of fracture reactivation, i.e. ΔP_c magnitudes of 0 MPa (grey contours in Fig. 3a) throughout large parts of the cap rock layer. The stress orientations display that σ_1 is oriented layer parallel / sub-parallel in Layer 1 and 3. In Layer 5, σ_1 becomes vertical at the top of the fold hinge.

While widespread failure and low ΔP_c magnitudes are still observed at 20% of shortening for the lowest cap rock layer (Figure 3b), the immediate risk of fracture reactivation reduces significantly in the central cap rock layer (Layer 3). Although ΔP_c magnitudes are 0 in a small stretch at the top and the bottom of the hinge zone (Fig. 3b), the centre of this layer has ΔP_c magnitudes of 6.5-10 MPa. ΔP_c magnitudes in the limb are slightly larger (7-11MPa). The top cap rock layer features even higher ΔP_c magnitudes ranging from 8 MPa at the bottom of the hinge to 16.5 MPa towards the top of the hinge (Fig. 3b) and in the limb. ΔP_c magnitudes of 0 MPa are only observed in the synform part of the fold. The σ_1 orientations in the folded layers, which are characterized by higher amplitudes at 20%, show a more pronounced separation from layer parallel / sub-parallel at the bottom of the hinge to σ_1 becoming vertical at the top of the fold hinge, which represents common stress orientations in buckle folds [23,25].

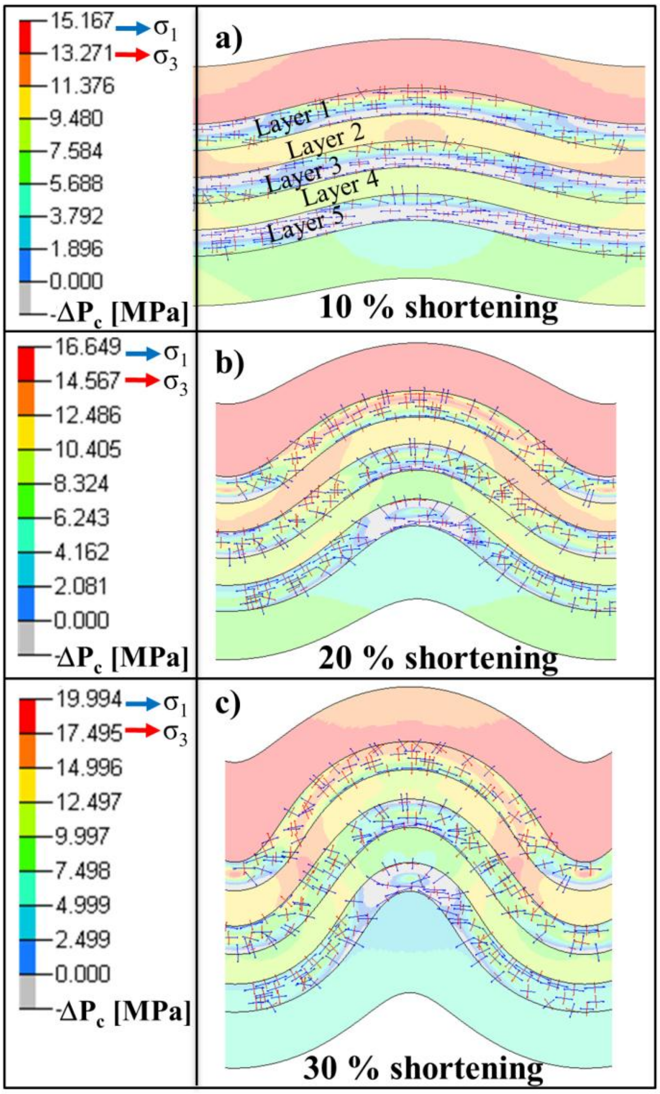

Figure 3: ΔP_c magnitudes and principal stress orientations for Model 1 for 10%, 20% and 30% of bulk shortening.

At 30% of shortening (Fig. 3c) the same pattern of ΔP_c magnitudes can be observed as for 20% of shortening, yet with slightly increased ΔP_c magnitudes. The lowest cap rock features immediate risk of fracture reactivation (ΔP_c ranging from 0-5MPa). For the central cap rock layer ΔP_c magnitudes range from 0MPa at the very top and bottom of the hinge zone to ~12.5MPa in the centre of the hinge zone and 10-12 MPa throughout the fold limb. The top cap rock layer features the highest ΔP_c magnitudes ranging from 8-17.5 MPa. The stress orientations are similar to 20%.

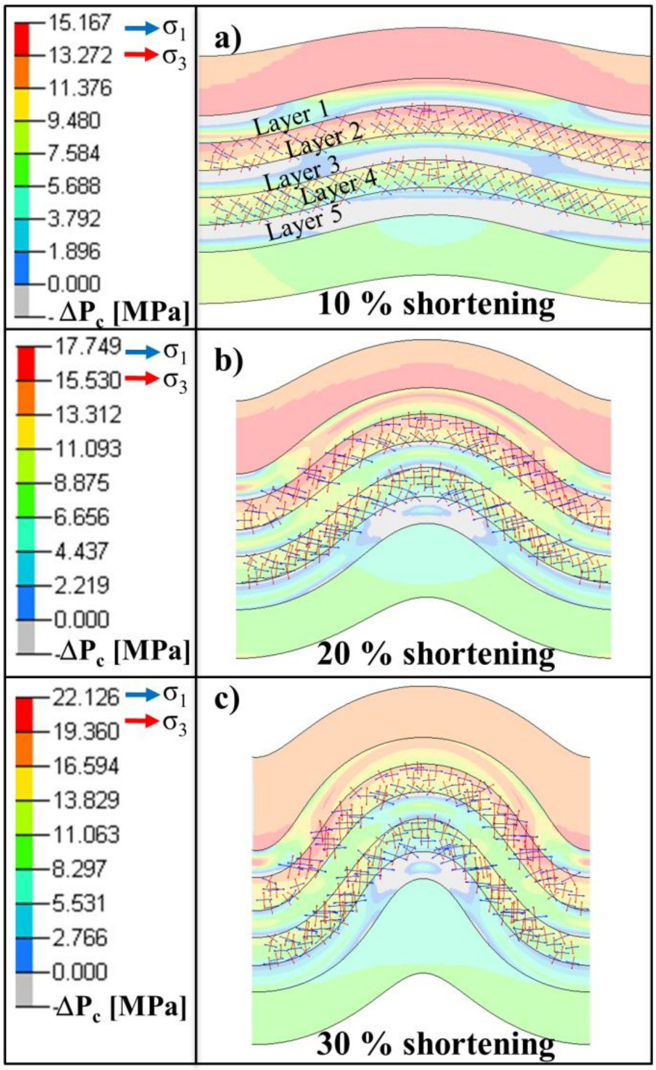

Figure 4: ΔP_c magnitudes for Model 2 for 10%, 20% and 30% of bulk shortening.

3.2. Model 2

In contrast to Model 1, in Model 2 the incompetent layers of the multi-layer fold system feature a low permeability, and hence only Layer 3 and 5 can be considered as injection layers.

The results for 10% shortening (Fig. 4a) show that both cap rock layers feature positive ΔP_c magnitudes while the injection layers show risk of fracture reactivation (i.e. ΔP_c =0). For Layer 2, ΔP_c magnitudes range from 9.5 MPa at the bottom of the layer to 15 MPa at the top of the layer. For Layer 4, ΔP_c magnitudes are lower, ranging from 5.5 MPa at the bottom of the layer to 9 MPa at the top of the layer. The σ_1 orientations do not resemble common patterns as observed for Model 1; σ_1 is orientated oblique (at an angle of ~ ± 45°) throughout both Layers 2 and 4.

For 20% (Fig. 4b) and 30% (Fig. 4c) of shortening the ΔP_c magnitudes generally increase throughout the cap rock layers. In Layer 2, ΔP_c increases to 11-17.5 MPa (at 20%) and 13-19 MPa (at 30%). For Layer 4, ΔP_c has magnitudes of 6-11MPa at 20% and 5-14 MPa at 30%. The σ_1 orientations at 20% and 30% maintain the oblique angle at the bottom of the hinge zone and at the bottom of the limb, but rotate towards σ_1 being horizontal at the top of the hinge. This is in contrast to the commonly expected stress orientations at the top of fold hinges [23,25].

3.3. Model 3

The stiffness and permeability distribution in Model 3 is equivalent to Model 1, although Model 3 features an initial overburden thickness of 3000 m and as a result of the increased compression ΔP_c magnitudes are much higher.

After 10% of shortening (Fig. 5a) the top cap rock layer (Layer 1) displays ΔP_c magnitudes of 30-45 MPa throughout the layer. The second cap rock layer (Layer 3) shows ΔP_c ranging from 17-30 MPa. The lowest cap rock layer (Layer 5) features the lowest ΔP_c magnitudes with imminent risk of fracture reactivation (i.e. $\Delta P_c = 0$) at the bottom of the hinge zone. In the fold limb and towards the top of the hinge zone ΔP_c magnitudes increase to 10-17 MPa.

For 20% of shortening (Fig. 5b) and 30% of shortening (Fig. 5c) a similar distribution of ΔP_c magnitudes is observed for the various layers, featuring increased numbers to the increasing overburden thickness. For Layer 1 ΔP_c ranges between 40-47 MPa (20%) and 47-56 MPa (30%); for Layer 3 ΔP_c ranges between 27-34 MPa (20%) and 32-39 MPa (30%); Layer 5 featuring the lowest ΔP_c magnitudes with ΔP_c reaching 0 MPa at the top of the hinge zone (both at 20% and 30%) and ranging from 6-20 MPa (20%) and 7-23 MPa (30%) throughout the fold.

The stress orientations throughout the shortening stages of the model are similar to Model 1.

In order to investigate the influence of erosional unloading and exhumation processes Fig. 6 shows ΔP_c magnitudes after erosional unloading is applied to the model after the various shortening stages.

For 10% of shortening followed by erosional unloading over 2.06 Ma (with a remaining overburden thickness of 1071 m) it is observed that the top cap rock layer (Layer 1) is prone to fracture reactivation throughout the layer (Fig. 6a). For Layer 3 fracture reactivation occurs at the bottom of the hinge zone and ΔP_c magnitudes range between 0 -12 MPa at the top of the hinge zone and 3-10 MPa in the fold limb. For the lowest cap rock layer (Layer 5) ΔP_c magnitudes range from 1 MPa at the bottom of the hinge to 21 MPa at the top of the hinge zone; ΔP_c magnitudes in the fold limb are ~15 MPa. The stress orientations do not significantly change compared to the shortening stage.

The same behavior for the ΔP_c magnitudes can be observed for 20% (Fig. 6b) and 30% (Fig. 6c) of shortening followed by erosional unloading over 2.37 Ma and 2.039 Ma, respectively (with a remaining overburden thickness of 1349 m and 2253 m, respectively): i.e. overall lower ΔP_c magnitudes; widespread risk of fracture reactivation in Layer 1; localized fracture reactivation at the bottom of the hinge in Layer 3 and only minor risk of fracture reactivation in Layer 5.

Considering the principal stress orientations, significant differences occur after erosion following 20% of shortening: in Layer 1 σ_1 becomes fold parallel (i.e. the out-of plane component in Fig. 6) in the limb and at the top of the hinge zone; in the bottom of the hinge zone σ_1 is horizontal / layer parallel; in Layer 3 σ_1 is mostly horizontal / layer parallel in the hinge zone and parallel to the hinge line in the fold limb; in Layer 5 σ_1 is layer perpendicular in the limb, horizontal at the bottom of the hinge and vertical at the top of the hinge.

For 30% followed by erosion σ_1 orientation in Layer 1 is similar to 20%; in Layer 3 σ_1 is horizontal at the fold hinge and layer perpendicular in the fold limb; in Layer 5 σ_1 is horizontal at the fold hinge but does not show a consistent orientation in the fold limb.

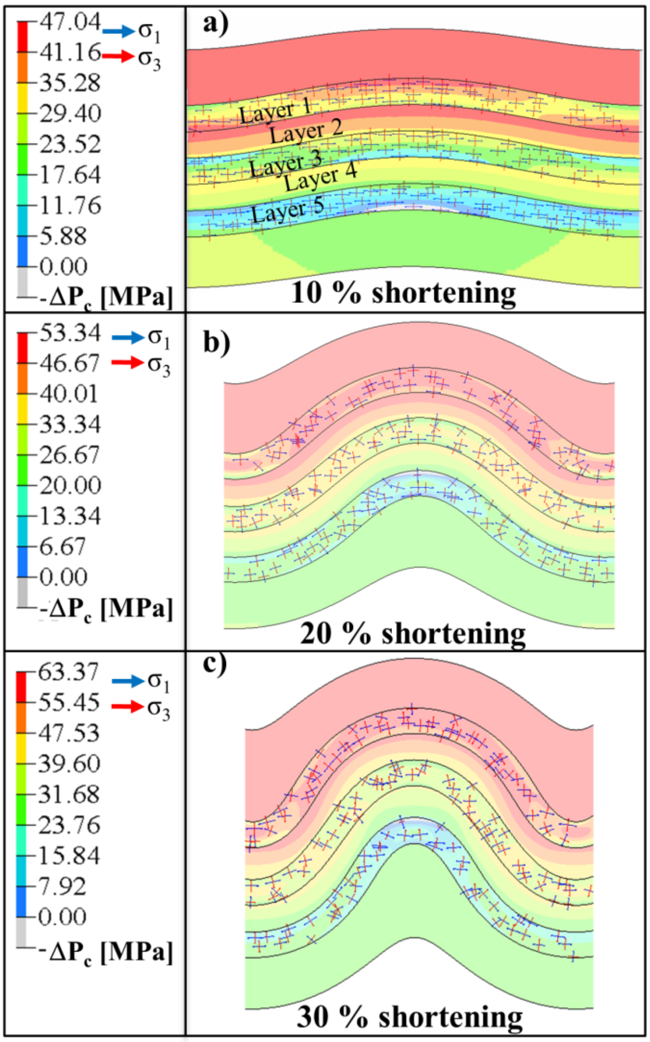

Figure 5: ΔP_c magnitudes for Model 3 for 10%, 20% and 30% of bulk shortening.

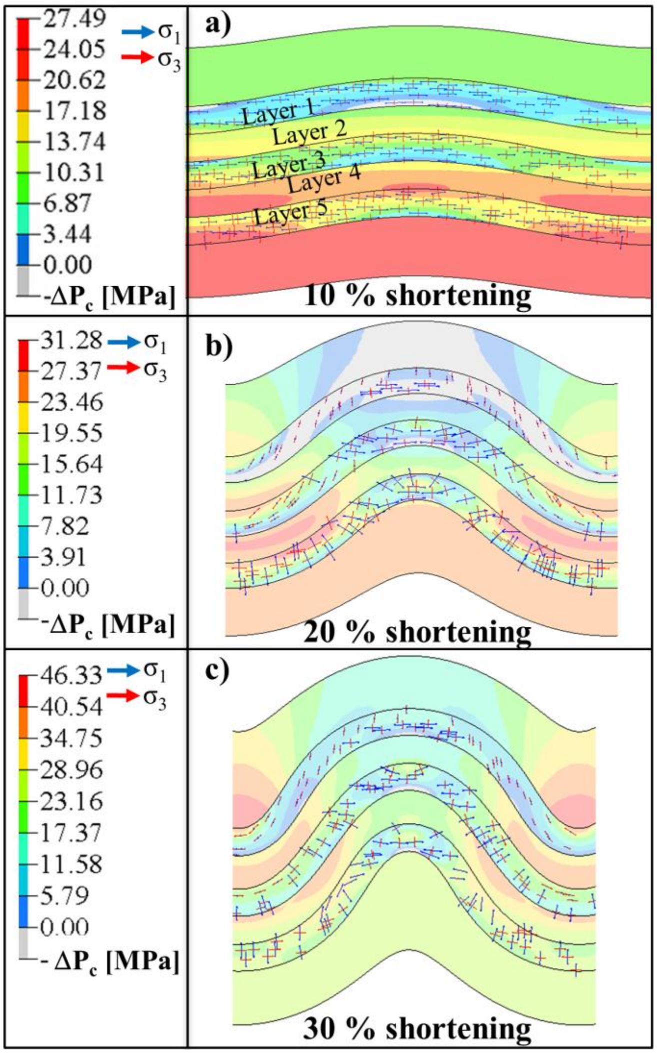

Figure 6: ΔP_c magnitudes for Model 3 after erosional unloading is applied.

The significant decrease in ΔP_c magnitudes due to erosional unloading can be explained by considering the evolution of the principal effective stresses at the top and bottom of the fold hinge of Layer 1. Figure 7a,b (showing this exemplarily for the 10% shortening model) shows that the minimum effective principal stress, σ'_3, decreases much more rapidly than the maximum effective principal stress, σ'_1, hence increasing the differential stress and reducing the ΔP_c magnitudes throughout the erosional unloading process.

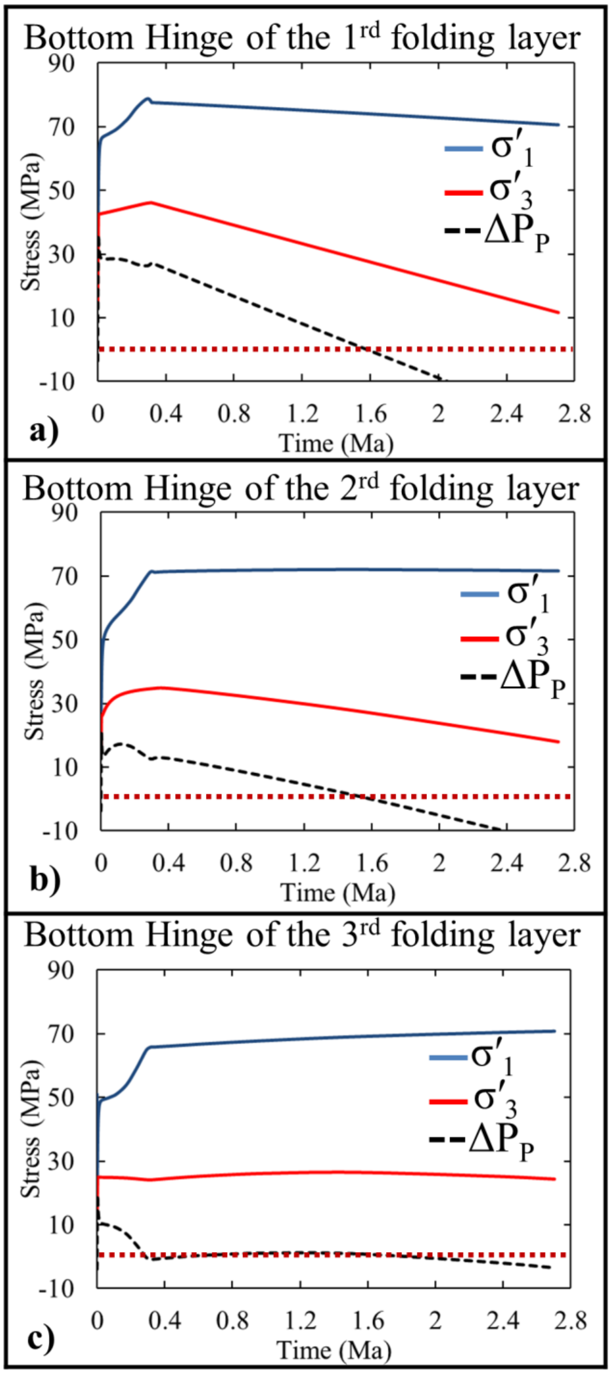

Figure 7: Effective principal stress evolution for Model 3 during erosional unloading.

3.4. Model 4

The stiffness and permeability distribution in Model 4 is equivalent to Model 2, although Model 4 features an initial overburden thickness of 3000 m and as a result of the increased compression ΔP_c magnitudes are much higher.

The top cap rock layer (Layer 2) displays ΔP_c magnitudes of ~41 MPa throughout the layer for 10% of shortening (Fig. 8a), 33-47 MPa for 20% of shortening (Fig. 8b), and 39-55 MPa for 30% of shortening (Fig. 8c). The second cap rock layer (Layer 4) shows slightly lower ΔP_c ranging from 25-31 MPa at 10% shortening, 27-33.5 MPa at 20%, and 23-31 MPa at 30%. The stress orientations throughout the shortening stages of the model are similar to Model 2.

In contrast to Model 3, the top cap rock layer (Layer 2) does not show imminent risk of fracture reactivation after 10% of shortening followed by erosional unloading over 2.06 Ma (with a remaining overburden thickness of 1071 m; Fig. 9a). ΔP_c magnitudes are ~13-17 MPa at the bottom of the hinge zone and ~7-10 MPa at the top of the hinge zone. The second cap rock layer has even higher ΔP_c magnitudes ranging from ~15 MP at the top of the hinge to 20-24 MPa at the bottom of the hinge. σ_1 is oriented horizontal in Layer 2 and at the top of the fold hinge in Layer 4.

For 20% followed by 2.3 Ma of erosion (with a remaining overburden thickness of 1292 m; Fig. 9b) ΔP_c magnitude contours are not layer sub-parallel anymore. For Layer 2, the lowest ΔP_c magnitudes are observed at the fold hinge zone with ΔP_c = 4-8 MPa at the bottom of the hinge and ΔP_c = 0 MPa at the top of the hinge. ΔP_c magnitudes in the fold limb increase towards ~17 MPa. For Layer 4, ΔP_c magnitudes are slightly higher ranging from ~13 MPa at the bottom of the hinge to ~9 MPa at the top of the hinge and increasing towards ~22 MPa in the fold limb.

The σ_1 orientations in Layer 2 are horizontal for the fold limb and the fold hinge zone; in the synform of the fold σ_1 becomes parallel to the hinge line. In Layer 4, σ_1 orientations are horizontal in the fold hinge and at an angle of ~45° to bedding in the fold limb.

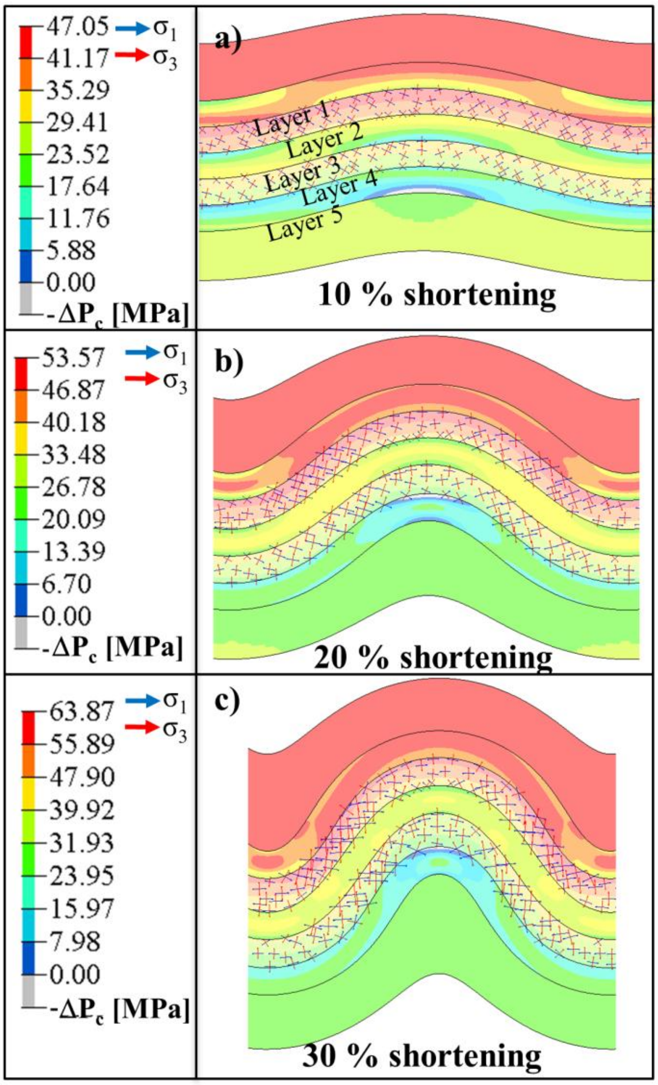

Figure 8: ΔP_c magnitudes for Model 4 for 10%, 20% and 30% of bulk shortening.

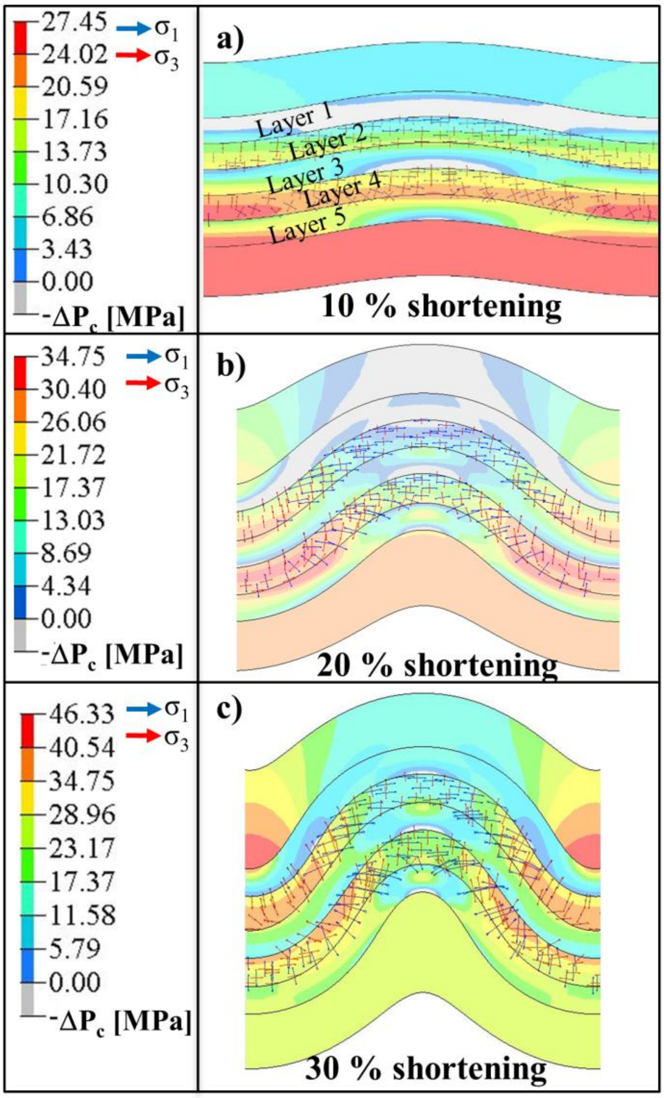

Figure 9: ΔP_c magnitudes for Model 4 after erosional unloading is applied.

For 30% followed by 2.039Ma of erosion (with a remaining overburden thickness of 2253 m; Fig. 9c) yields ΔP_c magnitudes in Layer 2 of 11-17 MPa in the hinge zone and 23-35 MPa in the fold limb. Layer 4 features ΔP_c magnitudes of 17-23 MPa in the hinge zone and 23-40 MPa in the limb. The stress orientations in both Layer 2 and 4 are similar to the 20% stage followed by erosion.

IV. Discussion

Recently, [20] have applied the PPSC concept to calculate ΔP_c of generic anticline structures under different stress regimes and considering different levels of inter-layer coupling using 3D finite element analysis. Their results show that ΔP_c results are strongly dependent on the relative location with respect to the injection location and are different for each combination of model parameters (such as stress regime and inter bedding friction coefficient). They conclude that in general the largest values of ΔP_c are obtained for a compressional stress regime and the lowest values of ΔP_c are obtained for an extensional stress regime, being in agreement with an earlier study by [10].

It should be recalled that the anticline models considered in [20] are based on static representations of stress and pore pressure, i.e. the specific strain path of how the geologic system evolved is not considered. As a result the ΔP_c magnitudes in [20] show much smaller variability. Based on recent studies by [23-25], which show that principal stress and pore pressure magnitudes vary significantly throughout the deformation history of the fold and with respect to the permeability distribution of the modeled layers, the results of this study show and confirm that the evolution of ΔP_c also varies significantly.

4.1. Competent cap rock

For a scenario featuring stiff and more competent cap rock layers (Model 1), the early stages of deformation (10% of shortening) are characterized by a widespread risk of fracture reactivation (i.e. $\Delta P_c = 0$) at the bottom of the hinge zone throughout all cap rock layers (Layers 1, 3, 5; Fig. 3). As deformation progresses ΔP_c magnitudes in Layer 1 and 3 become significantly larger until at 30% shortening (ΔP_c = ~17.5 MPa in Layer 1; Fig. 3a), widespread failure is only observed for Layer 5 (Fig. 3b,c). In order to properly address the fracture reactivation risk the corresponding stress orientations of σ_1 and σ_3 have to be considered. For the regions characterized by $\Delta P_c = 0$ in the bottom of the cap rock hinge, σ_1 is horizontal and σ_3 is vertical at all deformation stages (Fig. 3). This corresponds to low angle thrust faults being optimally oriented for reactivation. For 30% of shortening at the top of the hinge in Layer 5, σ_1 is vertical and σ_3 is horizontal, making either high angle extensional faults or vertical extensional joints prone to reactivation. As stated by [35] fold hinge zones are characterized by low angle thrust faults at the bottom of the hinge and high angle extensional faults near the top of the hinge zone, hence making these regions an imminent risk of fracture reactivation.

The same layer configuration featuring a larger overburden thickness (Model 3) is characterized by much larger ΔP_c magnitudes due to the larger amount of compression and the risk of fracture reactivation is not imminent in any cap rock layer.

However, the results for Model 3 show that after the onset of erosional unloading, σ'_3 magnitudes drastically decrease, i.e. the differential stress increases, and hence ΔP_c magnitudes decrease rapidly, resulting in possible cap rock failure in Layers 1 and 3 for 10% and 20% of shortening followed by erosion. Erosional unloading has a larger effect (i.e. resulting in lower ΔP_c) for folds subjected to lower bulk shortening and the decrease in ΔP_c is largest for Layer 1 and lowest for Layer 5 (Fig. 6). This can be explained by the remnant strain stored in the respective fold layer [23]. Layer 5 features a narrower fold hinge and hence experiences more compression, which results in a slower decrease of ΔP_c (Fig. 7c).

The σ_1 orientations in the cap rock regions characterized by $\Delta P_c = 0$ at 10% followed by erosion are horizontal at the bottom of the hinge in Layer 1, corresponding to an imminent risk of fracture reactivation of low angle thrust fault likely to occur here [35]. The same fracture reactivation risk is evident at the bottom of the hinge zone in Layers 1 and 3 for the 20% and 30% stages followed by erosion. ΔP_c magnitudes of 0 are also observed in Layer 1 for 20% of shortening followed by erosion. The corresponding hinge line parallel σ_1 orientation and σ_3 being layer perpendicular would indicate reactivation of low angle thrust faults striking perpendicular to the hinge line. Such faults are not characteristic for buckle folds and have not been documented in the relevant literature [35]. More likely than the reactivation of these shear fractures is the onset/initiation of layer perpendicular tensile fractures when σ'_3 reaches 0 MPa for the case of prolonged erosion (Fig. 10). These tensile fractures are documented to occur frequently in buckle folds [35] and are likely to be initiated in buckle folds subjected to erosion [23].

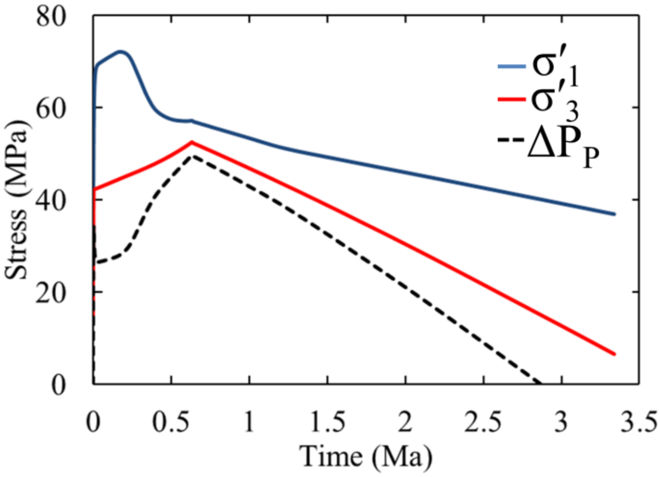

Figure 10: Effective principal stress evolution for Model 4 during erosional unloading in the limb of Layer 1.

4.2. Incompetent cap rock

In contrast to Model 1, Model 2 features cap rock layers that are less stiff and less competent. The results of Model 2 show that the cap rock layers are not at risk for fracture reactivation throughout the bulk shortening phase of deformation (Fig. 4). For all shortening stages the top cap rock layer (Layer 2) features the highest ΔP_c magnitudes. The stress orientations in Model 2 are not consistent with the orientations observed in Model 1 (which favor reactivation of frequently observed fracture sets) and thus provide an additional degree of safety as shear fractures oriented for reactivation due to the orientations in Model 2 (e.g. low angle thrust faults at the top of the hinge zone) are not likely to be observed in buckle folds [35].

It should also be noted that the possible injection layers (Layer 3 and 5) are characterized by fracture reactivation throughout the deformation history, which in turn has to be considered positive as the injectivity is increased in a fractured reservoir.

Similar to Model 3, the same layer configuration featuring a larger overburden thickness (Model 4) is characterized by much larger ΔP_c magnitudes (e.g. ΔP_c reaching up to 55MPa for 30%; Fig. 8c) due to the larger amount of compression and the risk of fracture reactivation is further reduced in both cap rock layers. Once erosional unloading is considered, ΔP_c

magnitudes are reduced but $\Delta P_c = 0$ is only obtained for 20% followed by erosion at the top of the hinge for Layer 2. The corresponding horizontal orientation of σ_1 would again favor low angle thrust faults at the top of the hinge, which are unlikely to occur here.

4.3. Summary and comparisons

The results concerning the risk of fracture reactivation presented in this study show great variability in ΔP_c magnitudes depending both on the time in the deformation history of the fold as well as on the distribution of material properties. The combination of permeability distribution with the competence contrast in the respective cap rock – reservoir layer sequences is important. In general, low permeability in less competent layers (i.e. Model 2) results in greater ΔP_c magnitudes, with ΔP_c increasing for an increased amount of shortening. Risk of fault reactivation is not evident throughout the shortening process (i.e. $\Delta P_c > 0$) for all cap rock layers of the multi-layer fold system. For scenarios featuring low permeability in a competent layer (i.e. Model 1) cap rock failure is likely at the early stages of deformation for all cap rock layers, and only for later stages $\Delta P_c > 0$ in Layer 1 and 3; Layer 5 is always at risk of fracture reactivation. The differences between Model 1 and Model 2 can be explained by the lower differential stress resulting in the less competent layers, thus resulting in higher ΔP_c magnitudes. These results agree with [20] who also observe that if the cap rock is stiffer than the injection layer, ΔP_c may become 0 at the bottom of the hinge zone.

This study also shows that the process of erosional unloading needs to be considered for evaluating the risk of fracture reactivation of a geologic structure. Due to the decrease of σ'_3 the differential stress generally increases during erosion and as a result ΔP_c magnitudes decrease. This phenomenon again is more pronounced for scenarios featuring stiffer, more competent cap rock layers than injection/reservoir layers. E.g. once erosional unloading is considered for Model 4, ΔP_c magnitudes are reduced, but not as significantly as for Model 3. For example, ΔP_c magnitudes after 10% shortening followed by erosion are 7-17MPa in Layer 2 and 15-24 MPa in Layer 4. For the same stage of shortening + erosion, Model 3 shows ΔP_c magnitudes ranging from 0-7 MPa in Layer 1, 3.5-13 MPa in Layer 3, and 7-17 MPa in Layer 5. Furthermore, erosional unloading results in lower ΔP_c magnitudes in folded layers at the top of the multi-layer sequence. The lower layers are characterized by a higher degree of remnant compressional strain and thus the decrease in σ'_3 is less rapid [23].

In order to better visualize the effect of erosional unloading, 2 fold systems featuring less stiff cap rock layers are presented in Fig. 11. The multi-layer fold systems feature the same final overburden thickness (i.e. 1180 m), yet Model 5 (Fig. 11a) represents a fold that is under active shortening (20%), while Model 6 (Fig. 11b) represents a fold that had an initial overburden thickness of 3000 m and was subjected to erosional unloading. The difference in ΔP_c magnitudes is evident. Layer 2 in Model 5 has ΔP_c ranging from 11-17MPa (Fig. 11a); Layer 2 in Model 6 has ΔP_c ranging from 0MPa at the bottom of the hinge zone to 4-12 MPa at the top of the hinge and in the limb (Fig. 11b); Layer 4 in Model 5 has ΔP_c ranging from 4.5-11 MPa (Fig. 11a); Layer 4 in Model 6 has ΔP_c ranging from ~15 MPa at the bottom of the hinge to ~8MPa at the top of the hinge and 12-27 MPa in the limb (Fig. 11b). These differences while significantly affected by the decrease in σ'_3 as observed in Fig. 7, can be better understood by the evolution of the pore pressure in the fold system. The pore pressure distribution during the shortening stage (Fig. 11a) indicates hydrostatic values for the overburden and Layer 1, followed by over-pressure generated in the low permeability layers. As a result the pore pressure contours become layer parallel in the fold system. During the erosional unloading stage the over-pressure is significantly reduced, at a much higher rate as the hysdrostatic pore pressure in the overburden (Fig. 11b). The resulting under-pressure is in agreement with observations by [36,37] showing under-pressure evolution in 1D consolidation studies followed by elastic erosional unloading.

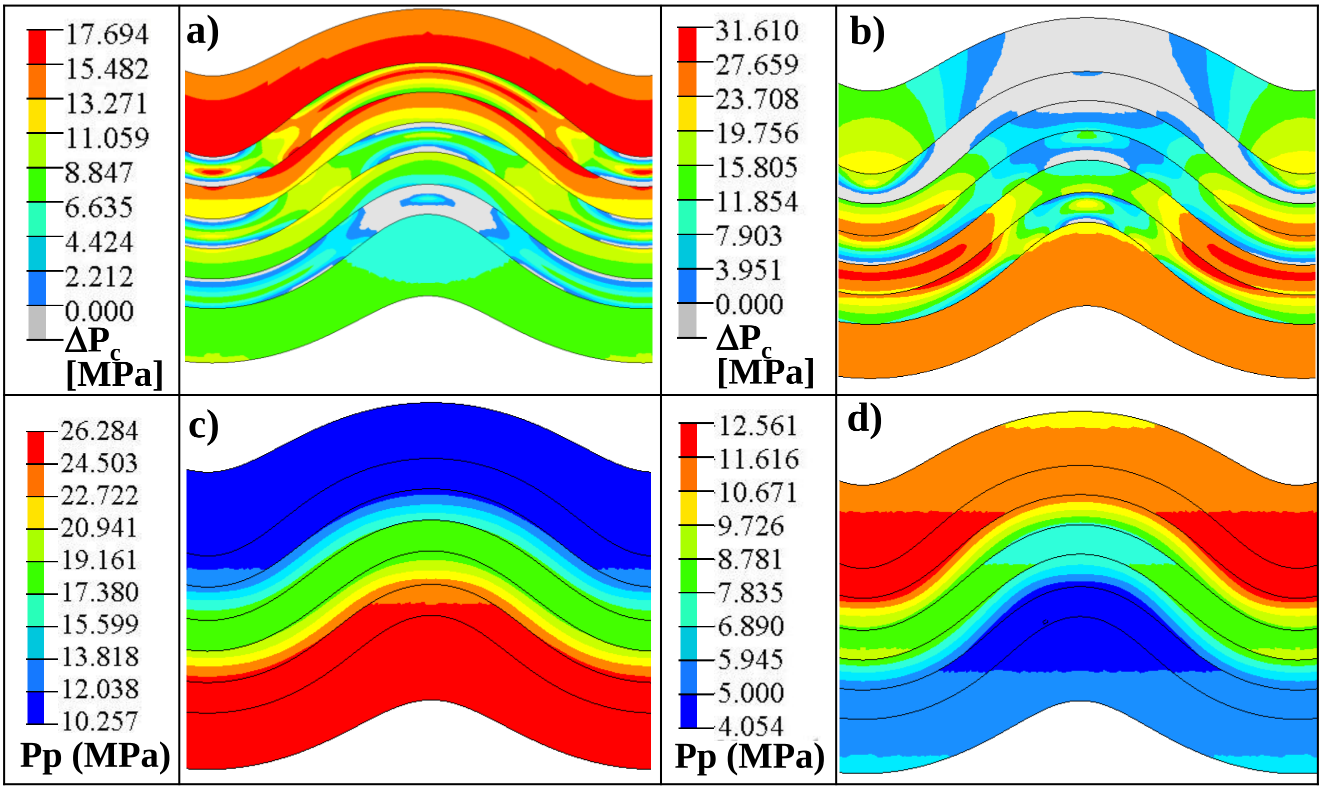

Figure 11: a) ΔP_c magnitudes for Model 5 featuring 20% of shortening with a remaining overburden of 1180 m. Grey contours represent zero critical pore pressure indicating failure. b) ΔP_c magnitudes for Model 6 featuring 20% of shortening with a remaining overburden of 1174 m after erosion. c) Pore pressure magnitudes for Model 5. d) Pore pressure magnitudes for Model 6.

IV. Conclusions

The concept of PPSC is extremely helpful as a first order risk assessment tool prior to subsurface fluid injection applications when the state of stress can be determined using numerical modeling approaches such as FEA. Based on the resulting 3D stress tensor, Eqs. (3 & 4) can be used to calculate the maximum sustainable pore pressure change, ΔP_c, in a formation before optimally oriented fractures are at risk of reactivation. The full 3D tensor based concept of PPSC is especially important for geologic structures which are characterized by a state of stress which is not Andersonian, i.e. where the vertical stress is not a principal stress (such as fold structures).

The results of this study show that the minimum ΔPc is varying throughout the deformation history of multilayer buckle folds and different locations within the structure show great variability in ΔP_c. Furthermore, the permeability distribution of the various layers in the multilayer fold system has great influence on minimum ΔP_c. If similar multi-layer buckle fold scenarios as presented in this study are considered for fluid injection applications the following points should be considered:

- Less competent (i.e. lower viscosity and Young's modulus) cap rocks should be preferred as larger ΔP_c magnitudes result.
- Injection in deeper settings (increased overburden thickness) provides larger ΔP_c magnitudes.
- If cap rocks represent stiff units, fold structures at a later stage of deformation should be preferred.
- Risk assessment of geologic structures needs to consider the deformation history of the structure, i.e. is erosional unloading present.
- Stress and pore pressure measurements are considered absolutely vital to calibrate site specific numerical models in order to benchmark the stress and strain history for realistic estimates of ΔP_c magnitudes.

It is clear that the numerical models presented are based on some limiting assumptions. As an outlook for future studies, the thermal evolution, especially during the erosional unloading process, needs to be considered as thermal contraction during exhumation will decelerate the evolution of under-pressure. The onset and initiation of fractures during the folding process can be added in the calculation of ΔP_c by including the rock cohesion into the equation system. Furthermore, fold structures in nature rarely resemble perfectly shaped cylindrical folds – the 3D state of stress in dome structures such as periclines will be different.

References

[1] R.H. Sibson. "Brittle failure controls on maximum sustainable over-pressure in different tectonic stress regimes", *Bulletin American Society of Petroleum Geology*, v.87, p. 901-908, 2003.

[2] C.A. Barton, M.D. Zoback, and D.Moss. "Fluid flow along potentially active faults in crystalline rock", *Geology*, 23 (8), pp. 683-686, 1995.

[3] J.F. Gibbs, J.H. Healy, C.B. Raleigh, and J. Coakley. "Seismicity in the Rangely, Colorado, area: 1962–1970", *Bulletin Seismological Society of America*, 63, p. 1557–1570. 1973.

[4] R.L. Wesson, and C. Nicholson. "Earthquake Hazard Associated with Deep Well Injection", *Prepared by the U.S. Geological Survey*. Open-File Report 87-331, 1987.

[5] C. Frohlich, E. Potter, C. Hayward, and B. Stump. "Dallas-Fort Worth earthquakes coincident with activity associated with natural gas production", *The Leading Edge*, 29(3): p. 270-275, 2010.

[6] F. Cappa, and J. Rutqvist. "Impact of CO2 geological sequestration on the nucleation of earthquakes", *Geophysical Research Letters*, 38, L17313, 2011.

[7] J.P. Verdon, J.-M. Kendall, D.J. White, and D.A. Angus. "Linking microseismic event observations with geomechanical models to minimize the risks of storing CO2 in geological formations", *Earth Planet. Sci. Lett.*, 305, 1–2, p. 143–152, 2011.

[8] J.E. Streit, R.R. Hillis. "Estimating fault stability and sustainable fluid pressures for underground storage of CO2 in porous rock", Energy, 29, p. 1445-1456, 2004

[9] Q. Li, Z. Wu, Y. Bai, X. Yin, and X. Li. "Thermo-hydro-mechanical Modeling of CO2 Sequestration System Around Fault Environment", *Pure Appl. Geophys.*, 163, p. 2585-2593, 2006.

[10] J. Rutqvist, J. Birkholzer, F. Cappa, and C.-F. Tsang. "Estimating maximum sustainable injection pressure during geologic sequestration of CO2 using coupled fluid flow and geomechanical fault-slip analysis", *Energy Conversion and Management*, p. 1798-1807, 2007.

[11] J. Rutqvist, J. Birkholzer, F. Cappa, and C.-F. Tsang. "Coupled reservoir-geomechanical analysis of the potential for tensile and shear failure associated with CO2 injection in multilayered reservoir-caprock systems." *Int J Rock Mech Min Sci*, 45, p. 132-143, 2008.

[12] S. Vidal-Gilbert, J.-F. Nauroy, and E. Brosse. "3D geomechanical modeling for CO2 geologic storage in the Dogger carbonates of the Paris Basin", *Int. J. Greenhouse Gas Control*, V.3, Issue 3, p. 288-299, 2008.

[13] M.D. Zoback. "Managing the seismic risk posed by wastewater disposal", *Earth Magazine*, April 2, p. 38-43, 2012.

[14] A. Settari, and F.M. Mourits. "A Coupled Reservoir and Geomechanical Simulation System", SPE Journal, 3, p. 219–226, 1998.

[15] S.E. Minkoff, C.M. Stone, S. Bryant, M. Peszynska, and M.F. Wheeler. "Coupled fluid flow and geomechanical deformation modeling", *Journal of Petroleum Science and Engineering*, 38, p. 37–56, 2003.

[16] R. Dean, X. Gai, C. Stone, and S. Minkoff. "A Comparison of Techniques for Coupling Porous Flow and Geomechanics", SPE Journal, 11, p. 132–140, 2006.

[17] F. Cappa. "Influence of hydromechanical heterogeneities of fault zones on earthquake ruptures", *Geophys. J. Int.*, 185, p. 1049-1058, 2010.

[18] Q. Zhou, J.T. Birkholzer, C.-F. Tsang, and J. Rutqvist. "A method for quick assessment of CO2 storage capacity in closed and semi-closed saline formations", *International Journal of Greenhouse Gas Control*, 2, p. 626–639, 2008.

[19] A. Amirlatifi, A. Eckert, R. Nygaard, B. Bai, X. Liu, and M. Paradeis. "Role of Geometrical Influences of CO2 Sequestration in Anticlines", *46th US Rock Mechanics / Geomechanics American Rock Mechanics Assosiaction Symposium*. Chicago, IL, p. 12–255, 2012.

[20] A. Eckert, W. Zhang, X. Liu, and M. Paradeis, "Numerical estimates of the maximum sustainable pore pressure in anticline formations using the tensor based concept of pore pressure-stress coupling", *Journal of Rock Mechanics and Geotechnical Engineering*, V.7, 1, pp. 60-72, 2015.

[21] J.B. Altmann, T.M. Müller, B. Müller, M.R.P. Tingay, and O. Heidbach. "Poroelastic contribution to the reservoir stress path", *International Journal of Rock Mechanics and Mining Science*, 47, p. 1104–1113, 2010.

[22] J.B. Altmann, B. Müller, T.M. Müller, O. Heidbach, M.R.P Tingay, and A. Weißhardt. "Pore pressure stress coupling in 3D and consequences for reservoir stress states and fault reactivation", *Geothermics*, 52, p. 195-205, 2014.

[23] A. Eckert, P. Connolly, and X. Liu. "Large-scale mechanical buckle fold development and the initiation of tensile fractures", *Geochem. Geophys. Geosyst.*, 15, 11, p. 4570-4587, 2014.

[24] A. Eckert, X. Liu, and P. Connolly. "Pore Pressure Evolution and Fluid Flow during Visco-elastic Single-Layer Buckle Folding. *Geofluids*, in press, 2015.

[25] X. Liu, A. Eckert, and P. Connolly. "A Comparison of Stress Evolution in Single-layer and Multi-layer Buckle Folds. *The 49th US Rock Mechanics / Geomechanics Symposium*, San Francisco, CA, USA, 28 June- 1 July 2015.

[26] T. Engelder. "Loading paths to joint propagation during a tectonic cycle; an example from the Appalachian Plateau, USA", *Journal of Structural Geology*, 7, p. 459-476, 1985.

[27] T. Engelder, and M.P. Fischer. "Influence of poroelastic behavior on the magnitude of minimum horizontal stress, Sh, in overpressured parts of sedimentary basins", *Geology*, 22, p. 949–952, 1994.

[28] R.R. Hillis. "Coupled changes in pore pressure and stress in oil fields and sedimentary basins", *Petroleum Geoscience*, 7, p. 419–425, 2001.

[29] J.W.J. Rudnicki. "Fluid Mass Sources and Point Forces in Linear Elastic Diffusive Solids", *Mechanics of Materials*, 5, p. 383–393, 1986.

[30] J.C. Jaeger, N.G.W. Cook, and R.W. Zimmerman. "*Fundamentals of Rock Mechanics*", 4th Edition. ed. John Wiley & Sons, 2007.

[31] S.M. Schmalholz, and Y.Y. Podladchikov. "Buckling versus folding: importance of viscoelasticity", *Geophysical Research Letters*, 26(17), p. 2641-2644, 1999.

[32] S.M. Schmalholz, Y.Y. Podladchikov, and D.W. Schmid. "A spectral/finite difference method for simulating large deformations of heterogeneous, viscoelastic materials", *Geophysical Journal International*, 145(1), p.199-208, 2001.

[33] C.R. Medina, J.A. Rupp, and D.A. Barnes. "Effects of reduction in porosity and permeability with depth on storage capacity and injectivity in deep saline aquifers: A case study from the Mount Simon Sandstone aquifer", *International Journal of Greenhouse Gas Control*, 5(1), p.146-156, 2011.

[34] R.J. Twiss, And E.M. Moores. "Structural Geology", 2nd Edition, W.H. Freeman and Company, New York, 2007.

[35] N.J. Price, and J.W. Cosgrove. "Analysis of Geological Structures". Cambridge University Press, UK 1990.

[36] J.J. Jiao., and C. Zheng. "Abnormal fluid pressures caused by deposition and erosion of sedimentary basins", *J. Hydrol.*, 204(1), p.124-137, 1998.

[37] S. Ellis, and D. Darby. "A modified Terzaghi consolidation factor for first-order estimation of overpressure resulting from sedimentation: review and synthesis", Math. Geol., 37(1), p.115-123, 2005.

Journal of Energy Challenges and Mechanics

http://www.nscj.co.uk/JECM/

ISSN 2056-9386
Volume 2 (2015) issue 4, article 3

Solar air-conditioning designs for residential buildings in Saudi Arabia

沙特阿拉伯居住建筑的太阳能空调设计

A. A. Al-Ugla*, M. A. I. El-Shaarawi

Mechanical Engineering Department, King Fahd University of Petroleum & Minerals (KFUPM), Dhahran 31261, Saudi Arabia

*ali.ugla@aramco.com

Abstract - **The excessive demand for air conditioning in Saudi Arabia is a direct result of the high ambient temperatures. Air-conditioning systems in residential buildings in Saudi Arabia consume approximately 46% of the total produced electrical energy. Almost air-conditioning systems used in Saudi Arabia are of the conventional (vapor-compression) type, which consumes a large amount of mechanical/electrical energy. Solar energy can be used instead to power such systems and hence help in the reduction of carbon emission, environmental pollution and global warming effects. Out of various renewable sources of energy, solar energy proves to be the best candidate for air conditioning in Saudi Arabia because of the coincidence of the maximum cooling load with the period of the greatest solar radiation input. In this paper, a solar air-conditioning system consisting of solar-powered LiBr-H_2O absorption chiller, flat plate collectors and storage tanks is investigated for a constant cooling load of 5 kW. A solar absorption air-conditioning system for a typical family living house in Saudi Arabia is studied with three storage designs (heat storage, cold storage, and refrigerant storage) to achieve full-day operation (24-hours constant cooling effect). The system performance, cost, features, energy saving and environmental pollution reduction are investigated based on the thermodynamic analysis. The results show the effect of the condenser temperature (which depends on the ambient temperature) and the evaporator temperature (which depends on the cooling load requirements) on the mass storage, energy saving and environmental pollution reduction. Based on the required storage tank capacity, the results indicate that refrigerant storage is the most suitable design for 24-hours supply of the constant cooling effect.**

Keywords - **24-hours, solar-powered, air-conditioning, residential buildings**

I. Introduction

Presently almost all the cooling produced in Saudi Arabia is by means of vapor compression systems. The compressors of these vapor compression systems are directly run by theelectrical energy that is generated by burning fossil fuel.

The building sector consumes nearly 70% of the total electrical energy produced in Saudi Arabia [1]. The air-conditioning systems in those building consume approximately 65% of the electrical energy of the building sector [2], thus, air-conditioning systems in the building sector in Saudi Arabia consume approximately 46% of the total produced electrical energy. Therefore, it is critical to consider the utilization of innovative solutions such as solar cooling.

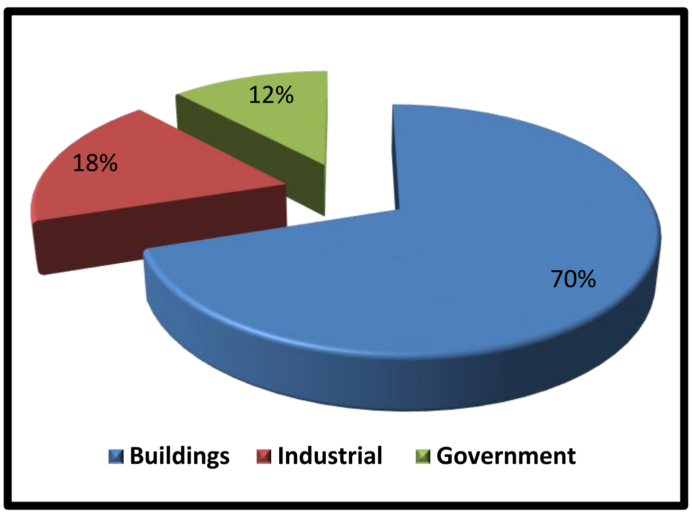

Fig. 1, Saudi Arabia Electrical Power Demand Distribution [1]

Solar energy can be used to power air-conditioning systems in two ways. First way is that, solar energy can be converted into electricity using Photo-Voltaic Cells and used to operate a conventional vapor-compression refrigeration system. Second way is that, solar energy can be used to heat the working fluid in the generator of a vapor sorption (absorption or adsorption) system. In the absorption air conditioning system, a heat source drives the cooling process, which can be considered an alternative to conventional air conditioning if excess heat is available, such as heat from the sun, which is applicable in Saudi Arabia.

The main difference between vapor compression (conventional) and absorption system is that absorber, generator and pump replace the compressor. In term of performance, absorption system can be categorized into the following three types:

- Single Effect: COP 0.6 to 0.8
- Double Effect: COP 1.0 to 1.2
- Triple Effect COP 1.4 to 1.6

COP is the coefficient of performance used to measure the performance of cooling systems. Higher COP, larger than one, means higher efficiency of the equipment which equates to lower operating costs. The main benefits of absorption systems are:

- Vibration-free
- Longer life-time
- High reliability
- Low maintenance
- Energy Saving

The major working pairs employed for solar absorption systems are LiBr-H_2O and H_2O-NH_3. Most researches confirm that LiBr-H_2O has a higher COP than for the other working fluids, the low cost and excellent performance of this working fluid combination make it the favorable candidate for use in solar air conditioning cycles. However, it cannot be used in sub-zero cooling application. The ammonia-water system has the following disadvantages when compared to LiBr-H_2O system [3].

- The coefficient of performance (COP) for the H_2O-NH_3 system is lower than that for the LiBr-H_2O system.
- It requires a higher generator inlet temperature, which results in the H_2O-NH_3 cooling systems achieving a lower COP.
- It requires higher pressures and hence higher pumping power.
- A more complex system requiring a rectifier to separate ammonia and water vapor at the generator outlet is required.
- There are restrictions on in-building applications of ammonia-water cooling units because of the hazards associated with the use of ammonia.

For these reasons, the lithium bromide-water system is considered better suited for most solar absorption air-conditioning applications. The storage can be used in an absorption cooling system to increase the effectiveness of the system.

The two main storage systems are (Hot storage tank and Cold storage). These two storage systems can be used individually or in combination. The hot storage is accomplished using a hot water storage tank, in order to reduce losses in conversion of thermal energy. The cold storage can be integrated in order to store energy at times of high radiation for use at times when the available solar energy is not sufficient to meet the cooling demand.

II. ENERGY SAVING

The developed designs systems operate 24-hour a day (continuous operation) using three methods of storage systems (heat, cold and refrigerant). During the full day (24-hour), for a constant hourly cooling load of five kWh for typical house in Saudi Arabia, the only electrical energy used is the pump consumption, which is less than 0.01% of the total energy produced by electricity. Using simulation software, engineering equation solver (EES), Table 1 shows the amount of energy saved using solar air-conditioning with storage systems. It indicates that for one house, 56.3 MWh of electrical energy can be savedon annual basis.

Table 1: Energy Saving

Period	**Energy Saving**
Hourly	6.43 kWh
Daily	154.2 kWh
Annually	56.3 MWh

III. ENVIRONMENTALIMPACT

The environmental effects of carbon dioxide are currently of significant interest. The increase of carbon dioxide emission has major negative impact on the environment. According to the World Bank for 2014, Table 2 shows the carbon dioxide emission in Saudi Arabia and United Kingdom [4, 5]. In both countries, the rate of CO2 emissions is high; however, in Saudi Arabia the rate per capita is higher than UK.

Table 2: CO_2 emissions in Saudi Arabia and United Kingdom [4, 5]

Country	Annual CO2 Emissions (kt)	Per Capita (t) 1 t =1,000 kg	% of World Total
SaudiArabia	464,481	17.04	1.38%
United Kingdom	493,505	7.863	1.47%

The use of solar air-conditioning system can save such emission of carbon dioxide in order to have positive impact on the environment. The average amount of CO_2 that can be saved when using solar energy is 392 g CO_2/kWh [6]. For typical house in Saudi Arabia of 5 kW cooling power, using solar air-conditioning can save major amount of CO_2 emission as shown in Table 3.

Table 3: CO_2 Emission Saving

Period	CO2 Emission Saving
Hourly	2.544 kg of CO2
Daily	61 kg of CO2
Annually	22,289.5 kg (21.9 UK ton) of CO2

IV. SYSTEM DESIGNS

Solar air-conditioning systems can meet continuous operation (day and night) based on different types of thermal energy storage systems. The designs for 24-hour solar air-conditioning systems are categorized based on the storage techniques in use, as follows: (heat, cold and refrigerant).

In the heat storage system, the stored hot thermal energy is supplied to the generator when the incident solar radiation is insufficient to produce therequired generator temperatures. In the cold storage system,the cold storage tank is introduced after the evaporator. The losses to the environment in thissystem can be expected to be lower than in heat storage system because of the lower temperature difference betweenworking and ambient temperatures. In the refrigerant storage system,the refrigerant storage tank is associated withthe condenser where the storage tank accumulates therefrigerant during the hours of high solar insolation. Then,this stored liquid refrigerant can be regulated at other times(e.g., nighttime) to meet the required cooling loads.

The refrigerant (water) is released from the absorbent (LiBr) when the refrigerant-absorbent solution is heated in the generator. The refrigerant vapor travels to the condenser while the weak absorbent-refrigerant solution moves to the absorber. The refrigerant experiences a throttling process as it passesfirst to the evaporator and then to the absorber, and it isreabsorbed by the weak solution to create a strong refrigerantsolution. The solution is then pumped to the generator to complete the cycle. The heat exchanger between thegenerator andabsorber is used to increase the efficiency of thesystem.

Several valves that are configured with the storage systems direct the flow for nighttime and daytime operation for the three systems. For the three systems, the heat is rejected to the environment by natural convection or forced fan. The total electricity requirement for any of the three systems is limited to that needed by the solution pump.

The advantages and disadvantages for each of designs are summarizedin Table 4. The heat storage system has the highest storage capacity (1,896 kg) and the cold and refrigerant storage systems have the lowest storage capacity (100.6 kg and 108.5 kg, respectively), with a slight difference between the two.Based on thermodynamic analysis, the refrigerant storage found to be the most suitable design due to mass storage size and collector area.

The systems are designed to meet a constantcooling load over the 24 hours under the steady-state operationmode.

Table 4: Comparative Analysis of the Three Designs

Design	Advantages	disadvantages
Heat Storage	Higher COP in nighttime operation	• Larger solar collectors area • Components of the system operate day & night. • Storage tank requires thick insulation.
Cold Storage	• Less complexity in the controlrequirements • Components of the systemoperate only in daytime.	Large evaporator and generator size.
Refrigerant Storage	• Smaller solar collector area • Strengthrequirements are notcritical. • Storage tank has thin insulation.	Evaporator operates day and Night.

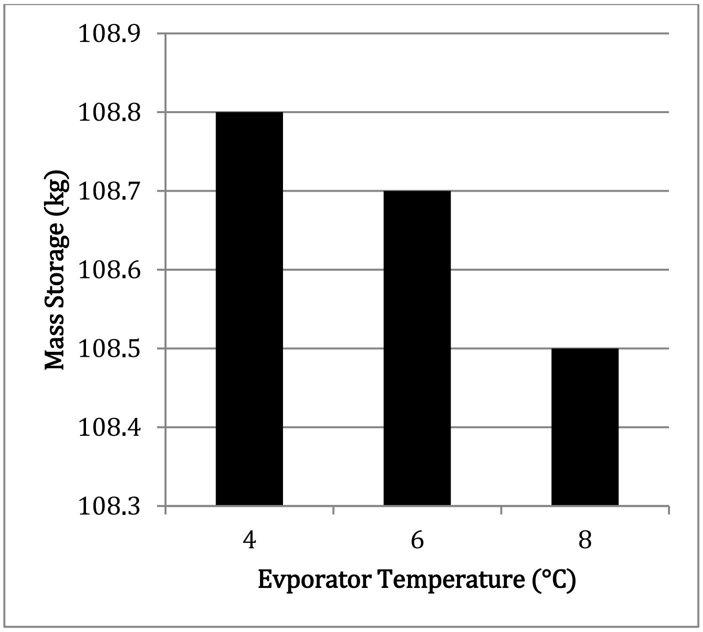

Fig. 2, Mass Storage by Evaporator Temperature

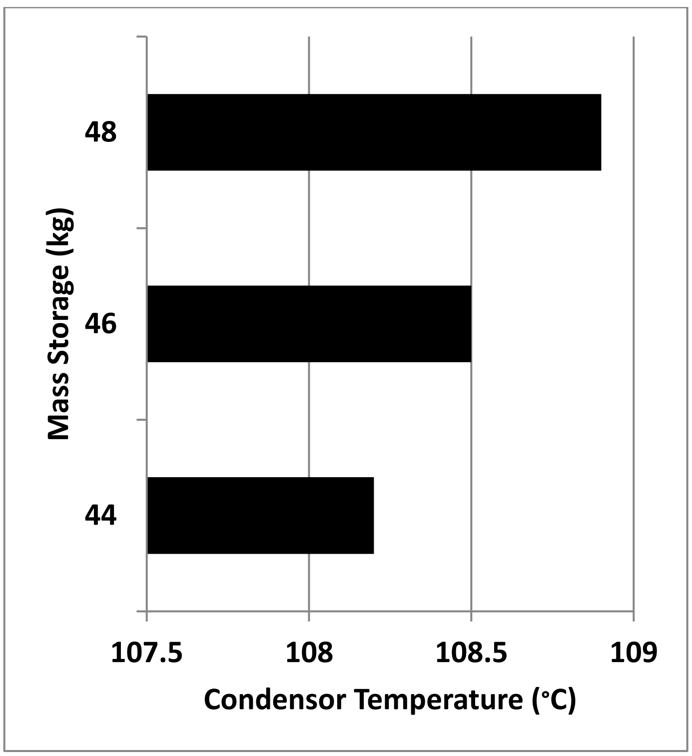

Fig.3. Mass Storage by Condenser Temperature

Using simulation software, engineering equation solver (EES), Fig. 2 shows the effect of evaporator temperature on the mass storage for the refrigerant storage system. The mass storage decreases when the evaporator temperature is higher which indicates that increasing the evaporator temperature will result in cost savings due to the reduction in storage tank. Similarly, Fig. 3 compares the mass storage for the refrigerant storage system versus condenser temperatures using simulation software, engineering equation solver (EES). It shows that the mass storage increases as the condenser temperature increases.

The analysis results show that as the solar available time for the refrigerantstorage system increases, which is applicable for summer,the mass storage capacity decreases. This indicates thata location featuring longer solar availability is highly suitablefor this system. For locations where the solar available time is 14.5h, the storage capacity is decreased to less than 75 kg.

V. Cost of collector IN three systems

The cost of individual components depends on the heat capacity of the components. Higher heat capacity corresponds to a higher heat exchange area required for each component, which further corresponds to a higher cost for that component. The collector rate for flat plate collector is $230/m^2, as stated by the Intelligent Energy-Europe (IEE) program). The collector cost for cold storage system is the most expensive one ($12,259) while it is the cheapest for the refrigerant storage ($5,106). For the heat storage system, the collector cost is $10,143.

VI. Conclusion

The development of solar air-conditioning system has major advantages towards energy saving and carbon dioxide emission elimination. In this paper, three solar-air-conditioning designs for 24-hour a day based on storage methods have been discussed. The features and benefits for each design in term of storage capacity and collector cost have been analyzed. The best storage design is the refrigerant storage as the collector cost is small compared to the other. Moreover, non-insulated storage tanks are required for refrigerant storage systems. These twofactors indicate that the cost of the refrigerant storage system is lower than the other two systems.The improvement of mass storage by condenser and evaporator temperatures will positively affect the design parametersand system selection.

References

[1] Y. Alyousef and M. Abu-ebid. “Energy Efficiency Initiatives for Saudi Arabiaon Supply and Demand Sides”. www.intechopen.com (Saudi Electricity Company),2010.

[2] King Abdullah City for Atomic and Renewable Energy, Towards Sustainable Energy Mix For Saudi Arabia. 3rdSaudi Solar Forum, Riyadh, Saudi Arabia, April 17, 2011.

[3] H.-M. Henning."Solar assisted air conditioning of buildings – an overview". Applied Thermal Engineering, 1734-1749, 2007.

[4] http://data.worldbank.org/indicator/EN.ATM.CO2E.KT/countries. last accessed May 2015.

[5] http://data.worldbank.org/indicator/EN.ATM.CO2E.PC/countries. last accessed May 2015.

[6] Sam Friggens, How much Carbon Dioxide do solar panels save? http://blog.abundancegeneration.com/2013/08/how-much-carbon-dioxide-do-solar-panels-save. Last accessed May 2015.

Journal of Energy Challenges and Mechanics
http://www.nscj.co.uk/JECM/
ISSN 2056-9386
Volume 2 (2015) issue 4, article 4

Combined break-junction tunneling and STM/STS studies of the β-tungsten-type superconductor Nb_3Sn below and above T_c

对临界温度上下β-钨型超导体 Nb_3Sn 的破结穿隧与 STM/STS 之结合研究

Toshikazu Ekino[1*], Alexander M. Gabovich[2], Yuta Sakai[1], Akira Sugimoto[1]and Jun Akimitsu[3]

[1]*Hiroshima University, Graduate school of Integrated Arts and Sciences, Higashihiroshima739-8521, Japan*
[2]*Institute of Physics, National Academy of Sciences, Kiev 03680, Ukraine*
[3]*Aoyama-Gakuin University, Department of Physics, Sagamihara 252-5277, Japan*

ekino@hiroshima-u.ac.jp

Accepted for publication on 25 December 2015

Abstract **- Electron-tunneling spectroscopy was employed to investigate the well-knownβ-tungsten-type Nb_3Sn superconductor. The primary measurements were done by means of the surface-sensitive break-junction technique. BCS-like energy-gap features are reproduced in the superconducting state. Reproduced conductance humps outside the superconducting gap structures are commonly observed. Such hump structures are complementary to coherent peaks at the superconducting-gap edges and resemble the pseudo gap phenomena revealed in copper-oxide high-T_c superconductors. Those humps become the only gap-like manifestations above T_c. The possible origin is discussed in terms of the charge-density wave (CDW) formation associated with the structural phase transition. The scanning tunneling microscopy/spectroscopy (STM/STS) measurements were also carried out to obtain complementary density-of-states data.**

Keywords – **Tunneling, break junction, STM/STS, energy gap, A-15 compound, high-T_c superconductor.**

I. INTRODUCTION

One of the intriguing features of high-T_c superconductors is the manifestation of the gap-like structures above the superconducting critical temperature. This puzzling issue has been intensively investigated in terms of either the precursor Cooper-pairing effects or the competing phenomena suppressing the superconducting critical temperature [1]. The nature of the normal-state gap formation in cuprate high-$T_c$superconductors is not perfectly understood to date, althoughseveral possible origins were suggested based on the formation of competing charge density waves (CDWs) with accompanying periodic lattice distortions in the layered crystal structures. The CDW appearance in cuprate superconductorswas confirmed experimentally and theoretical attempts have been made to identify CDW manifestations with the observed tunnel and photoemission spectral data[1].It is natural to search for the existence of such phenomena in the other classes of superconductors with CDW anomalies occurring at temperatures both higher and lower than T_c.A-15 (β-tungsten) compound Nb_3Sn, which hadone of the highest superconducting critical temperatures, T_c, over a long periodbefore the discovery of high-$T_c$cuprate superconductors 30 years ago[2], is very promising in this connection.

This materialdoes not exhibit a layered crystal structure appropriate to cuprates.However,its lattice includes orthogonal linear chains of Nb atoms alongprincipal cube axis directions[2]. Such quasi-one-dimensional feature tends to induce structural anomalies driven by peculiarities of the normal-state electron density of states, $N(E)$, near the Fermi level, which determines T_c. Actually, A-15 materials undergo tetragonal distortions below certain temperatures,T_m>T_c.Hence, Fermi surface is partially gapped by concomitant CDWs, which is detrimental to superconductivity. Such an interplay between superconducting pairing and CDWswas intensively studied for a number of A15 compounds both experimentally and theoretically, and Nb_3Sn ($T_c \approx 18$ K) isthe representativecase [3-5].The superconducting and CDW order parameters inevitably lead to the corresponding superposed energy gaps induced by both Cooper and electron-hole pairings. The origin of superconductivity and the gapping features of A-15 compounds wereeffectively explored by the conductance spectroscopy in the tunnel [6] and point-contact [7] regimes as the typical methods to probe these phenomena. The experiments revealed a single clear-cut superconducting gap, and another feature at higher voltages most probably connected to the structural transition [8].

In this paper, tunneling measurements of Nb_3Sn single crystals are presented using break-junction (BJ) [9] and the scanning tunneling microscopy/spectroscopy (STM/STS)techniques on the basis of the previous works [6, 8]. The experiments were carried out focusing on both the superconducting gap features and the electronic peculiarities of $N(E)$ emerging due to the structural (martensitic) transition intimately associated with CDWs. The mean-field equations describing competing superconducting and electron-hole pairings are the same for the majority of microscopic descriptions of the CDW pairings[1, 4, 5]. Therefore, the important consequencesare similar. One expectsthe manifestations of CDWs in the quasiparticle conductance $G(V) = dI/dV$, where I denotes the quasiparticle tunnel current across thejunction. The $G(V)$ curve in CDW superconductors is a complicated functional of the superconducting, Δ, and dielectric (CDW), Σ, energy gaps [1, 5, 10]. In the BJTS method,$G(V)$ doesnotinclude a simple convolution of the gapped electron density of states as in the conventional Bardeen-Cooper-Schrieffer (BCS) model of superconductivity.

II. Experimental procedures

Single crystalsof Nb_3Sn weregrown by a vapor transport method. The sample resistivitywasmeasuredin a standard dcfour-probeconfiguration. The main measurement techniques employed here were the tunneling spectroscopy using the break junction (BJTS) and the low-temperature ultra-high-vacuum(~ 10^{-8} Pa) STM/STS with a PtIr tip. In theBJTS technique, clean and unaffected superconductor – insulator – superconductor (SIS) junction interface can be obtained *in situ* along the crack of the tiny single-crystal piece at $T = 4$ K in the helium atmosphere. Thebreak junction configuration therefore possesses the gap peak-to-peak interval to be $4\Delta/e$ instead of $2\Delta/e$ of the superconductor – insulator – normal metal(SIN) junction, where e denotes the elementary charge. This relationships are also validwhen the gap has a dielectric (CDW) origin.The BJ tunneling spectra were measured using a low-frequency ac-modulation technique with a low-noise lock-in amplifier. When the junction wasmechanically stable, a long-period full bias-voltage scantaking 30 min – 1hr or more was adopted to eliminate any parasitic effects in the tunnel currents.

The main aim of adopting BJTS is to exploreverydelicate electronic properties using a conventionalsensitive technique, but we also carried out the STM/STS measurements in order to obtain further evidence detectingthe existence of the interplay between superconducting and CDW pairings.Here, the preliminary STM/STSresults are presentedtogether with the BJTS data.

III. Results and discussion

The temperature dependence of the resistivity forthe Nb_3Sn sample showed a sharpdrop at the superconductingtransition and becomes zero at $T = 18.1$ K, therebyindicating the sufficientquality of the test sample.

Whatever the details, knowing high T_c of Nb_3Sn, we should analyze its gapstructuresbearing in mindthe expected strong-coupling nature of the superconducting electron pairing. Here the BJTS resultsareshown inFigure 1 for severaldifferentjunctions.The data shown here constitutearepresentative group among junctions with similar characteristics. One can see the main gap peaks at ± 2.0 – 2.2 mV and broad peaks at ± 2.8 – 3.0 mV. Assuming the SIS nature of the junction, these values correspondto $\pm 2\Delta/e$.Sometimes the double-peaked gap structures including both peak values (± 2.0 and ± 2.8 mV) are observed. This two-gap feature qualitatively resembles the two-band superconductivity as reported also in $Nb_3Sn$by point-contact spectroscopy measurements[11]. In our case, the second gap valuesscatter substantially although the basic-gap value is almost the same.Thus, we did observe the double-gap structures but in most cases the single-gap feature was found showing either≈ 3 mV or ≈ 2 mV values.The latter characteristics always demonstrate sharp gap structures as is shown in the figure. Therefore, we could not identify, which of the observed gaps is intrinsic for this compound.

The $G(V)$ curve with the smaller gap and distinct conductance structurecorresponds to the standard BCS quasiparticle density of states $N(E,\Gamma) = |\mathrm{Re}\{(E-i\Gamma)/[\Delta^2-(E-i\Gamma)^2]^{1/2}\}|$, where E is the energy, Γ is aphenomenological broadening parameter [12].The value of energy gap, 2Δ, was found by fitting the SIS conductance, determined by the convolution of two $N(E,\Gamma)$ factors. It gives the gap-peak energy, regardless of the Γ value [13] .In the fitting, we included the thermal smearing effect in addition to Γ broadening. Similar gap-peak positions were foundalthough the spectra are of different quality. The gap values thus obtained are $2\Delta(4\mathrm{K}) = 2 – 2.8$meV. The results therefore reveal the gap ratio $2\Delta/k_BT_c = 2.8 – 3.6$, which is in the range of the *s*-wave-pairing BCS ratio 3.52. The value, which is smaller than the BCS one, indicatesthe existence of the local non-stoichiometriclow-T_c region.The secondary gap features were also observed in the novel iron-based binary superconductors, and discussed in connection with either the local off-stoichiometric effect or the multi-gap superconductivity [14].

In the middle experimental curve of Fig. 1, the intensive dipstructures are observed at ± 12 mV. Such features were often attributed to the manifestation of the strong electron-phonon interactionexpected for this compound

[15].However, it should not be the case here, becauseof irreproducibility andan unusual depth of the dips as comparedwith the strong-coupling features. Instead, thedipsare probably generated by the proximity effects and/or the weak-link behavior in the local patches of thejunction area.

For higher bias voltages at the same fixed $T = 4.2$K, one can observe shoulders or hump structures at ± 40 – 60 mV, in addition to weak but distinct hump features at biases ± 20 – 30 mV.

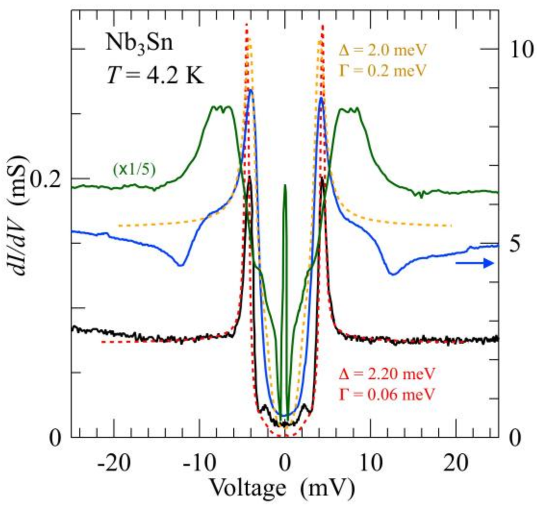

Fig.1. The tunnel conductance $G(V)$ of superconducting Nb_3Snjunctions obtained in break-junction tunnel-spectroscopy (BJTS)measurements. These spectra are obtained fordifferent junctionscorresponding to samples from the same batch. The dashed lines are the fitting results based on theBCSdensity of states $N(E,\Gamma)$ (see the details in the text).

In the top curve of Figure 2, the representative superconducting gap featureswithextra ± 20 mV humps areshown. The appearance of such features depends on the junction, i.e. they are often absent and not consistent with the superconducting gapat ± 4 – 6 mV. Therefore, itshould not berelated tosuperconductivity.This is alsoseen from Fig. 1, where there are no distinct features at around those bias voltages. The humps at ± 20 mVexhibit the weakchange, namely, 2 – 4 %, against the background. Such structures, whicharereproduced by our present measurements, werealready clearly observed and presented previously forNb-Sn break junctions [6]. Inthosedata, the peculiarities occurredbetween ± 20 mV and ± 30 mV. Such a subtle intensity could be associated with the strong electron-phonon interaction, which has been believed to be the most probablemechanism to inducesuperconductivity in Nb_3Sn and other A-15 compounds [15]. This is, however, not the case in the present measurements, because the peculiarities are too large to be the strong-coupling features. It should be emphasized that a caution against interpretation of the outer structures as strong-coupling effects was expressed earlier with the applicationto 5*f*-electron superconductor UPd_2Al_3[16].

An essential method to clarify the origin of such hump structures consists in finding of their temperature evolution. However, the BJTS are mechanically unstable. Hence, it is difficult to systematically measure temperature dependences of the structure concerned in the relevant regionpreserving the identical junction-interface properties.Nevertheless, we were able to follow the trace of the characteristic temperature evolution during the heating process. It is remarkable that the distinctpeak positions at about ± 20 mV, found at a low $T = 4.2$ K, i.e.much below T_c, remained the same during the heating. However, the peaks gradually transformed into heavily broadened and symmetric structuresclearly seenagainst the bias-dependent backgroundeven at temperatures 20.8 K. This temperature lies above the superconducting transition at 18 K. It means that these structures are not directly connected to superconductivity. The thermal smearing of the Fermi distribution function does not influence this broadened gap structure because the energy scale ~1.7 meV corresponding to the temperature 20.8 K is smaller as compared with that of the hump bias location at 20 meV (~ 240 K). The possible origin of gap-structures broadening is the effective widening of the junction area, so that the overall $G(V)$isformed by the averaging of the gap distributions. This conclusion is supportedby the observed relatively high conductance $G(V)$ magnitudes.

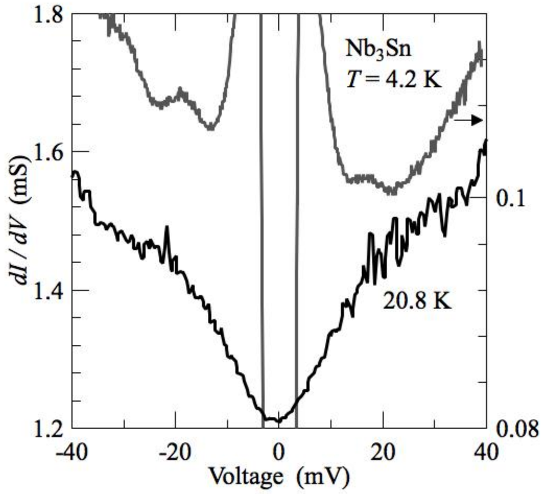

Fig.2. $G(V)$ of BJTS Nb_3Sn junctions in the superconducting state. These spectra are obtained from different junctions at 4.2 K and 20.8 K (>T_c).

We emphasize that the wider humps at ± 40 – 60 mV in the $G(V)$ curves are reproducible in addition to the above mentioned narrower features at $V = \pm 20 – 30$ mV. Thesecharacteristics werediscovered in our previous BJTS measurements, in which merely the broadened humps or the shallow shouldersappearedin these bias voltage regions [8]. The repeated BJTS measurements at low temperatures confirmed the existence of the distinct gap-edge-like peaks among thecommonly observed weakhump or shoulder structures. Figure 3 demonstrates such an example, in which fairly discerniblepeaks appeared at ± 40 mV together with weaker but distinguishable peaks at ± 20 mV. We can therefore attribute the features at ± 40 mV as the dielectric gap

2Σ manifestations [8].The ± 40 mV peaksare in fact clearly visible, being10 percent higher thanthecorresponding background intensity. From these data, it is obvious that the distinct gap-like structures existwell above the superconducting gap energy, which supportsthe conclusion form the data of Figure 2. The finestructures at lower biases of |V| < 20 mV are probably associated with the superconductingweak-link formation with limited critical current density.

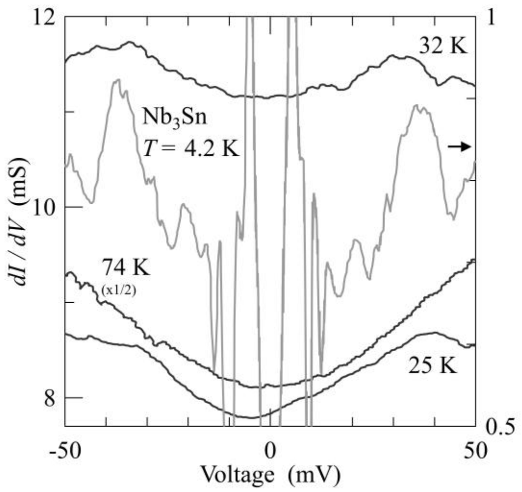

Fig.3. $G(V)$ of BJTS Nb_3Sn junctions in the superconducting and normal states. These spectra were obtained forvaryingjunctionproperties.

To obtain explicit temperature dependence of the high-bias feature constitutesaseparateproblem. We made attempts to clarify how the gap edge moves to lower biases. Unfortunately, the junction properties could not be stable throughout the temperature span.Nevertheless, we managed to observe the characteristics in almost the same patch of the broken junction. The results areshown in Figure 3.The spectral featuresscatter while temperature increases. One can see the gap-edge structures preservewell above $T_c$andgradually disappear, so that theycould not be observed above74K, where one sees only the substantially bias-dependent background. The fact that the high-energy gap-likefeatures do not disappear at $T_c$means that they are induced by such phenomena that exist both in the superconducting and normal state.Therefore, it seems improbable that ± 40 mV peculiarities are due to such precursor effects as fluctuating Cooper pairs. On the contrary, the interaction responsible for the gapping of the electron density of statesis presumably a phenomenon competing with the Cooper pairing for the Fermi surface.The substantial gap-related depression of $G(V)$ near zero bias above $T_c$indicates that the interface quality is sufficienttodetect thequasiparticle tunnel density-of-states evolution during various manipulations, including heating.

The temperature dependence of the gap values obtained from the data presented in Figure 3 is plotted in Figure 4. Since there are not enough data points, it is hard to draw definite conclusions about the thermal evolution of the gapfeatures.However, it is important that at least for this junction, the $G(V)$ curve exhibits no peculiar features at temperatures above 74 K.One should remind the fact that tunneling spectroscopy studies a realcontact interface, in which any subtle structures could be modified or suppressed due to the non-ideal electron scattering at the surface, especially when the temperature is increased inducingstrong thermal broadening of the Fermi distribution function. For this reason, it is very difficult to identify the exact gap closing temperature.

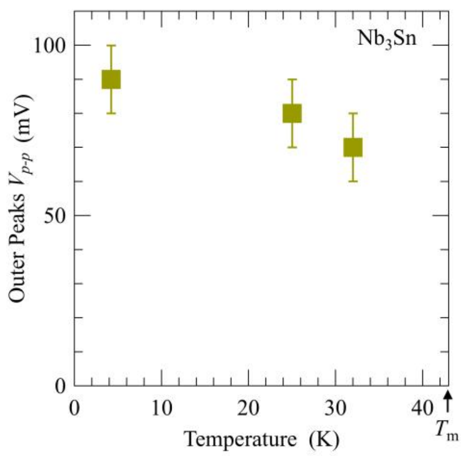

Fig.4. Temperature dependence of the outer peak-to-peak gap valuestaken from Fig. 3.

Nevertheless, one can recognize that the outer peak-to-peak distance $V_{p-p}$is reduced with the increase of temperature.Itshows the trend to close around the martensitic transition temperature T_m = 43 K of Nb_3Sn demonstrating a conventional mean-field gap evolution behavior. Since V_{p-p}= 4Σ/e, the conventional gap-to-$T_m$ratiocan be estimated as $2\Sigma/k_BT_m$~ 12, which is 3-4 times larger than the BCS mean field value.

The obtained value is typical for dielectric (CDW) transitions found in a number of materials [1,5].Moreover, the characteristicenergy scales and behavior of the normal-state gap observed here resemble the CDW gap formation and evolution in low dimensional conductors with the nesting sections on the Fermi surface [1,5,17]. Therefore, we believe that the superlatticeappears with the concomitant electron spectrum gapping driven by one of the mechanismssuggested for A-15 compounds [1-5]. Whatever the subtle theoretical details, therelevant phenomenon(the consequence of which is observed here)really occurs in A-15 compound Nb_3Sn and is known as the martensitic structural phase transition[2-4]. Below thecharacteristic temperatureT_m, the tetragonal periodic lattice distortions appeardeformingthe original cubic lattice.The transition isdriven by the Peierls-type instability due to displacement of Nb atoms. The concomitant CDW leads to the quasiparticle gap formation in the original electronic density of states $N(E)$. However, only a small Fermi surface section is affected and distorted by the dielectric energy gap created by this transition. Since the electron spectrum changesarerelatively weak, the electronic transport properties arenot significantly affected as is confirmed bythe experiment[8]. Therefore, not so muchattention was paid previouslyto the peculiarities of the tunnel conductance spectra characterizing Nb_3Sn tunnel junctions. Moreover, CDW distortions in Nb_3Sn seem to be spatially inhomogeneous similarly to what is inherent to cuprate layered structures [1, 10]. This would make the electron spectrum due to the CDW instability much smoother than in conventional types of sharp second-kind phase transitions. Therefore, the CDW gapping reveals itself in the tunnelingconductance $G(V)$ as a weak pseudogap-like feature well known for other objects [1, 10]. This is readily understood taking into account the inhomogeneity effects and the gapping of only a small Fermi surface section[1].

In order to investigate the gap structure of Nb_3Snmore thoroughly and systematically, the comparable measurementsof STM/STS were carried out.In fact, as far as we know, there was merely a preliminary report on STM/STS measurements presented 3 decades ago [19]. The technical difficulty in the measurements of A-15 cubic compounds like Nb_3Sn is the lack of apparent cleave plane in the crystal. This is a fatal weakness of the scanning measurements using this kind of the samples. One should remind that there are enormous numbers of reports on the STM/STS measurements of the conventional and novel superconductors, but unfortunately all of them were done using layered compounds and/or thin films in which the surface states differ substantially from their bulk counterparts. In what follows, we describe the STM/STS measurements of Nb_3Sn.

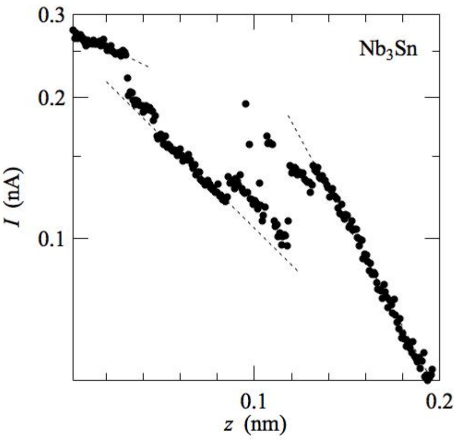

Fig. 5. Dependence of vacuum tunneling current I on the PtIr tip – Nb_3Sn sample distance at T = 4.9 K.

Figure 5 demonstrates the dependence of tunneling current I on the tip-sample distance z, as the initial procedure of the STM measurements. The Nb_3Sn sample is taken from the same batch as was used for the BJTS measurements. The data points are strongly scattered. The work functionϕ, the magnitude of which characterizes the quality ofthe crystal surface flatnesscan be recovered, in principle, fromour $I(z)$ dependences measured by STM/STS. Since the present sample does not possess the layered structure, one should not expect the requiredatomic flatness of the crystal surface. This must be the major reason of the data scatter in Fig. 5. Nevertheless, the conventional exponential $I(z)$ dependences are obtained insome surface areas. From corresponding $I(z)$,rough estimations of ϕ are possible. The estimated values of ϕ thus obtained are in the range 0.7–3.2eVfor z < 0.2 nm. As comes about from the data, for smaller z the work function ϕ is lower, the changes occurring abruptly. Thereason may be non-trivial.Namely, the work function reflects the degree of surface roughness.On the other hand, the shorter is the electron tail outside the conducting sample,the higher should be the corresponding ϕ value.In the vicinity of the rough interface (small z) the electron density in the vacuum in some patches may be larger than for the smooth interface. Hence, the apparent ϕ is reduced. On the contrary, for largerzthe influence of atomic corrugationsis smoothed out, so that the natural electronic conditions with the intrinsic, larger, ϕ are restored.As a result, the measured work functionϕ andits z-dependenceare fairly good characteristicsof the surface properties.At the same time, in the purely layered superconducting material nearly ideal values of ϕ =3 –5 eVwere found [20].

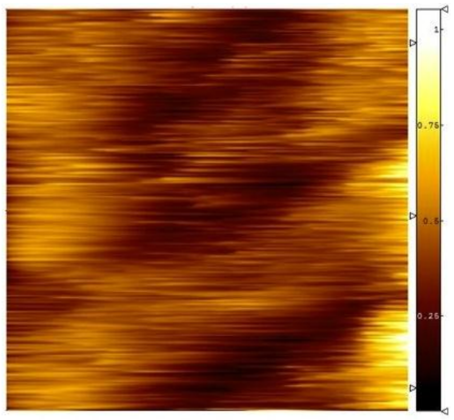

Fig. 6. STM image of the *in situ* cracked surface of Nb_3Sn at T = 4.9 K.The scanning area is 10 nm × 10 nm,V = 0.1 V and I= 0.4nA. Vertical bar on the right side indicates the relative height of the topography (the brighter is the higher).

Figure 6 demonstratesa trial STM topographymeasured on the Nb_3Sn surface.To our knowledge, this is the first STM observationof the A-15-compound surface obtained here for a small area of 10 nm × 10 nm.This circumstance justifies thecurrent presentation notwithstandingitstopography non-atomic resolution. As is expected from the I-z characteristics shown in Figure 5, it was difficult to resolve the surface atomic arrangements. Nevertheless, the image shown here was reproducedduring other scanning runs. In this STM image, there are contrastingstripes running inthe diagonal direction. The period of the stripes is about 3.5 nm, which corresponds to 6.5 times unit cell constanta_0.At present, the detailed features of the stripes, which may have either electronic or atomic origin, are not known, but the stripe existence seems to argue in favor of the normal-state gapping found in this compound. It is alsointeresting to note that the period of those stripes is similar to that observed on the surface of high T_c superconductors [1].

Figure 7 shows $G(V)$ measured for Nb_3Sn in the STSmode.Thesuperconducting-gap like structure is clearly visible at 4.9 K. In principle, the gap-edge peaks in the SIN junction (similar to thosein the STS one) occur athalf the peak interval of BJTS. However, in the presented data, the $V_{p\text{-}p} \approx 16$ mVis larger than what was expected from the BJTS, although the samples originated from the samebatch. Since the peak positions identified with the gap-edgelocations are often overestimated in the broadened spectra, we adopted the fitting procedure using the $N(E,\Gamma)$ in the SIN configuration. The result indicates the gap value of $2\Delta \approx 10$ meV, which is smaller than the observed $eV_{p\text{-}p}$, but it is still much larger than that from the $2\Delta \sim 3$ meV of the BJTS. Another discrepancy between the experimental and calculated curves is the hugeleakage in the sub-gap region around zero bias, which could not be reproduced even by increasing the broadening parameter Γ.Such a situation may be a result of simultaneous probing ofthe non-gapped nanometer-size domains.

When the bias voltage is increased, another characteristic feature appeared, which is the broad hump structures at the biases of ± 40 – 50 mV. These features must correspond to the normal state gap observed in the BJTS, but the hump positions of ± 40 – 50 mV in STS hereare the same as $\pm 2\Sigma/e$ of the BJTS, in spite of the expected $\pm 4\Sigma/e$. Thishigh-bias hump feature was already observed in the Nb_3Sn – metal junction without noticing as the gap-edge structure [15].The presented STS measurementsraiseissues to be clarified in the future.

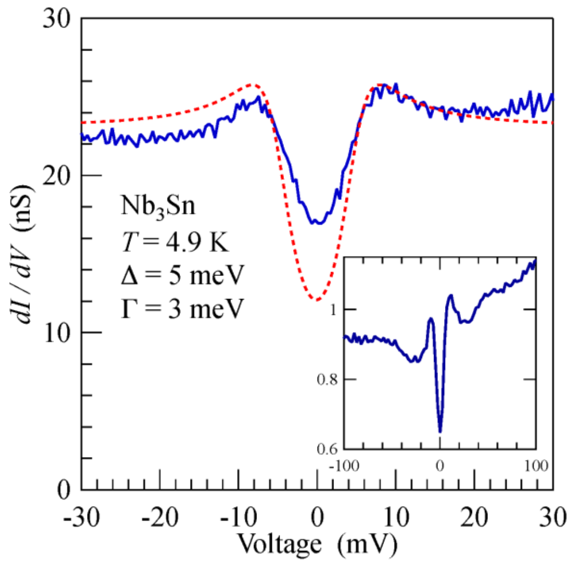

Fig. 7.Tunneling conductance $G(V)$ in the superconductinggap region measured by STS. The inset shows the high-bias feature.

The coexisting superconducting-gap and hump structures presented here in Nb_3Sn are very similar to those found in the tunneling-conductance characteristics of high-$T_c$cuprates and recently reported iron-chalcogenides except for the energy scales[1, 14, 21]. These apparent similaritystimulates further studies to compare the objects concerned, whichwe are going to study in more detail.

III. Conclusion

The classical superconductor Nb_3Sn wasstudied by break junctionand scanning microscopy/spectroscopytunneling techniques. We observed superconducting-gap structuresofthe BCS size and the humps most probably being a manifestation of the normal state gap, accompanying the martensitic phase transition. The low-temperature humps outside the superconducting gap obtained by break-junction tunneling are confirmed by thepreliminary STM/STS measurements. There is the apparent discrepancy in the energy scales between BJTS and STM/STS, whichwaits forclarification.The resultant normal gap to transition temperature ratio from the BJTS is similar to that found inthe low-dimensional conductor $NbSe_3$, which was studied decades ago. These results strongly suggest that the normal-state gap is induced by the Peierls-type instability ubiquitousto low-dimensional electron structures, in which nested sections of the Fermi surfaceare removed below the structural transition. Similar CDW-like phenomena were observedincupratesboth directly and asthe pseudogapmanifestations. They were also found in the novel iron-chalcogenide superconductors together with spin-density waves [22].In all such materials CDW gaps close at temperatures higher than the superconducting critical one, although both order parameters coexist at temperatures lower than T_c.

References

[1] A.M. Gabovich, A.I. Voitenko, T. Ekino, M.S. Li, H.Szymczak, M. Pekala, Adv. Condens. Matter Phys. **2010**, 681070, 2010.
[2] L.R. Testardi, Rev. Mod. Phys. **47**, 637, 1975.
[3] L.P. Gorkov, Zh. Eksp. Teor. Fiz. **17**, 525, 1973.
[4] G. Bilbro, W.L. McMillan, Phys. Rev. B**14**, 1887, 1976.
[5] A.M. Gabovich, A.I. Voitenko, M. Ausloos, Phys. Rep. **367**, 583, 2002.
[6] J. Moreland, J.W. Ekin, J. Appl. Phys. **58**, 3888, 1985.
[7] R. Escudero, F. Morales, Solid State Commun.**150**,715, 2010.
[8] T. Ekino, A. Sugimoto, Y. Sakai, A.M. Gabovich, J.Akimitsu, Low Temp. Phys. **40**, 1182, 2014.
[9] T. Ekino, T. Takabatake, H. Tanaka, H. Fujii, Phys. Rev. Lett. **75**, 4262, 1995.
[10] T. Ekino, A. M. Gabovich, M. S. Li, M. Pękała, H. Szymczak, A. I. Voitenko, Phys. Rev. B **76**, 180503, 2007.
[11] M. Marz, G. Goll, W. Goldacker, R. Lortz, Phys. Rev. B **82**, 024507, 2010.
[12] R.C. Dynes, V. Narayanamurti, J.P. Garno, Phys. Rev. Lett.**41**,1509, 1978.
[13] T. Ekino, H. Fujii, M. Kosugi, Y. Zenitani, J. Akimitsu,Phys. Rev. B **53**, 5640, 1996.
[14] T. Ekino, K. Nagasaka, Y. Sakai, A. Sugimoto, A.M. Gabovich, Phys.Procedia**65**, 65, 2015.
[15] J. Geerk, U. Kaufmann, W. Bangert, H. Rietschel, Phys. Rev. B **33**, 1621, 1986.
[16] J. Geerk, H.v. Lohneysen, Phys. Rev. Lett. **99**,257005, 2007.
[17] T. Ekino, J. Akimitsu, Jpn. J. Appl. Phys. Suppl. **26**, 625, 1987.

[18] P. Monceau, Adv. Phys. **61**, 325, 2012.
[19] A.L. de Lozanne, S.A. Elrod, C.F. Quate, Phys. Rev. Lett.**54**, 2433, 1985.
[20] A. Sugimoto, K. Shohara, T. Ekino, Z. Zheng, S. Yamanaka, Phys. Rev. B **85**, 144517, 2012.
[21] T. Ekino, Y. Sezaki, H. Fujii, Phys. Rev. B **60**, 6916, 1999.
[22] A. Sugimoto, T. Ekino, A. M. Gabovich, Phys. Rev. B **90**, 224503, 2014.

Journal of Energy Challenges and Mechanics

http://www.nscj.co.uk/JECM/

ISSN 2056-9386
Volume 2 (2015) issue 4, article 5

Damage assessment of water distribution pipelines after the 2011 off the pacific coast of Tohoku earthquake

2011年東北地方太平洋沖地震之后的配水管道损伤评估

Yoshihisa Maruyama[1*], Shigeru Nagata[2], Kazue Wakamatsu[3]

[1]*Department of Urban Environment Systems, Chiba University, 263-8522, Japan*
[2]*Kajima Technical Research Institute, Kajima Corporation Co., Ltd., 182-0036, Japan*
[3]*Department of Civil Engineering, Kanto Gakuin University, 236-8501, Japan*

ymaruyam@faculty.chiba-u.jp

Accepted for publication on 25 December 2015

Abstract - **The 2011 off the Pacific coast of Tohoku earthquake occurred on March 11, 2011 with a moment magnitude of 9.0. The water supply was disrupted for approximately 2.2 million households because of this event. In this study, the applicability of empirical fragility functions of water distribution pipelines is evaluated using the damage ratios calculated for the above earthquake. To achieve this objective, the damage dataset compiled by the Ministry of Health, Labor and Welfare of Japan is employed to calculate the damage ratios. The damage ratios are obtained with respect to pipe material and diameter. Empirical fragility functions are compared with the actual damage ratios, and the accuracy of estimation is discussed.**

Keywords – **2011 off the Pacific Coast of Tohoku earthquake, water distribution pipe, damage ratio, fragility function.**

I. INTRODUCTION

On March 11, 2011, the 2011 off the Pacific coast of Tohoku earthquake occurred with a moment magnitude of 9.0. Lifeline facilities such as electric power supply, water supply, sewage, city gas supply, and telecommunication systems were affected by the ground motion and tsunami. The water supply was disrupted for approximately 2.2 million households [1]. The Ministry of Health, Labor and Welfare of Japan (MHLW) investigated the incidents of damage to water distribution pipelines after this event [2]. According to their report, pipe breakages were found in Iwate, Miyagi, Fukushima, Tochigi, Ibaraki, and Chiba Prefectures. They recorded the locations of pipe breakages, as well as the pipe materials and diameters in these locations.

In this study, the damage ratios of water distribution pipes are calculated in the six prefectures using the damage dataset compiled by MLHW. The relationship between the damage ratios and the ground motion intensity is evaluated, and the applicability of fragility functions developed in previous studies [3-6] is discussed. Lastly, a damage estimation method on a regional scale is proposed in the case of occurrence of a gigantic earthquake.

II. DATASETS EMPLOYED IN THIS STUDY

The damage dataset of water distribution pipes compiled by MHLW is employed in this study. The locations of damage incidents were revealed using the Geographical Information System (GIS). The GIS dataset that identifies the water-supply areas in Iwate, Miyagi, Fukushima, Tochigi, Ibaraki, and Chiba Prefectures, compiled by the Ministry of Land, Infrastructure, Transport and Tourism (MLIT), is also employed [7]. The National Institute of Advanced Industrial Science and Technology (AIST) of Japan developed a system named QuiQuake to draw a map of the distribution of ground motion intensity just after an earthquake [8]. QuiQuake provides wide and detailed strong ground motion maps based on the observed ground motion records.

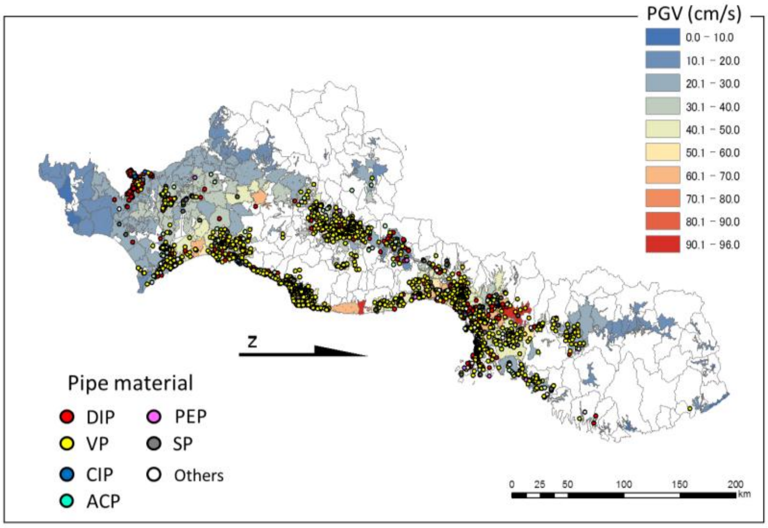

Fig. 1. Locations with incidents of damage to water distribution pipes, and distribution of the peak ground velocities in the water-supply areas after the 2011 off the Pacific coast of Tohoku earthquake.

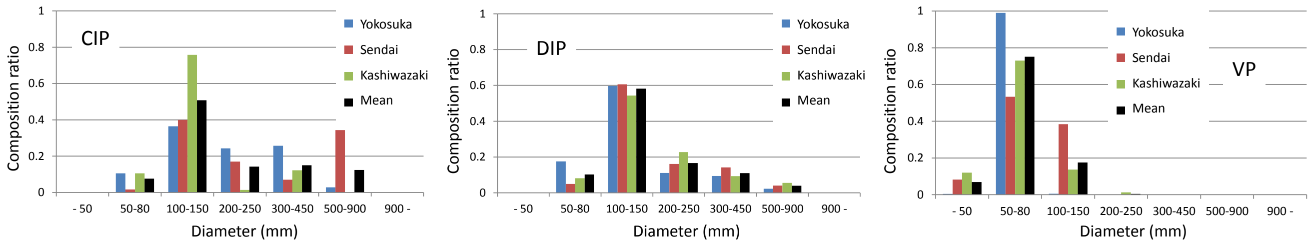

Fig. 2. Composition ratios of pipe length vs. diameter for CIP, DIP, and VP.

Figure 1 shows the locations that had incidents of damage to water distribution pipes, and the distribution of the mean of the peak ground velocity (PGV) for each water-supply area. Symbols assigned to the damage incidents were classified based on the pipe material: ductile cast iron pipe (DIP), vinyl pipe (VP), cast iron pipe (CIP), asbestos cement pipe (ACP), polyethylene pipe (PEP), steel pipe (SP), and others. In all, 5,656 pipe breakages are considered in this study.

The damage ratio of a water distribution pipeline is defined as the number of pipe breakages divided by the pipe length (km). The length of pipes, grouped based on material, in each water-supply area is available from the 2011 census data compiled by Japan Water Works Association (JWWA) [9], but the length of pipes, grouped based on diameter, is not compiled in the census data. Hence, the proportions of pipe lengths for different diameters are estimated using the detailed GIS datasets for water pipelines in the three municipalities: Yokosuka City (Kanagawa Prefecture), Sendai City (Miyagi Prefecture), and Kashiwazaki City (Niigata Prefecture). Figure 2 shows the composition ratios of pipe lengths with respect to diameter for CIP, DIP, and VP. The mean of the ratios were multiplied by the total length of pipes of a particular material to calculate the damage ratio for that material for different diameters.

III. Evaluation of Damage Ratios of Water Distribution Pipes

Figure 3 shows the distribution of damage ratios for DIP with diameters in the range of 50-80, 100-150, 200-250, 300-450, and 500-900 mm. The damage ratios were larger in the areas where intense ground shaking and extensive liquefaction were observed.

To estimate the damage ratios of water pipes, the following formula is commonly used in Japan [3].

$$R_m(v) = C_p C_d C_g C_l R(v) \quad (1)$$

where R_m is the damage ratio, C_p, C_d, C_g, and C_l are correction coefficients for the pipe material, diameter, geological condition, and liquefaction occurrence, respectively, and v is the PGV of ground motion. $R(v)$ is the estimate for the damage ratio of CIP with diameter in the range of 100–150 mm; this is also proposed in other studies [4-6].

Figure 4 shows the relationship between PGV and the damage ratios of water distribution pipes with the diameter in the range of 100-150 mm. In this figure, the estimations done by previous studies [3-6] based on Eq. (1) are also indicated. The correction coefficient for the pipe material (C_p) is set to be 0.3 for DIP, 1.0 for VP, and 1.0 for CIP. C_d is set to be 1.0 based on the study by Isoyama *et al.* [3]. The effects of

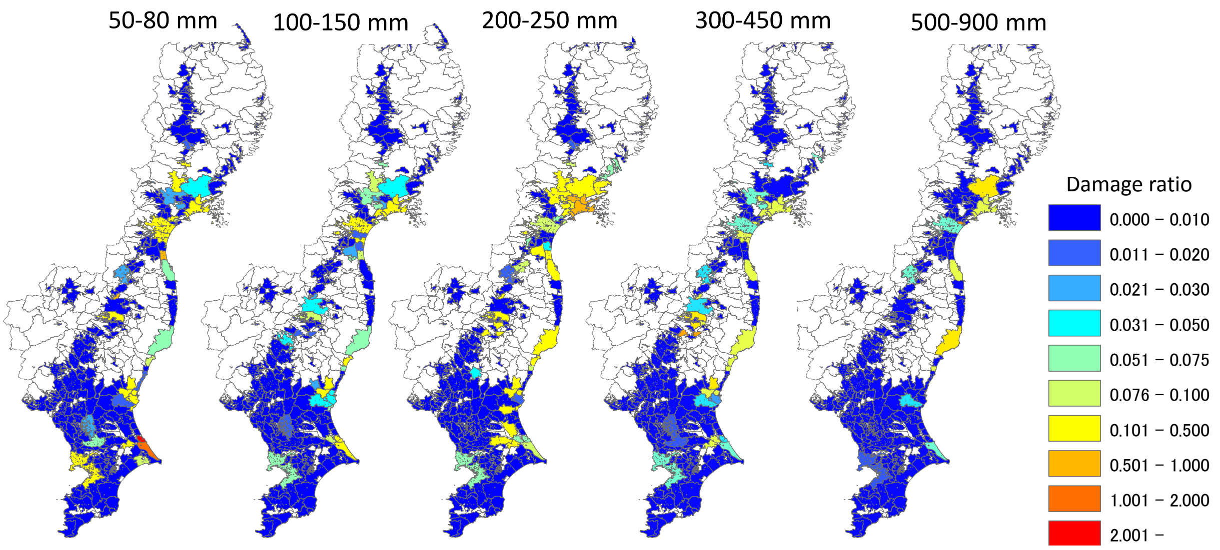

Fig. 3. Distribution of the damage ratios for DIP with the diameter range of 50-80, 100-150, 200-250, 300-450, and 500-900 mm.

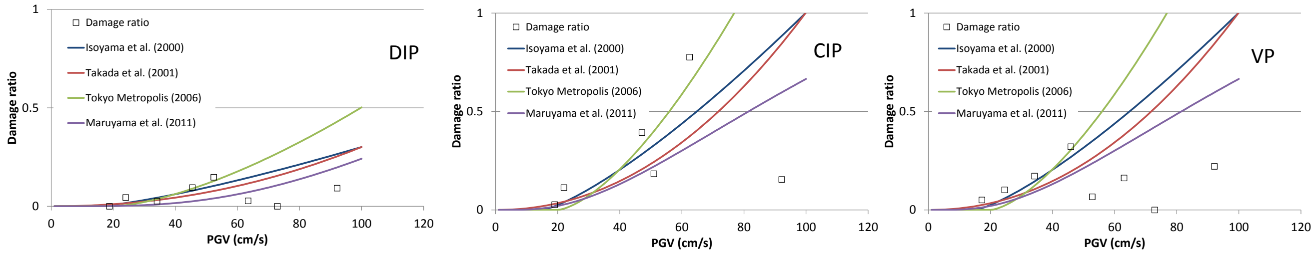

Fig. 4. Comparison of the damage ratios of water distribution pipes and the damage ratios estimated by previous studies [3-6].

geological conditions are not considered in this study (C_g = 1.0), because the distribution of PGV reflects those of geological conditions [10]. The correction coefficient for liquefaction is also not considered in this study (C_l = 1.0). According to the results, the damage ratios during the 2011 earthquake are in complete agreement with the empirical fragility functions.

IV. Damage Estimation Method on a Regional Scale in Case of Gigantic Earthquake

The Headquarters for Earthquake Research Promotion of Japan evaluated the national seismic hazard, and provided the Probabilistic Seismic Hazard Maps [11]. According to their assessment, the probability of occurrence of an earthquake in the Tokyo Metropolitan Area is approximately 70% within 30 years. It is also anticipated that an earthquake with a magnitude of 8-9 may occur in the Nankai Trough, which forms the plate interface between the subducting Philippine Sea Plate and the overriding Amurian Plate. In case these gigantic earthquakes occur, estimation of possible damage to various facilities on a regional scale will be required, in order to have a prompt disaster response at an early stage.

In the previous section, the applicability of the empirical fragility functions for water distribution pipes was discussed. They provide reasonable estimation for the water-supply areas where pipe breakages were found after the 2011 earthquake. On the other hand, as observed in Fig. 1, water-supply areas without pipe breakages were also found, even though the PGV is large enough to cause damage to water pipes. Hence, in order to perform damage estimation on a regional scale immediately after the occurrence of an earthquake, it is essential to identify the areas where pipe breakages may occur.

A logistic regression model is considered to evaluate the probability of occurrence of pipe breakages as shown in the equation below.

$$p = \frac{\exp(b_0 + b_1x_1 + b_2x_2 + b_3x_3 + b_4x_4)}{1 + \exp(b_0 + b_1x_1 + b_2x_2 + b_3x_3 + b_4x_4)} \tag{2}$$

where b_i is the regression coefficient, x_1 is the PGV, x_2 is the length of the water distribution pipes, x_3 is the vulnerability factor for pipe material [12], and x_4 is the vulnerability factor for ground condition, which is the mean of the correction factor C_g [3] in the water-supply area; p is the probability of occurrence of pipe breakages in the water-supply area. If pipe breakages were found in a specific water-supply area, 1.0 was substituted for the random variable Y. Y was assumed to be 0.0 for the areas without pipe breakages. Hence, p can be expressed as

$$p = \Pr(Y = 1.0 | x_1, x_2, x_3, x_4) \tag{3}$$

$$1 - p = \Pr(Y = 0.0 | x_1, x_2, x_3, x_4) \tag{4}$$

	Estimation	
Observation	Positive	Negative
True	True positive (TP)	False negative (FN)
False	False positive (FP)	True negative (TN)

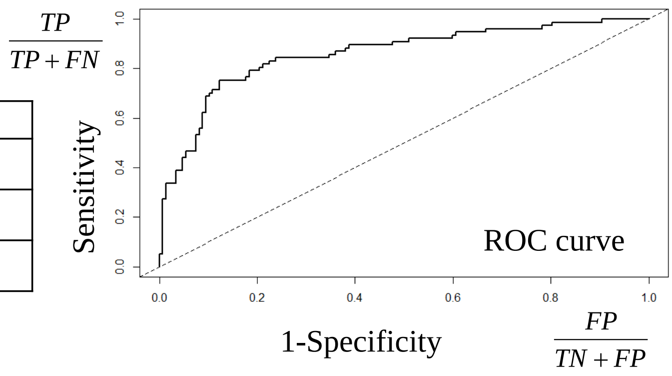

Fig. 5. Receiver operating characteristics (ROC) curve and definitions of the different fractions to draw ROC curve.

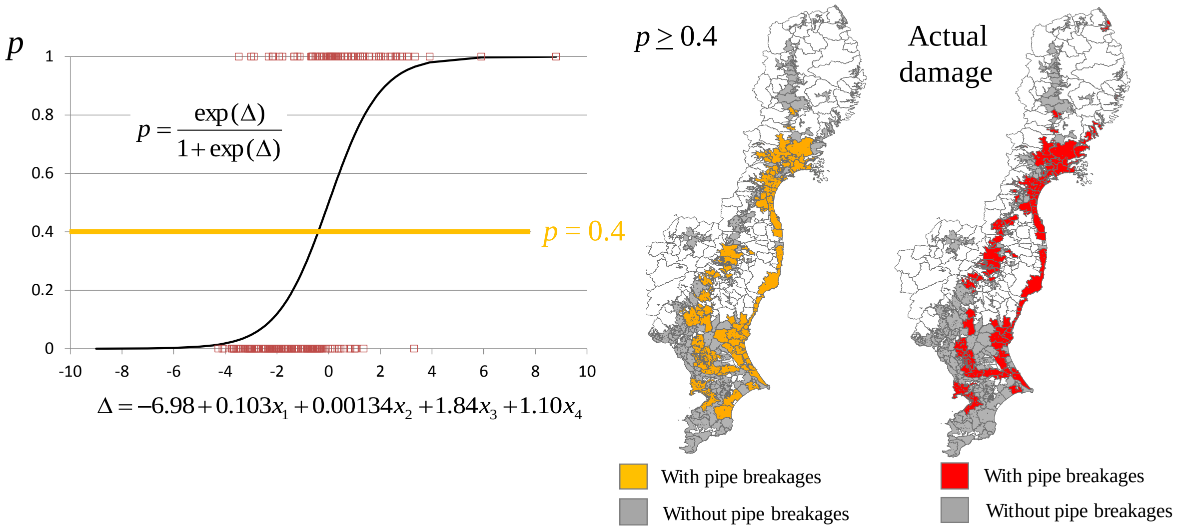

Fig. 6. Logistic regression model and the result of discrimination of the water-supply areas with/without pipe breakages.

A logistic regression analysis was performed using Eqs. (2)-(4). The threshold value of p to discriminate the water-supply area with/without pipe breakages properly is evaluated based on the receiver operating characteristics (ROC) curve (Fig. 5). In the ROC curve, the true positive rate (sensitivity) is plotted as a function of the false positive rate (1-specificity) by changing the threshold value of p [13]. The definitions of different fractions are also shown in Fig. 5. The area under the curve (AUC) was calculated as 0.86, which corresponds to a model with good discrimination. The best threshold of p was found to be 0.42, with true positive rate of 0.75, and true negative rate of 0.88.

Based on the results, the threshold value of p to discriminate the water-supply areas with/without pipe breakages was assumed to be 0.4. If p is larger than 0.4, the water-supply areas are considered to have the possibility of pipe breakages. Figure 6 shows the logistic regression model and the result of discrimination. In this figure, the water-supply areas with pipe breakages after the 2011 earthquake are also illustrated. The water-supply areas with pipe breakages could be identified reasonably well based on the logistic regression model constructed by this study.

This study tried to estimate the number of pipe breakages for water supply systems on a regional scale. First, the water-supply areas with pipe breakages are identified using the logistic regression model (Eq. (3)). Then, the empirical fragility functions are applied to estimate the damage ratios of water distribution pipes. Lastly, the number of pipe breakages is obtained as the product of damage ratios and the lengths of the water pipes.

Figure 7 compares the number of pipe breakages after the 2011 earthquake and those estimated using the empirical fragility functions [6]. The estimated values are slightly smaller than the actual number of pipe breakages for VP and CIP. The actual number of pipe breakages for DIP is three times larger than the estimated value. The locations of pipe breakages are very much concentrated in the water-supply areas in Chiba and Ibaraki Prefectures where extensive liquefaction was observed after the earthquake [14]. They were also concentrated in the developed hilly areas for residential purpose, such as Sendai City, Miyagi Prefecture [15]. The estimated values in this study are calculated using Eq. (1); however the correction coefficients for liquefaction (C_l) and geological condition (C_g) were assumed to be 1.0 in the calculation. This study underestimated the number of pipe breakages because the effects of larger strain due to liquefaction and landslide in the developed hilly areas were not considered. To obtain more accurate results, the correction coefficients for liquefaction and developed hilly areas should be properly considered in the estimation method.

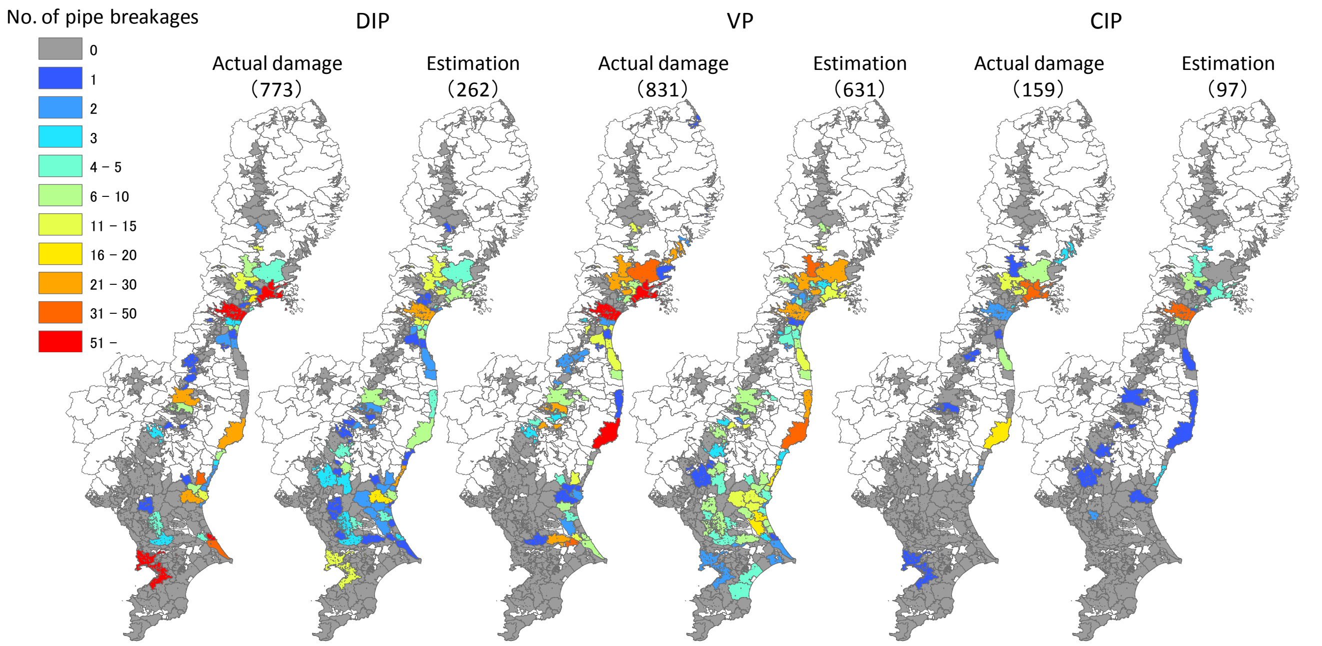

Fig. 7. Comparison of the number of pipe breakages for the pipes with diameter range of 100-150 mm after the 2011 earthquake and those estimated by this study.

V. Conclusion

This study evaluated the damage ratios of water distribution pipes after the 2011 off the Pacific coast of Tohoku earthquake based on the damage dataset compiled by MLHW. In order to obtain the damage ratios of water pipes, the length of pipes for different diameter ranges is estimated for different pipe materials, based on the detailed inventory data and the census data compiled by JWWA. The damage ratios were evaluated with respect to PGV, and the relationships were compared with the empirical fragility functions developed by the previous studies. The estimated values obtained from the fragility functions were reasonable and compared well with the actual damage ratios after this event.

To estimate the number of pipe breakages for water supply system after a gigantic earthquake, a damage estimation method on a regional scale is proposed. First, the water-supply areas with the possibility of pipe breakages are identified based on the logistic regression model. The model constructed by this study has a good discriminating ability based on the assessment of ROC curve. Further, the number of pipe breakages was estimated using the empirical fragility functions for the identified water-supply areas. The number of pipe breakages for VP and CIP show good agreement, but the number of breakages for DIP was underestimated. The correction coefficients for liquefaction and geological condition should be properly considered to obtain a more accurate estimation.

Acknowledgment

This work was supported by JSPS KAKENHI Grant Numbers 24686053 and 24310133.

References

[1] Japan Water Works Association. “Report of damage to water facilities after the 2011 off the Pacific coast of Tohoku earthquake,” http://www.jwwa.or.jp/houkoku syo/houkokusyo_18.html, 2011 (in Japanese).

[2] Ministry of Health, Labor and Welfare of Japan. “Report on the effects of the 2011 off the Pacific coast of Tohoku earthquake on water supply system,” http://www.mhlw.go.jp/topics/bukyoku/kenkou/suido/houkoku/suidou/130801-1.html, 2012 (in Japanese).

[3] R. Isoyama, E. Ishida, K. Yune, and T. Shirozu. “Seismic damage estimation procedure for water supply pipelines,” *Water Supply*, **18**(3), pp. 63-68, 2000.

[4] S. Takada, M. Miyajima, M. Yoda, M. Fujiwara, Y. Suzuki, and T. Toshima. “Study on the damage prediction method of buried pipelines under near field earthquake disaster,” *JWWA Journal*, **798**, pp. 21-37, 2001 (in Japanese).

[5] Tokyo Metropolitan Government. “Report on earthquake disaster scenario predictions,” 2006 (in Japanese).

[6] Y. Maruyama, K. Kimishima, and F. Yamazaki. “Damage assessment of buried pipes due to the 2007 Niigata Chuetsu-oki earthquake in Japan,” *Journal of Earthquake and Tsunami*, **5**(1), pp. 57-70, 2011.

[7] Ministry of Land, Infrastructure, Transport and Tourism of Japan. “National land numerical information download service,” http://nlftp.mlit.go.jp/ksj-e/index.html, 2012.

[8] National Institute of Advanced Industrial Science and Technology of Japan. “QuiQuake - Quick Estimation System for Earthquake Map Triggered by Observed

Records –," https://gbank.gsj.jp/QuiQuake/index.en .html, 2013.
[9] Japan Water Works Association. "Census data as of 2011," 2013 (in Japanese).
[10] K. Fujimoto and S. Midorikawa. "Empirical estimates of site amplification factor from strong-motion records at nearby station pairs," *Proceedings of the 1st European Conference on Earthquake Engineering and Seismology*, Paper No. 251, 2006.
[11] H. Fujiwara, S. Kawai, S. Aoi, T. Ishii, T. Okumura, Y. Hayakawa, N. Morikawa, S. Senna, K. Kobayashi, and K.X.S. Hao. "Japan seismic hazard information station, J-SHIS," *Proceedings of the 4th International Conference on Earthquake Engineering*, Paper No. 274, 2006.
[12] N. Nojima. "Seismic vulnerability index for lifeline facilities," *Proceedings of the 14th World Conference on Earthquake Engineering*, 8p, 2008.
[13] J.A. Hanley and B.C. McNeil. "The meaning and use of the area under a receiver operating characteristic (ROC) curve," *Radiology*, **143**(1), pp. 29-36, 1982.
[14] I. Towhata, S. Maruyama, K. Kasuda, J. Koseki, K. Wakamatsu, H. Kiku, T. Kiyota, S. Yasuda, Y. Taguchi, S. Aoyama, and H. Hayashida. "Liquefaction in the Kanto region during the 2011 off the Pacific Coast of Tohoku earthquake," *Soils and Foundations*, **54**(4), pp. 859-873, 2014.
[15] Y. Maruyama, K. Wakamatsu, and S. Nagata. "Comparison of the observed and estimated fragility of the water distribution system of Sendai City, Miyagi Prefecture during the 2011 Tohoku earthquake," *Proceedings of the 10th National Conference in Earthquake Engineering*, Earthquake Engineering Research Institute, doi: 10.4231/D3KD1QM0P, 2014.

Journal of Energy Challenges and Mechanics
http://www.nscj.co.uk/JECM/
ISSN 2056-9386
Volume 2 (2015) issue 4, article 6

Computer programs for analysis of solar domestic hot water systems: RETScreen case study

太阳能生活热水系统分析之计算机程序：RETScreen 案例研究

Leandra Altoé[1]; Delly Oliveira Filho[1,*]; Francisco Javier Rey Martinez[2]; Joyce Correna Carlo[3]; Paulo Marcos de Barros Monteiro[4]

[1]*Department of Agricultural Engineering, Universidade Federal de Viçosa, Viçosa, Minas Gerais, Brazil*
[2]*School of Industrial Engineering, Department of Energetic Engineering and Fluid Mechanics, Universidad de Valladolid, Valladolid, Spain*
[3]*Department of Architecture and Urbanism, Universidade Federal de Viçosa, Viçosa, Minas Gerais, Brazil*
[4]*Department of Control and Automation Engineering, Universidade Federal de Ouro Preto, Ouro Preto, Brazil*

**delly@ufv.br*

Accepted for publication on 23rd November 2015

Abstract - **The simulation programs are important tools for analyzing different energetic options, including the use of energy efficiency measures and renewable energies. The objective of this study was to analyze comparatively the different computer tools available for modeling of solar domestic hot water systems in buildings. Among the main simulation software in use for this purpose, there are RETScreen International, EnergyPlus, TRNSYS, SolDesigner, SolarPro, e T*SOL. Among the tools mentioned, only EnergyPlus and RETScreen International are free, but they allow obtaining interesting results. In the presented case study can be seen the versatility of the RETScreen program, which allows for analysis of energy production, economic viability and carbon dioxide emissions. Within the range of computer solar water heaters simulators currently available, it is necessary that the user knows the tool specifications, such as programming language and capabilities so one may choose the program that is most suitable to produce the expected results for one's knowledge and modeling skills.**

Keywords - **software, solar energy, water heating, buildings.**

I. INTRODUCTION

In recent years have seen a sharp increase in energy demand of buildings, due to population growth, increased time spent indoors and improvements in the conditions of comfort to users. The contribution of the buildings in relation to energy consumption has reaching values between 20% and 40% in developed countries [1]. In developing countries, energy consumption by buildings is also increasing due to improving people's quality of life. In Brazil, buildings account for 13.7% of final energy consumption and 48.5% of electricity consumption [2].

Over the past 50 years, a wide variety of energetic simulation programs of buildings have been developed, enhanced and are presently in use throughout the energy professionals [3]. From the 1970s, we observed a greater creation of energetic simulation programs increased, result of increased computer availability, the first oil crisis and the growing environmental awareness [4]. The United States Department of Energy lists on its website more than 400 computational tools for evaluating energy efficiency, renewable energy, and sustainability in buildings. A brief description of each program is provided, as well as target audience, programming language and strengths and weaknesses of the tools [5].

Through simulation can evaluate the thermal and energy performance of buildings for different options, such as architectural design, construction components, lighting systems and air conditioning systems. With the computer simulation, we can estimate the amount of energy, the cost of energy use and the environmental impact of different options, even before the construction of the building [6].

An interesting option to reduce the energy demand of buildings, especially residential, is the use of solar water heaters. Studies in different countries have proven the technical-economic feasibility of this technology compared to conventional sources, such as electricity and natural gas [7-9].

In addition, several studies have shown the potential to reduce carbon dioxide emissions on cooking of the buildings by solar thermal systems, particularly in countries with high dependence on fossil fuel [10-12].

In this context, the objective of this article was to conduct a comparative assessment of different computational tools available, focusing on their abilities and their target audience. In addition, an economic and environmental analysis of solar water heater based on RETScreen International is presented.

II. Comparative analysis of computer tools

The US government, based on popular features of two programs previously created, BLAST and DOE-2, developed the EnergyPlus. The software have innovative capabilities, including thermal and energy simulation in different zones, time steps smaller than an hour, and input and output data structures adapted to facilitate the development of the interface by third parties. Newer versions allow to calculate the energy and water consumption and the simulation of renewable energy systems, including thermal solar energy. The program is available for platforms Windows, Mac OS e Linux and uses Fortran 2003 as programming language. According to the program developers, high level of computer literacy not required, however engineering background helpful for analysis portions [5, 13].

RETScreen was developed by the Government of Canada and is currently available in 25 languages. It is estimated that there are more than 130,000 users of the program in 222 different countries. The software allows evaluating energy production, financial costs, economic viability and greenhouse gases emissions of systems based on renewable energy sources, including thermal and photovoltaic solar, wind, biomass and geothermal and energy efficiency measures, such as cogeneration. The software also includes databases of products, hydrology, climate and case studies for different types of projects. The program operates in Windows, Linux, and opera with Excel, Visual Basic and C++. As the software uses programming languages more known to the public, the user can easily learn how to use the program through the training material [5, 14].

The SolDesigner is a German program specialized in analysis of hydraulic design and control of solar thermal systems. It is useful for finding solutions for hot water projects and water solar heating in buildings and pools. SolDesigner produces a highly qualified design of the solar system and estimates for costs and energy production. The program is available for Windows platform and as well as RETScreen, uses Excel. According to the program developers, is not necessary programming knowledge to handle the SolDesigner [5].

The SolarPro was developed in United States and allows simulate the operation of solar hot water heating systems, hour by hour, for one year, such as EnergyPlus. Dozens of customizable variables can be incorporated into the simulation. The program operates in Windows computer platform and uses programming language of the type Visual Basic. To manage the program is recommended that the user have general knowledge of solar thermal processes [5].

TRNSYS, the Transient Systems Simulation Program, that has been commercially available since 1975, continues to develop by the international collaboration of the United States, France, and Germany. The program is primarily an equation solver program based on numerical techniques that allows the user to change the simulation complexity through of the inclusion of mathematics modules. As the EnergyPlus, it simulates buildings and their energetic systems in multi-zone, including solar thermal systems. TRNSYS operates Windows platform and uses as main programming language FORTRAN, although some components can also be written in C++. To operate this computer program, it is recommended that the user has some knowledge of FORTRAN, especially if he/she wants to modify the default calculation module [5, 15].

T*SOL is a German simulation program for the planning and professional design of solar thermal systems. The standard module contains a large number of configurations of hot water system, space heating systems and swimming pools. As the main capacity is the project design, the presents an extensive database with solar heating products, which facilitates its implementation. The program works in Windows operating system and uses Delphi programming language. Just as most of the programs mentioned above, it is not necessary programming knowledge to operate the T*Sol, just some prior information about operation of solar water heaters [5].

The EnergyPlus, RETScreen International, SolDesigner, SolarPro, TRNSYS and T*Sol tools have distinct capabilities and consequently are intended for different users. Some are simple, with the main function of design, while others make a more detailed analysis of the system. In Table 1 is shown a comparison among different computer programs for analysis of domestic solar water heaters, indicated by the Department of Energy of the United States. It is noted that only the RESTcreen and EnergyPlus are free, however it is possible to meet a wide audience with these programs, including students, civil construction professionals, energetic planners and researchers.

SolarPro, SolDesigner and T*Sol has been used more by construction professionals, while TRNSYS, EnergyPlus, and RETScreen International are more widely used in scientific research, especially due to its detailed analysis modules and be validated by several tests. Some scientific studies conducted with the aid of such software tools are presented below.

TABLE 1. CHARACTERISTICS OF COMPUTATIONAL PROGRAMS FOR ANALYSIS OF SOLAR DOMESTIC HOT WATER SYSTEMS

Program	Application	Audience	Strengths	Weaknesses	Access
EnergyPlus	Building performance, energy simulation, heat and mass balance, load calculation	Engineers, architecture consulting firms, utilities, federal agencies, researchers	Detailed and accurate simulation Allows to import geometry from CAD programs	Text input may make it more difficult to use than graphical interfaces	Free
RETScreen International	Energy, economic and environmental analysis of projects based on renewable energy and efficiency energetic	Engineers, architects, technologists, planners, facility managers, educators, researchers	Friendly platform and tool for easy application	n/a	Free
SolDesigner	Design of solar water heaters and circuits of hot water	Officials, tech-design engineers, house-owners, builders, plumbers	Detailed design of the thermal solar system	Does not give simulated energy yields	Not Free
SolarPro	Solar water heating, thermal processes, renewable energy, simulation	Solar design engineers, solar contractors, do-it-yourselfers	Accurate and detailed simulation	Level of user input can be cumbersome	Not Free
TRNSYS	Energy simulation, building performance, load calculation, renewable energy, energy efficiency	Engineers, architects, researchers, consulting firms	Allows modeling at different levels of complexity. Interacts with various other simulation packages	Require detailed information about the building and energy system	Not Free
T*SOL	Solar thermal heating, swimming pool heating, solar planning and design	Solar specialists, planners, engineers, heating technicians, plumbers, energy consultants	Precise calculations possible very user friendly	n/a	Not Free

Source: [5].

Canadian researchers studied the optimal design of a forced circulation solar water heating system for a residential unit in cold climate using TRNSYS, in Montreal. For these weather conditions, it was obtained the optimal system could provide 83-97% and 30-62% of the hot water demands in summer and winter, respectively. It is also determined that this system can provide about 54% of the heating energy needs of water per annual solar energy [16].

In another study, TRNSYS program was used to evaluate the performance evaluation of a net-zero-energy house in Datong, China. The hot water system with electric backup was designed considering the family of three people, with the total daily demand of 150 liters for water heating and 250 liters for radiant floor heating. For the conditions of Datong, was verified by simulation that to meet this hot water demand would be necessary a system with 7.6 m² of solar collector and hot water tank with 400 liters capacity [17].

Italian researchers applied EnergyPlus program to analyze of net-zero-energy households in your country. In total 40 economically and technically feasible energy efficiency measures for a high performing single-family house were evaluated. Through simulation, it was found that to attend the demand of domestic hot water would be needed a solar heater with gas backup with 5.9 m² solar collector, coupled to a thermal reservoir 800 liters, which is also used for other heating purposes in the housing, for an annual solar fraction of 80% [18].

Greek investigators used the RETScreen InternationalI to analyze the technical and economic viability of solar water heaters in Thessaloniki. It was found that a solar system with electric assistance, designed to meet an annual solar fraction of about 60%, in such meteorological conditions, can provide 1,702 kWh year^{-1}, with payback of five years, internal rate of return of 21.8% per year internal rate of return and net present value of 2,103 euros [19].

The RETScreen International program was also applied to evaluate the potential to reduce of carbon dioxide by means of solar water heaters in households in the Serbia. For an electricity grid mix of 73% thermal and 27% hydro power plants, the installation of a system to meet a typical house represents the reduction 31 to 34 tCO_2 during the system lifetime, depending on the region of the country considered [12].

According to a Canadian Government survey, in the period of 1998 to 2004, this tool was used in the design of projects had a total installed capacity of 1,000 MW of generation by several renewable sources, avoiding the emission of 630 kt CO_2/year [20]. The following a case study is presented to demonstrate the applicability of RETScreen International for design and life cycle analysis of a domestic hot water system, in a typical Brazilian dwelling.

III. RETSCREEN CASE ESTUDY

The RETScreen International program was used to analyze a solar water heater, designed to meet a typical Brazilian dwelling. It conducted a study of economic feasibility and reduction of greenhouse gases emissions of the solar system, compared to using electric energy. The electrical water heating system without storage, also known as electrical resistance showerheads, is the water heating system most widely used in Brazil. This appliance is present in 73.5% of Brazilian dwellings, accounting for around 24% of electricity consumption in these conditions [21].

It was considered a typology of dwelling intended for a family of four people, with two bedrooms, a living room, a kitchen and a bathroom, with a total area of 63 m². This model has features representing 58% of Brazilian dwellings [22].

This study considered a solar system consisting of flat solar collectors and horizontal thermal reservoir, with natural circulation of water (thermosyphon effect). The parameters adopted for the design of the solar domestic hot water system are as follows:

- Dwelling with four residents;
- A daily bath per resident;
- Water consumption per bath of 50 liters;
- Bath time of 10 minutes;
- Bath temperature equal 40 °C;
- Flat solar collector with copper pipes and glass cover, optical efficiency factor of 0.779 and global coefficient of loss of 6.795 W/(m².K); and
- Horizontal thermal reservoir with stainless steel coating and polyurethane insulation.

The solar system was simulated for the weather conditions of the city of Belo Horizonte, Minas Gerais, Brazil (latitude -19°55'15"; longitude -43°56'16"). Belo Horizonte receives annual average daily solar radiation, in the horizontal plane, of 4.34 kWh/m²/day and has an average annual temperature of 22.3°C.

Through the implementation of the RETScreen International program was proposed to size two solar water heaters, one with annual solar fraction of 70% and other with 80%. It is emphasized that 70% is the minimum value of annual solar fraction recommended by the Brazilian standard used as a reference for sizing of solar water heaters, the NBR 15569: Solar Water Heating System in Direct Electric Circuit [23]. The results are shown in Table 2.

TABLE 2. SIZING OPTIONS FOR THE SOLAR DOMESTIC HOT WATER SYSTEM, ON METEOROLOGICAL CONDITIONS OF BELO HORIZONTE, BRAZIL.

Annual solar fraction (%)	Solar collector area (m²)	Thermal reservoir capacity (L)
70	2.0	200.0
80	3.0	200.0

It was presented two sizing options as an example in this work, but it can simulate various other by the program, including changing the type of solar collector and thermal reservoir. The software has a database with hundreds of solar heating products, with their technical characteristics, to assist the program user.

After defining various design options, it can be check, which shows the better economic feasibility by using the RETScreen International software. The parameters considered in this study to analyze the economic feasibility of the solar domestic hot water system, compared to electric shower, are as follows:

- Cost of the solar system with an annual solar fraction of 70%, including the costs of acquisition and installing: US$ 980;
- Cost of the solar system with an annual solar fraction of 80%, including the costs of acquisition and installing: US$ 1,090;
- Electricity tariff for the residential sector in Belo Horizonte including taxes: US$ 0.215/kWh;
- Horizon of the solar system planning: 20 years;
- Discount rate: 8% per year; and
- Annual adjustment of electricity tariff: 2% per year.

The results of the economic feasibility analysis of the solar system, found through the program's application, are presented in Table 3.

TABLE 3. INDICATORS OF ECONOMIC FEASIBILITY OF A SOLAR WATER HEATER ON THE METEOROLOGICAL CONDITIONS OF BELO HORIZONTE, BRAZIL, COMPARED TO ELECTRIC SHOWER USE.

Indicator	Solar fraction 70%	Solar fraction 80%
Internal rate of return	26.8% per year	27.7% per year
Net present value	US$ 1,809	US$ 2,129
Simple payback	4.1 year	3.9 year
Benefit-cost ratio	2.85	2.95

Therefore, it was verified that, between the two proposed design options, the system with annual solar fraction of 80% presented a higher profitability to the owner of the dwelling. However, it is noteworthy that the two design options showed good indicators of economic feasibility, with payback time within the first quarter of the estimated useful life for the solar heater and a rate of return greater than 25% per year. The rates of return obtained were more than triple the discount rate considered for the project, of 8% per year. In this study was regarded that the owner of the dwelling has the initial capital to invest in the solar water heater, however the program also allows evaluate the economic viability considering financing and subsidies.

Besides being interesting to the owner of the dwelling, the use of solar water heaters is also economically attractive to the National Electric System. As the electric showerheads have high power, around 3 to 8 kW, and is turn on mostly at the beginning of the night, contribute to increase the peak demand of the national load curve, creating costs for demand supply. The installation of each solar domestic hot water system generates a saving US$336 to US$405 for National Electric System, considered the costs of expanding capacity [24].

In case one want to calculate through the RETScreen International software the reduction of greenhouse gas emissions from the clean energy project. For this case study, it was found that the replacement of the electric showerhead by the solar water solar heater with annual solar fraction of 70% e 80% was, respectively, 97 and 112 kgCO_2equivalent/year. For comparison, the Figure 1 is shown the avoided emissions of the system with annual solar fraction of 80% in relation to different sources of energy.

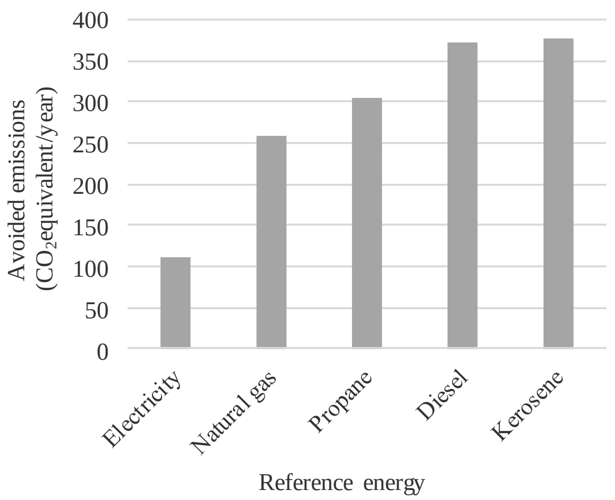

Fig.1, Reduction of greenhouse gas emissions of a solar domestic hot water system with an annual solar fraction of 80%, in Belo Horizonte, Brazil, compared to using of other energy sources.

The mitigation of emissions by the use of solar water heaters in relation to electricity was much lower compared to non-renewable energy sources in the studied case. This occurs because the Brazilian electric energy matrix have large share of renewable sources, around 79.3% [2]. The emission factor of greenhouse gases by the electricity system in Brazil is 0.087 tCO_2equivalente/MWh, while in the United States, China and Australia is respectively 0.522, 0.766 and 0.841 tCO_2equivalente/MWh [24]. It is noteworthy that solar thermal energy has other environmental benefits beyond reducing emissions of greenhouse gases. Large hydroelectric plants, source most used in Brazil for the production of electricity, generate negative impacts on the local and regional environment due to the need to flood large areas.

The program also allows to convert the emissions avoided in several equivalent mitigation measures. Table 4 is presented some measures equivalent to the installation of solar water heaters in 1,000 households with an annual solar fraction of 80% in Belo Horizonte, Brazil.

TABLE 4. EQUIVALENT EMISSIONS MITIGATION OF GREENHOUSE GASES TO THE INSTALLATION OF SOLAR DOMESTIC HOT WATER SYSTEM IN 1,000 DWELLINGS, IN BELO HORIZONTE, BRAZIL.

Mitigation measure	Quantity
Gasoline not used	48,123 liters per year
Oil not consumed	260 barrels per year
Urban solid waste recycling	37 tons per year
Forest absorbs carbon dioxide	10 hectares per year

This feature of the RETScreen International program is interesting to facilitate the user's understanding about the negative environmental impact avoided by the use a renewable energy source, in this case, the solar domestic hot water system.

IV. CONCLUSION

Computational tools for the modeling of solar water heaters have been used, throughout the world, to assist professionals in tasks such as sizing and energy analyses. Nowadays, there is a wide variety of programs for different users. Amongst the most widespread tools, there are RETScreen International, EnergyPlus, TRNSYS, SolDesigner, T*SOL and SolarPro.

Among the tools mentioned, only the EnergyPlus and RETScreen International are free, but allow obtaining interesting results, and they are designed for a diverse audience, including designers, researchers and energy planners. The first program has a module of detailed energy analysis of solar water heaters, while the second one has modules of economic feasibility of the system and greenhouse gas emissions analysis. In the presented case study can be seen the versatility of the RETScreen program, which allows for analysis of energy production, economic viability and carbon dioxide emissions.

Therefore, within the range of computer solar water heaters simulators currently available, it is necessary that the user know the tools specifications, such as programming language and capabilities so one may choose the program that is most suitable to produce the expected results for one's knowledge and modeling skills.

ACKNOWLEDGMENTS

The authors thank Procel Edifica/Eletrobras, the National Council for Scientific and Technological Development (CNPq) and the Minas Gerais State Research Foundation (Fapemig) for their financial support.

REFERENCES

[1] L.P. Pérez-Lombard, J. Ortiz and C. Pout. “A review on buildings energy consumption information”, *Energy and Buildings*, **40**, pp. 394-398, 2008.

[2] Energy Research Company. National Energy Balance 2014: Base year 2013. Rio de Janeiro, 2014.

[3] D.B. Crawley, L.K. Lawrie, F.C. Wilkelmann, W.F. Buhl, Y.J. Huang, C.O. Pedersen, R.K. Strand, R.J. Liesen, D.E. Fisher, M.J. Witte and J. Glazer. “EnergyPlus: creating a new-generation building energy simulation”, *Energy and Buildings*, **22**, pp. 319-331, 2001.

[4] F. Urban, R.M.J. Benders and H.C. Moll. “Modelling energy systems for developing countries”. *Energy Policy*, **35**, pp. 3473-3482, 2007.

[5] U.S. Department of Energy. Available in: http://apps1.eere.energy.gov/buildings/tools_directory. Accessed in April, 22, 2015.

[6] N. Mendes, F.S. Westphal, R. Lamberts and J.A.B. Cunha Neto. “Uso de instrumentos computacionais para análise do desempenho térmico e energético de edificações no Brasil”. *Ambiente Construído*, **5**, pp. 47-68, 2005.

[7] S. Kalogirou. “Thermal performance, economic and environmental life cycle analysis of thermosiphon solar water heaters”. *Solar Energy*, **83**, pp. 39-48, 2009.

[8] H. Cassard, P. Denholm and S. Ong. “Technical and economic performance of residential solar water heating in the United States”. *Renewable and Sustainable Energy Reviews*, **15**, pp. 3789-3800, 2011.

[9] H.F. Naspolini and R. Rüther. “Assessing the technical and economic viability of low-cost domestic solar hot water systems (DSHWS) in low-income residential dwellings in Brazil”. *Renewable Energy*, **48**, pp. 92-99, 2012.

[10] G. Tsilingiridis and G. Martinopoulos. “Thirty years of domestic solar hot water systems use in Greece - energy and environmental benefits - future perspectives”. *Renewable Energy*, **35**, pp. 490-497, 2010.

[11] Y. Hang, M. Qu and F. Zhao. “Economic and environmental life cycle analysis of solar hot water systems in the United States”, *Energy and Buildings*, **45**, pp. 181-188, 2012.

[12] S. Stevanovic and M. Pucar. “Financial measures Serbia should offer for solar water heating systems”. *Energy and Buildings*, **54**, pp. 519-526, 2012.

[13] Ernest Orlando Lawrence Berkeley National Laboratory. Getting Started with EnergyPlus. Berkeley, 2013.

[14] Natural Resources Canada. RETScreen International. Available in: http://www.retscreen.net/. Accessed in April 20, 2015.

[15] Solar Energy Lab - Solar Energy Laboratory of University of Wisconsin-Madison. TRNSYS 16: Volume 1 Getting Started. Madison, 2013.

[16] A. Hobbi and K. Siddiqui. “Optimal design of a forced circulation solar water heating system for a residential unit in cold climate using TRNSYS”. *Solar Energy*, **83**, pp. 700-714, 2009.

[17] C. Peng, L. Huang, J. Liu and Y. Huang. “Energy performance evaluation of a marketable net-zero-energy house: Solark I at Solar Decathlon China 2013”. *Renewable Energy*, **81**, pp. 136-149, 2015.

[18] C. Becchio, P. Dabbene, E. Fabrizio, V. Monetti and M. Filippi. “Cost optimality assessment of a single family house: Building and technical systems solutions for the nZEB target”. *Energy and Buildings*, **90**, pp. 173-187, 2015.

[19] C.J. Koroneos, A. Evanthia and E.A. Nanaki. “Life cycle environmental impact assessment of a solar water heater”. *Journal of Cleaner Production*, **37**, pp. 154-161, 2012.

[20] CANMET Energy Technology Centre. RETScreen International: Results and Impacts 1996-2012. Varennes, 2004.

[21] Brazil Energy Central. Search for possession of equipment and usage habits: Base year 2005: Residential Class. Rio de Janeiro, 2007.

[22] S.F. Tavares. Methodology for analysis of the life energy of Brazilian residential buildings. Ph.D. Thesis, Universidade de Santa Catarina, Florianopolis, 2006.

[23] Brazilian Association of Technical Standards. NBR 15569: Solar Heating System Water in Direct Electric Circuit - Design and Installation. Rio de Janeiro, 2008.

[24] L. Passos, J.M. Cardemil and C. Colle. “Feasibility Study of Using Domestic Solar Hot Water Systems as Alternative to Reduce the Electricity Peak Demand in Brazil”. *Energy Procedia*, **57**, 2014, pp. 2487-2495, 2014.

Journal of Energy Challenges and Mechanics
http://www.nscj.co.uk/JECM/
ISSN 2056-9386
Volume 2 (2015) issue 4

TABLE OF CONTENTS pages

Journal of Energy Challenges and Mechanics

ISSN 2056-9386

http://www.nscj.co.uk/JECM/

Scope:

Since James Watt, a Scottish inventor, improved efficiency of the steam engine, human civilization relies more and more on a steady supply of energy. Today we are at a transitional age. On the one hand, we see technology advances in the exploration and development of oil and gas, a depleting resource; we see growth in handling aging and decommissioning. On the other hand, we see ideas and plans for new energy infrastructure. This journal is about energy challenges and the underlying mechanics, involving multiple disciplines in science, technology, management and policy-making. Mechanics, fundamentally, is about force and the related behaviours, where force is about relationships, including those physical, human and social. For mechanics, the journal covers interactive boundaries with many other disciplines. For energy, topics include both fossil fuels and many different forms of renewable energy; also, issues related to energy economy, energy policy, efficiency, safety, environment and ecology will also be covered.

North Sea

Cove Bay, Aberdeen, Scotland, United Kingdom